Targeted Electrochemical Reactions at the Active Sites of the Photosystem I Protein Complex

By

Joshua M. Passantino

Dissertation

Submitted to the Faculty of the

Graduate School of Vanderbilt University

In partial fulfillment of the requirements

For the degree of

DOCTOR OF PHILOSOPHY

In

Chemical Engineering

May 13, 2022

Nashville, TN

Approved:

G. Kane Jennings, Ph.D.

David E. Cliffel, Ph.D.

Matthew Lang, Ph.D.

Nathan Schley, Ph.D.

Jamey Young, Ph.D.

DEDICATION

For my family

ACKNOWLEDGEMENTS

First, I would like to thank the many organizations that provided funding for the work presented in this dissertation. I received funds from the National Science Foundation (NSF) through the Graduate Research Fellowship Program and summer students that worked with me also received NSF funding. The United States Department of Agriculture (USDA) also provided funds for much of the PSI work. Vanderbilt provided funding during my time as a Teaching Aide for multiple classes.

I want to thank my advisor, Dr. Kane Jennings, for all of the help and guidance he has given me during my time at Vanderbilt. He has served as a role model for how to be a good mentor and how to be a better researcher. He also provided me more knowledge about Auburn sports news than ESPN, which was a welcome reprieve from focusing on academic and research work. I also want to thank Dr. David Cliffel, who served as a secondary mentor who gave his guidance and expertise to help me be a competent electrochemist. I want to thank Dr. Paul Laibinis for his grilling me with research questions during our group meetings and helping me be a better teacher in the classroom. Additionally, I want to give thanks to Dr. Matthew Lang, Dr. Nathan Schley, and Dr. Jamey Young for serving on my dissertation committee and giving me advice throughout the PhD process.

I would also like to thank the Jennings and Cliffel research groups with whom I worked on PSI projects with. These members include Dr. Dilek Dervishogullari, Dr. Chris Stachurski, Dr. John Williams, Dr. Kody Wolfe, Matt Galazzo, Marc Nabhan, and the undergraduate students Tyler Oddo and Long Than. I also want to thank Dr. Maxwell Robinson for his mentorship in research during my first year. I want to especially thank Dr. Kody Wolfe for his collaboration and

friendship in and out of the lab. We had many conversations about work and our lives out of the lab that greatly improved my experience at Vanderbilt.

I want to thank Keiann Simon, Inaya Molina, and Alessia Williams, each of whom served as one of my mentees through the Vanderbilt Institute for Nanoscale Science and Engineering (VINSE) summer REU program. They all were fantastic mentees who helped me to develop as a mentor each summer. I also want to thank Lucas Mowery and Blake Christiansen who were two undergraduate researchers from Vanderbilt who worked directly with me on projects. Additionally, I would like to thank Riley Knight, who asked me to serve as a mentor and help her through her undergraduate research career.

Both Dr. Bradley Baker and Dr. Liudmyla Prozorovska ensured that the lab office was always filled with conversations about all topics under the sun, and I am very grateful to have worked alongside them. The office was much quieter after they left. I also want to thank the rest of the Jennings and Laibinis groups who were not involved in the PSI project: Allison Cordova, Dr. Ricky Deng, Joshua Livingston, Zane Parkerson, Ali Shawon, Ryan Solomon, and Juliana Yang.

I want to thank the members of VINSE who worked with me through research and through the summer REU program. In particular, I want to acknowledge Dr. Dmitry Koktysh, Alisha McCord, and Sarah Ross for their hard work in running VINSE. I also want to thank VINSE for allowing me to be part of their research program, through which I met Janna Eaves-Rathert, who is now a good friend to me.

I worked mainly with two student groups, the Graduate Student Council and Engineers Without Borders. I want to thank all of the members I worked with on those groups, and I am thankful for all of the good work we were able to do for graduate students and communities in

need. Big shoutout to Chloe Frame, who served as the Student Life Liaison this past year during my presidency who worked with me on so many projects to help our peers.

I would like to thank the Chemical and Biomolecular Engineering Department at Vanderbilt and everyone who kept it running. In particular, Felisha Bacquera and Jenni Powell are two of the hardest workers I know, and I am grateful for their dedication to helping the department. I also want to thank the graduate students of the department who were my family for my 5 years at Vanderbilt.

I would not have made it through my graduate career if not for my closest friends who were by my side my entire time here. Michael Kosson was my first roommate in Nashville, and we were nearly inseparable after that. Michael and I met Maddie Johnson and Hannah Stephens during their recruitment visit at Vanderbilt. They became my core community at Vanderbilt, and I am so grateful to have met and worked with each one of them. We bonded over watching the US Men's curling team win a gold medal in 2018. So it was fitting that the last time we were all together as students was when we all tried our hand at curling for the first time.

Finally, I want to thank all of the members of my family, who have been supportive and amazing through my entire graduate career. To my parents, Vicki and Michael, thank you for being some of the best parents I could ask for. To my sister, Meaghan, thank you for always doing art projects for me because I can't even draw a straight line with a ruler. My grandmother, Lottie, you have been one of my biggest cheerleaders in my life, and I am so fortunate to be your grandson. I also must thank my cat, Yoshi, who has been by my side for 8 years at this point and had to deal with me more than any other living being. Somehow, he still loves me, I think. I love all of you and hope that I continue to make you proud.

TABLE OF CONTENTS

Chapter 3

Chapter 4

Chapter 5

Chapter 6

Appendices

List of Abbreviations:

Ascorbic Acid (AscH), Attenuated Total Reflectance-Fourier Transform Infrared Spectroscopy (ATR-FTIR), Atom Transfer Radical Polymerization (ATRP), Cyclic Voltammetry (CV), 2,6-dichlorophenolindophenol (DCPIP), Direct Electron Transfer (DET), Dehydroxyascorbic Acid (DHA), Dye-Sensitized Solar Cell (DSSC), Electrochemical Impedance Spectroscopy (EIS), Energy Dispersive X-Ray Spectroscopy (EDS), Fill Factor (FF), Fluorine-Doped Tin Oxide (FTO), Short-Circuit Current (J_{SC}), Mediated Electron Transfer (MET), Methyl Viologen (MV), Molecular Weight Cut Off (MWCO), Oxidized Species (O), Open-Circuit Potential (OCP), Polyaniline (Pani), Photochronoamperometry (PCA), Photochronopotentiometry (PCP), Partial Differential Equations (PDEs), poly-3,4-ethylenedioxythiophene (PEDOT)Polypyrrole (PPy), Photosystem I (PSI), Photosystem II (PSII), Polystyrene sulfonate (PSS), Pyrrole (Py), Reduced Species (R), Reversible Addition Fragmentation Chain-Transfer (RAFT), Relative Centrifugal Force (RCF), Sodium Dodecyl Sulphate-Polyacrylamide Gel Electrophoresis (SDS-PAGE), Scanning Electron Microscopy (SEM), Thermogravimetric Analysis (TGA)

LIST OF TABLES

LIST OF FIGURES

Appendix

Chapter 1

Photosystem I

Introduction

Solar energy conversion is a promising approach to resolving global dependence on fossil fuels for electricity production and materials manufacturing. Annually, over 800 million TWh of energy from the sun strike the Earth, providing an extraordinary capacity to harvest that energy for utilization in our day-to-day lives.[1] Photosynthesis has developed and adapted over billions of years to harvest and use 800 thousand TWh annually, which is nearly five times the 167 thousand TWh humans used in total energy demand in 2018.[2,3] With the current state of solar energy conversion, under 500 TWh of energy is produced through human-made solar devices, which tend to have unfavorable cost-to-efficiency ratios because of the use of nonrenewable materials and unsustainable processing.[3] To resolve these issues, biological photosynthetic materials are being explored to improve solar energy conversion.

Photosystem I (PSI) is an integral protein involved in photosynthesis and approaches 100% quantum efficiency from the light harvested; this efficiency, coupled with the abundance and low cost of photosynthetic materials, has pushed investigators to explore biological materials for solar energy conversion. The PSI protein complex has grown in reputation over the last two decades as a powerful redox-active biological material and is a prime candidate for biohybrid solar energy conversion. This 500 kDa trans-membrane protein complex found in the thylakoid is essential in the light reactions of photosynthesis. *In vivo*, the primary function of PSI is to accept low energy electrons from plastocyanin, excite the electrons to a higher energy state with photons collected by surrounding chlorophylls, and donate the excited electrons to ferredoxin to produce NADH.[4]

The oxidation and reduction capabilities of PSI, as well as its rapid charge separation, have drawn attention from researchers who see PSI as a potential component in photochemical applications. On the stromal side of the protein, the iron-sulfur cluster known as the F_B site attains one of the most negative reduction potentials (-590 mV vs. SHE) found in nature.[5] In the lumenal pocket, the P_{700} chlorophyll pair has been shown to have a potential near 450 mV vs SHE, enabling P_{700} to oxidize a wide range of electron donors and creates a potential difference of over 1 V across the protein with >99% energy conversion efficiency of the light absorbed by the protein.[5] The chlorophyll and reaction sites of PSI are shown in Figure 1.1.

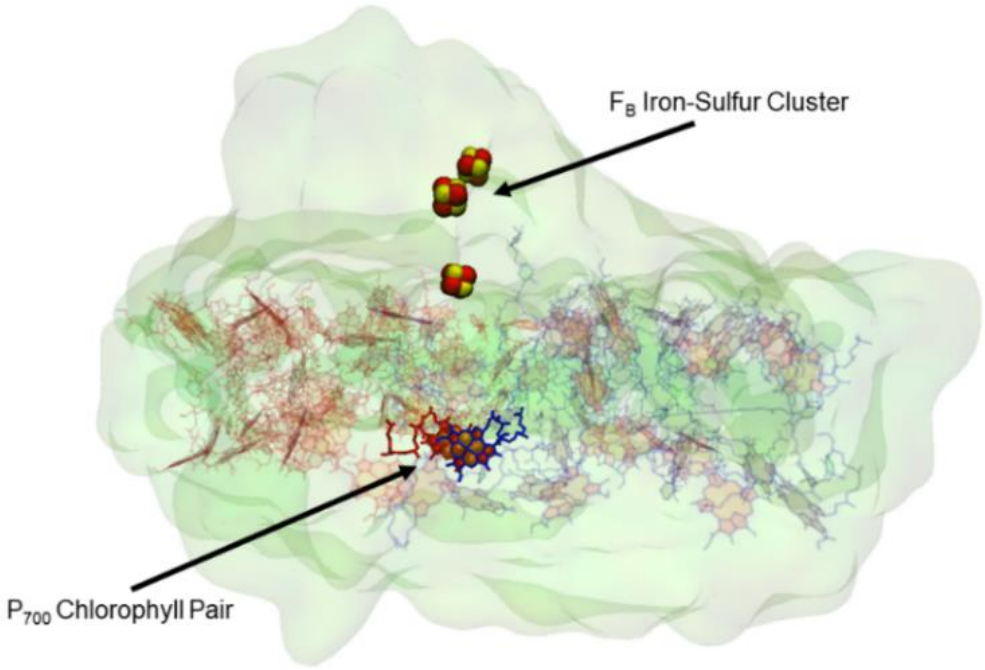

Figure 1.1: Structure of reaction sites found in PSI. The PsaA (red) and PsaB (blue) subunits are shown. Atomic coordinates used in this figure are from PDB entry 6JO6, contributed by Suga et al.[6]

The charge separation time from P_{700} to the F_B site is on the order of 700 ns while recombination from the F_B site occurs in the tens of ms, allowing rapid transfer of electrons with relatively slow charge recombination.[7] The electron transport chain of PSI is has two separate pathways (A-Branch or B-Branch) and is shown in Figure 1.2. The redox sites have two states

(P_{700} or P_{700}^{+}) and (F_B or F_B^{-}). For simplicity, in the rest of this dissertation, they will be referred to as P_{700} or F_B regardless of oxidation state.

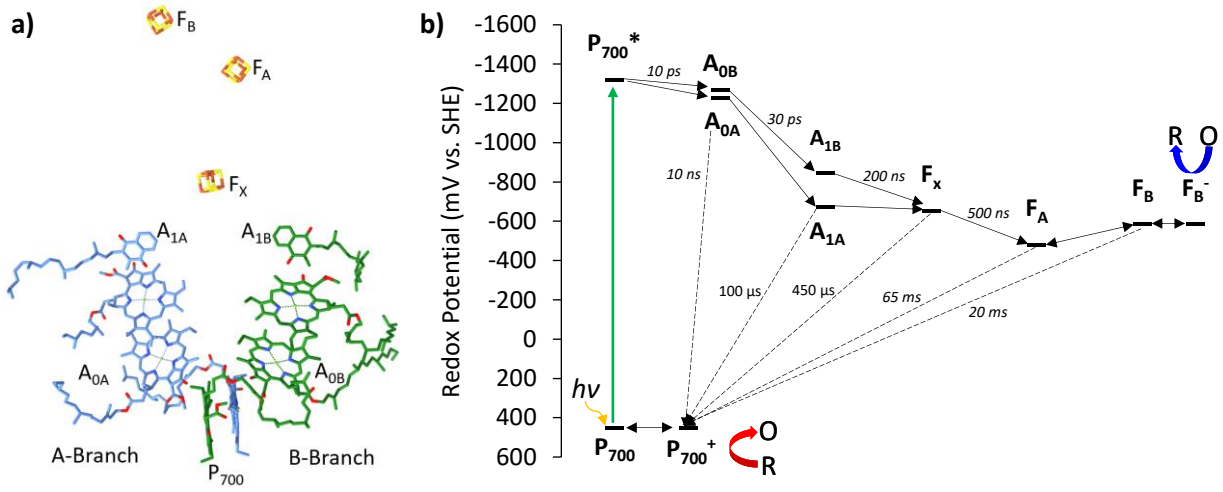

Figure 1.2: a) Depiction of PSI electron transport chain sites. b) Electron transport chain potentials and speed of electron transfer and recombination. Adapted from Bruce et al.[7]

The versatility of PSI along with its abundance and ease of extraction has led scientists to use it in many applications such as hydrogen production, photobioelectrodes, dye-sensitized solar cells, and solid-state solar cells. In these investigations, aside from solid-state work, the redox capabilities of PSI are leveraged to form desired products or improve photochemical performance.[8–16] In the solid-state applications, the rapid turnover and voltage differential are used to increase performance of the devices while in liquid applications, the asymmetry of PSI redox capabilities are leveraged for enhanced photocurrent generation. Different approaches to using the robust redox properties are explored in Chapters 3-5 of this dissertation, and a summary of this work and an outlook for integration of PSI in biohybrid applications is presented in Chapter 6.

Transition from Liquid Cells

Photoelectrochemical investigations of PSI have commonly employed the use of a three-electrode liquid cell, which is traditionally used to examine reactions occurring at a single electrode by applying a potential at the electrode. These types of cells are best utilized for studying

fundamental electrochemistry, but they cannot be used for applied devices. Two-electrode cells, on the other hand, can be liquid- or solid-state and are used to investigate performance across the two electrodes instead of focusing on reactions occurring at one electrode, making them much more suitable for applied systems. The major difference between the two types of cells is the presence of a reference electrode that operates at a well-known and specific potential that serves as a reference for potential, similar to sea level serving a reference for elevation measurements. For two-electrode experiments, the counter electrode also serves as the reference electrode, so potentials are measured across the cell. The experimental setups for both types of cells are shown in Figure 1.3.

In liquid cells, unless a PSI reaction site is wired directly to an electrode, the electrochemical reactions for PSI are dependent on mediated electron transfer (MET) mechanisms, which require redox species to diffuse to the protein reaction sites for electron transfer to occur. Alternatively, solid-state devices with PSI depend on direct electron transfer (DET) between electrodes where electrons require a conductive path from the cathode to the anode to function. For PSI systems involved in DET, there needs to be direct connection between the P_{700} and F_B sites, which places elevated requirements on cell fabrication.

Three-electrode cells have been used to enable a focused study of the effect of PSI films on electrode performance.[7,10,17] Additionally, PSI has been incorporated in solid-state devices using electron-conducting materials such as polyviologen,[15] polyaniline,[16] tyrosine,[18] fullerenes,[18,19] LiF,[19,20] and PEDOT:PSS.[20] A common challenge with PSI integration in solid-state devices is directly connecting conducting material to the F_B and P_{700} reaction sites. Performing DET at the P_{700} site is particularly difficult to because it is buried in a lumenal pocket

that is hard to access, and any unconnected protein in a solid-state system would only act as an insulator and decrease the overall efficiency of the system.

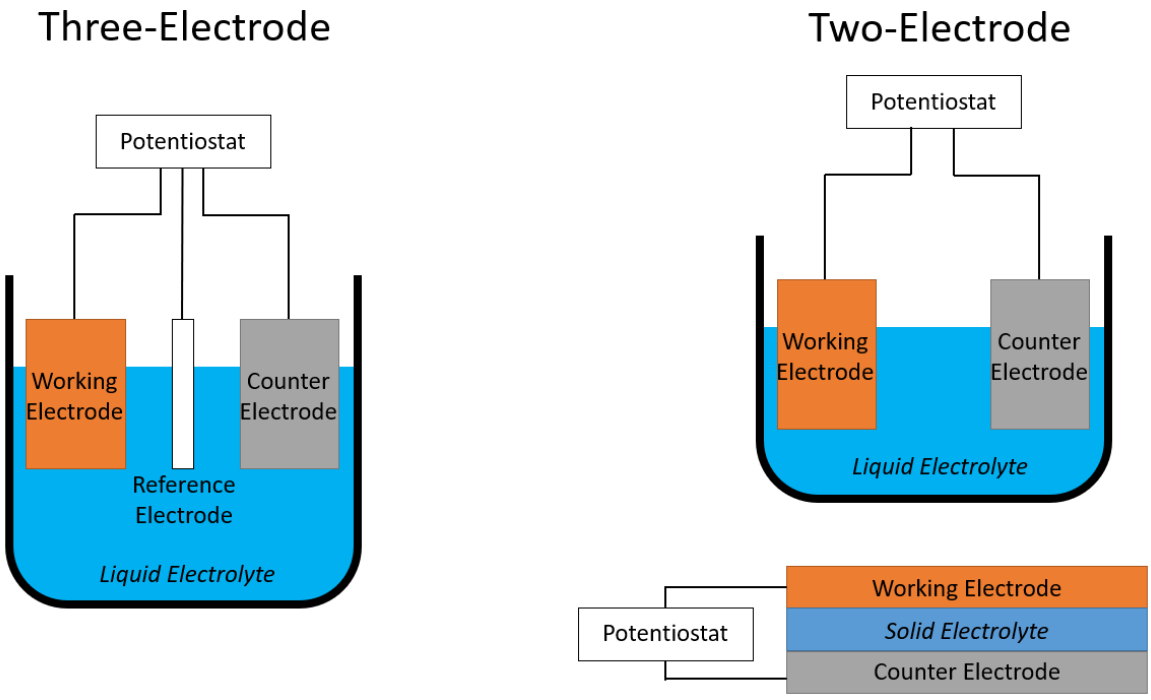

Figure 1.3: Experimental setup for three-electrode and two-electrode cells. The two cells on the right show a liquid-state (top) and solid-state (bottom) setup.

In Chapter 3 of this work, a two-electrode gel-based dye-sensitized solar cell device that utilizes the asymmetry of PSI redox reactions to enhance performance is presented. The use of a gel-based cell allows for PSI to perform within a MET system that utilizes a two-electrode setup, resulting in a well-performing system that can serve as a stand-alone biophotovoltaic device. The ability to perform MET in a two-electrode cell enables asymmetry of PSI redox capabilities to boost performance with careful selection of PSI placement and mediator selection. A reaction-diffusion model of the electrochemical kinetics of PSI interacting with an ascorbic acid (AscH) and 1,2-dichlorophenolindophenol (DCPIP) mediator system is also explored. The model can be used to simulate PSI performance in various electrochemical cell setups and determine limitations for protein multilayer films.

Photosystem I Protein-Polymer Conjugates

Protein-polymer conjugates are a unique class of biohybrid materials that offer the combination of properties of both synthetic polymers and biomolecules. These conjugates have been used to advance research in a wide range of fields such as medicine,[21] enzymatic performance,[22] muscle-inspired actuators,[23] and catalysis.[24]

Traditional approaches to forming protein-polymer conjugates involve either grafting intact polymers to the target protein or attaching a polymerization initiator that can spur the growth of polymer from the protein upon exposure to a suitable monomer. Grafting to proteins involves the reaction of a functionalized polymer with an active group on the protein, which often results in low yield due to the large size of the molecules and the constraints on concentrations.[24,25] Grafting from the protein is compatible with common polymerization techniques such as ATRP, RAFT, and ring-opening polymerization.[25–27] In these conjugation methods, either a protein that has been modified or a functionalized polymer is needed for successful connection, resulting in more complex processes for successful conjugation.

PSI research has mostly focused on improving the photoelectrochemical performance of materials[7,28–31] as well as producing hydrogen.[12,13,32] The protein complex has been interfaced with conducting polymers in multiple applications. A common constraint for PSI-polymer systems is the dependence on MET to small redox species because of a lack of direct connection to the active sites for DET.[16,20,33] To ensure connection, protein-polymer conjugates have been formed by other groups using a modified protein complex with an attached polymer at the F_B site for the purpose of hydrogen production.[13,34] In most of this research, there has been a focus on the overall photochemical redox capabilities of PSI or the robust reductive capability of the F_B site. The

oxidative capabilities of the P_{700} site are also robust, and the P_{700} site has appropriate potentials favorable to perform oxidative polymerizations,[35] such as with pyrrole.

In Chapter 4 of this dissertation, a novel route for protein-polymer conjugates using PSI to polymerize an electroactive monomer is presented. Specifically, unmodified Photosystem I (PSI) protein complexes are demonstrated to directly polymerize pyrrole monomer to form PSI-polymer conjugates via oxidative polymerization at the P_{700} reaction site. This polymerization technique is the first reported photoactive protein-polymer conjugate where the polymer was formed by an unmodified protein. This technique could be expanded by using other monomers to tailor conjugate functionality. The ability to create protein-polymer conjugates to combine the photo-redox properties of PSI with special properties of the polymer should facilitate the generation of inexpensive, biohybrid solar conversion technology.

Photosystem I in Conducting Polymer Matrix

Embedding PSI within a polymer matrix to provide more direct connections to donate or accept electrons from PSI has been explored in multiple systems. Badura *et al*. entrapped PSI within an Os-containing redox polymer hydrogel and serve as an electron donor to immobilized PSI in an electrochemical cell.[36] Similarly, Gizzie *et al*. entrapped PSI in a polyaniline (Pani) matrix by electropolymerizing a solution of aniline and PSI on a gold electrode, showing a significant improvement over PSI multilayers in a wet cell. The Pani-PSI matrix was also shown to maintain similar performance over 16 days.[37] Vapor-phase polymerization of poly(3,4-ethylenedioxythiophene) (PEDOT) within multilayer PSI films showed enhanced film pseudo-capacitance up to a limiting thickness of PSI before the protein blocked polymer connection to the electrode, lowering performance.[38]

PSI has also been interfaced with conducting polymer matrices into solid-state devices to help move away from liquid devices. One of the first PSI-integrated solid-state devices was published in 2014 by Gordiichuck *et al.* The device was made in layers by depositing a monolayer of PSI on top of a TiO_2 semiconductor anode with polytriarylamine as a conducting layer and capped with a MoO_3/Al cathode. This initial device achieved a maximum external quantum efficiency of just under 0.007% at a measured wavelength of ~660 nm.[19] A similar layered approach was taken by Kazemzadeh *et al*.[20] and Dervishogullari *et al*.[15] where multilayers of PSI were used as a solid layer and PEDOT: PSS and polyviologen, respectively, were used as conducting polymer layers to better align energetically with PSI redox potentials. More recently, Wolfe *et al*. expanded on the layered approach by alternating monolayers of PSI and PEDOT:PSS to show that the liquid electrochemical performance reaches a maximum performance after depositing 6-layer pairs and noted that this principle should hold for a solid-state equivalent.[39]

To improve connection in solid-state applications, Gizzie *et al*. explored using films of Pani-PSI that were electropolymerized directly from an aniline and PSI solution as a solid-electrolyte layer.[16] This approach improves connections between the polymer and protein compared to the layering systems, but the concentration of PSI entrapped within the film was estimated to be very low at approximately 15 nmol/cm^3. The device was also shown to retain over 85% of the original photocurrent output over 20 days. Solid-state devices are expected to retain performance longer than liquid analogues because PSI readily creates reactive oxygen species that degrade the protein in aqueous solutions in the absence of antioxidants.[40]

In Chapter 5, an approach is explored to embed high concentrations of PSI into a conducting polymer matrix that can be used for both liquid and solid-state applications. In this work, a multilayer film of PSI is deposited onto a gold surface, and polypyrrole is

electrochemically polymerized from the electrode, growing through free volume within the protein film. This method allows for high concentrations of protein within the film, polymer that is connected to the electrode by definition, and direct connections between the proteins and the polymer to increase performance. The polymerization kinetics and effect of polymer thickness are examined to find optimal performance conditions.

References

1. Kabir, E., Kumar, P., Kumar, S., Adelodun, A. A. & Kim, K. H. Solar energy: Potential and future prospects. *Renew. Sustain. Energy Rev.* **82**, 894–900 (2018).
2. Bolton, J. R. & Hall, D. O. Photochemical Conversion and Storage of Solar Energy. *Annu. Rev. Energy* **4**, 353–401 (1979).
3. British Petroleum Company. *BP Statistical Review of World Energy*. *Statistical Review of World Energy* **67**, (2018).
4. Brettel, K. & Leibl, W. Electron transfer in photosystem I. *Biochim. Biophys. Acta - Bioenerg.* **1507**, 100–114 (2001).
5. Brettel, K. Electron transfer and arrangement of the redox cofactors in photosystem I. *Biochimica et Biophysica Acta - Bioenergetics* **1318**, 322–373 (1997).
6. Suga, M. *et al.* Structure of the green algal photosystem I supercomplex with a decameric light-harvesting complex I. *Nat. Plants* **5**, 626–636 (2019).
7. Nguyen, K. & Bruce, B. D. Growing green electricity: Progress and strategies for use of Photosystem I for sustainable photovoltaic energy conversion. *Biochim. Biophys. Acta - Bioenerg.* **1837**, 1553–1566 (2014).
8. Yu, D. *et al.* Enhanced photocurrent production by bio-dyes of photosynthetic macromolecules on designed TiO_2 film. *Sci. Rep.* **5**, (2015).

9. Frolov, L., Wilner, O., Carmeli, C. & Carmeli, I. Fabrication of oriented multilayers of photosystem I proteins on solid surfaces by auto-metallization. *Adv. Mater.* **20**, 263–266 (2008).

10. Ciesielski, P. N. *et al.* Photosystem I-Based biohybrid photoelectrochemical cells. *Bioresour. Technol.* **101**, 3047–3053 (2010).

11. Heifler, O., Carmeli, C. & Carmeli, I. Enhanced Optoelectronics by Oriented Multilayers of Photosystem I Proteins in Dry Hybrid Bio-Solid Devices. *J. Phys. Chem. C* **122**, 11550–11556 (2018).

12. Leblanc, G., Chen, G., Jennings, G. K. & Cliffel, D. E. Photoreduction of catalytic platinum particles using immobilized multilayers of Photosystem I. *Langmuir* **28**, 7952–7956 (2012).

13. Lubner, C. E., Grimme, R., Bryant, D. A. & Golbeck, J. H. Wiring photosystem I for direct solar hydrogen production. *Biochemistry* **49**, 404–414 (2010).

14. Gizzie, E. A. Enhancing Electron Transfer at the Protein/Electrode Interface: Applications in Bioderived Solar Energy Conversion and Electrochemical Biosensors. (2017).

15. Dervishogullari, D., Gizzie, E. A., Jennings, G. K. & Cliffel, D. E. Polyviologen as Electron Transport Material in Photosystem I-Based Biophotovoltaic Cells. *Langmuir* **34**, 15658–15664 (2018).

16. Gizzie, E. A. *et al.* Photosystem I-polyaniline/TiO_2 solid-state solar cells: simple devices for biohybrid solar energy conversion. *Energy Environ. Sci.* **8**, 3572–3576 (2015).

17. LeBlanc, G., Gizzie, E. A., Yang, S., Cliffel, D. E. & Jennings, G. K. Photosystem I Protein Films at Electrode Surfaces for Solar Energy Conversion. *Langmuir* **30**, 10990–11001 (2014).

18. Zeynali, A., Ghiasi, T. S., Riazi, G. & Ajeian, R. Organic solar cell based on photosystem I

pigment-protein complex, fabrication and optimization. *Org. Electron. physics, Mater. Appl.* **51**, 341–348 (2017).

19. Gordiichuk, P. I. *et al.* Solid-state biophotovoltaic cells containing photosystem i. *Adv. Mater.* **26**, 4863–4869 (2014).

20. Kazemzadeh, S., Riazi, G. & Ajeian, R. Novel Approach of Biophotovoltaic Solid State Solar Cells Based on a Multilayer of PS1 Complexes as an Active Layer. *ACS Sustain. Chem. Eng.* **5**, 9836–9840 (2017).

21. Grigoletto, A., Tedeschini, T., Canato, E. & Pasut, G. The evolution of polymer conjugation and drug targeting for the delivery of proteins and bioactive molecules. *Wiley Interdiscip. Rev. Nanomedicine Nanobiotechnology* **13**, 1–33 (2021).

22. Thiele, M. J. *et al.* Enzyme-Polyelectrolyte Complexes Boost the Catalytic Performance of Enzymes. *ACS Catal.* **8**, 10876–10887 (2018).

23. Chen, C., Ng, D. Y. W. & Weil, T. Polymer bioconjugates: Modern design concepts toward precision hybrid materials. *Prog. Polym. Sci.* **105**, 101241 (2020).

24. Li, X. *et al.* Highly active enzyme–metal nanohybrids synthesized in protein–polymer conjugates. *Nat. Catal.* **2**, 718–725 (2019).

25. Gauthier, M. A. & Klok, H. A. Peptide/protein-polymer conjugates: Synthetic strategies and design concepts. *Chem. Commun.* 2591–2611 (2008). doi:10.1039/b719689j

26. Liu, X. & Gao, W. Precision Conjugation: An Emerging Tool for Generating Protein–Polymer Conjugates. *Angew. Chemie - Int. Ed.* **60**, 11024–11035 (2021).

27. Pelegri-O'Day, E. M. & Maynard, H. D. Controlled Radical Polymerization as an Enabling Approach for the Next Generation of Protein-Polymer Conjugates. *Acc. Chem. Res.* **49**, 1777–1785 (2016).

28. Baker, D. R., Simmerman, R. F., Sumner, J. J., Bruce, B. D. & Lundgren, C. A. Photoelectrochemistry of photosystem I bound in Nafion. *Langmuir* **30**, 13650–13655 (2014).

29. Chen, W.-L., Gross, E. L. & Pan, R. L. A Photoelectrochemical Cell Using Electrodes Modified by Photosystem I Particles of Spinach. *Bot. Bull. Acad. Sin.* **33**, 9–15 (1991).

30. Passantino, J. M., Wolfe, K. D., Simon, K. T., Cliffel, D. E. & Jennings, G. K. Photosystem I Enhances the Efficiency of a Natural, Gel-Based Dye-Sensitized Solar Cell. *ACS Appl. Bio Mater.* **3**, 4465–4473 (2020).

31. Wolfe, K. D. *et al.* Photosystem I Multilayers within Porous Indium Tin Oxide Cathodes Enhance Mediated Electron Transfer. *ChemElectroChem* 1–9 (2019). doi:10.1002/celc.201901628

32. Krassen, H. *et al.* Photosynthetic hydrogen production by a hybrid complex of photosystem I and [NiFe]-hydrogenase. *ACS Nano* **3**, 4055–4061 (2009).

33. Saboe, P. O. *et al.* Biomimetic wiring and stabilization of photosynthetic membrane proteins with block copolymer interfaces. *J. Mater. Chem. A* **4**, 15457–15463 (2016).

34. Grimme, R., Lubner, C., Bryant, D. & Golbeck, J. Photosystem I/molecular wire/metal nanoparticle bioconjugates for the photocatalytic production of H2. *Chemtracts* **21**, 207–209 (2008).

35. Sadki, S., Schottland, P., Brodie, N. & Sabouraud, G. The mechanisms of pyrrole electropolymerization. *Chem. Soc. Rev.* **29**, 283–293 (2000).

36. Badura, A. *et al.* Photocurrent generation by photosystem 1 integrated in crosslinked redox hydrogels. *Energy Environ. Sci.* **4**, 2435–2440 (2011).

37. Gizzie, E. A., Leblanc, G., Jennings, G. K. & Cliffel, D. E. Electrochemical preparation of

photosystem I-polyaniline composite films for biohybrid solar energy conversion. *ACS Appl. Mater. Interfaces* **7**, 9328–9335 (2015).

38. Robinson, M. T., Simons, C. E., Cliffel, D. E. & Jennings, G. K. Photocatalytic photosystem I/PEDOT composite films prepared by vapor-phase polymerization. *Nanoscale* 6158–6166 (2017). doi:10.1039/C7NR01158J

39. Wolfe, K. D. *et al.* Layer-by-Layer Assembly of Photosystem I and PEDOT:PSS Biohybrid Films for Photocurrent Generation. *Langmuir* **37**, 10481–10489 (2021).

40. Wolfe, K. D. *et al.* Improving the Stability of Photosystem I-Based Bioelectrodes for Solar Energy Conversion. *Curr. Opin. Electrochem.* **19**, 27–34 (2019).

Chapter 2

Experimental and Analytical Techniques

Materials Preparation

PSI Protein Extraction and Isolation

Extraction of PSI protein complexes from spinach was done using a procedure adapted from Reeves and Hall[1] and Shiozawa *et al*.[2] The major steps of the extraction process are shown in Figure 2.1, and the steps are described in more detail below:

1. Fresh baby spinach purchased from a local supermarket was de-veined and then homogenized in a blender with a grinding medium to break open plant cell walls.
2. The blended mixture was filtered through cheesecloth to remove large solids such as remaining stem material and cellulose that does not contain PSI proteins.
3. The liquid filtrate was then centrifuged at 8,000 RCF. PSI is located in the thylakoids, which are heavier than other components of the plant cell. The thylakoids were separated into the solid pellet upon centrifugation while the supernatant that contains other cell materials was decanted for removal.
4. A lysing solution containing surfactant was added to the pellet, and the two were mixed to facilitate the lysing of the thylakoids. The surfactant breaks apart the thylakoid membrane and solubilizes PSI along with other thylakoid materials.
5. The solution was centrifuged at 20,000 RCF to pellet out undesired parts of the lysed thylakoids. The solubilized PSI proteins and other organelles remain in the supernatant after centrifugation.
6. The supernatant was loaded onto a hydroxyapatite ion-exchange column that selectively adsorbs PSI and allows other organelles to flow through.

7. The column was washed with column buffer to remove any excess material that was not adsorbed to the hydroxyapatite.
8. Elution buffer was flowed through the column to remove PSI from the column and was collected as the final extraction product.
9. A) The concentration of the PSI extract was estimated by Baba's assay or chlorophyll quantification if desired.[3] B) The PSI extract was stored at -80 °C until use.
10. If removal of surfactant and excess salt from the PSI extract was desired, the solution was dialyzed in deionized water at a 1000:1 volume ratio for 12 h in a 10,000 MWCO membrane before use.

Composition of the grinding medium, lysing solution, column buffer, and elution buffer can be found in Reeves and Hall and Shiozawa *et al*.

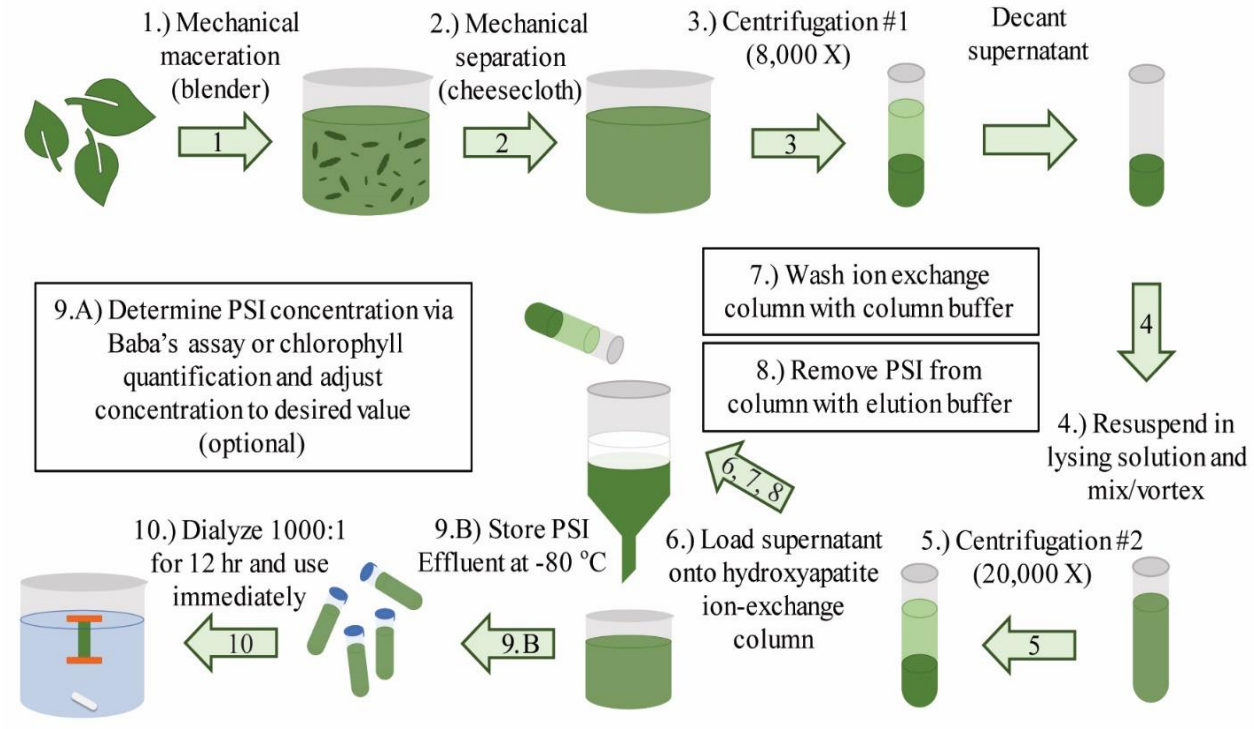

Figure 2.1: PSI extraction process steps. Image by Kody Wolfe.

Deposition of PSI Multilayer Films

PSI multilayer films in this work were all deposited using a vacuum-assisted drop casting method. To prepare the films, an electrochemical mask was placed on the desired substrate and flattened. A hole of 0.24 cm^2 was cut out from the mask to yield consistent active areas for the resulting films. Dialyzed PSI solution was deposited on the substrate and placed under vacuum to increase the drying rate of the film. A multilayer film of PSI remained after evaporation of all the water. Once dry, the films were rinsed in water to remove excess any excess salt and then dried under vacuum again. Dialyzed PSI solution must be used to form multilayer films because if surfactant is drop-cast with the protein, then protein is solubilized by the surfactant upon exposure to water, and only a monolayer of protein remains.[4] The thickness of the resulting films was tuned by changing the area of the exposed substrate under the electrochemical mask or varying the concentration or volume of PSI drop-cast onto the surface.

Gel Cell Preparation

The quasi-solid-state gel cells comprised of layers of FTO, dye-sensitized TiO_2, PSI, agarose, and copper were fabricated by the following method. First, FTO substrates (MTI Corporation) were rinsed with ethanol and dried under a stream of nitrogen. The substrates were then treated with ozone plasma under vacuum for 15 min to create a hydrophilic surface. TiO_2 paste (Dyesol 18NR-T) was mixed in a 1:3 (v:v) ethanol solution and spin-coated onto FTO at 1,500 rpm for 30 s. The films were then sintered at 500 °C in a muffle furnace for 30 min and cooled overnight.

To dye-sensitize the TiO_2 substrate, 20 g of commercially available blackberries were crushed in a mortar by pestle and mixed with 20 mL of ethanol. Solids were filtered from the

mixture, and the TiO_2 films were left in the dye solution for 12 h.[5] The dyed films were rinsed in ethanol and dried under nitrogen before use.

For the gel electrolyte, aqueous based electrolyte solutions of AscH and DCPIP (in a ratio of 20 mM AscH to 1 mM DCPIP) were used with AscH concentrations ranging from 2 to 200 mM. For devices at lower pH, 100 mM KCl served as the supporting electrolyte, while at neutral pH, 100 mM monobasic phosphate was the electrolyte. Agarose was added to each liquid electrolyte at 0.5 wt% and then stirred and heated to 120 °C. The medium was cooled and formed an electrolyte gel.

For the copper cathode, an insulating mask with a 0.28 cm^2 hole was placed on the copper, a duplicate mask was placed on TiO_2, and 50 μL of dialyzed PSI was drop-cast onto the copper into the exposed area made by the mask. The PSI was then dried under vacuum for 30 min, leaving a multilayer film of randomly oriented PSI protein complexes.

Agarose gel (100 μL) was placed within the opening of the mask on the metal substrate, with or without a PSI multilayer previously deposited. The FTO slide with the TiO_2 was then pressed on top of the cathode and bound with binder clips to form the device.

PSI-Polypyrrole (PPy) Conjugate Photopolymerization

Photopolymerization was carried out by adding pyrrole monomer into a solution of ~4 μM PSI and 1.0 M $NaClO_4$ to a concentration of 0.5 M pyrrole and mixing with an ultrasonicator until all pyrrole was solubilized. The mixture was then illuminated using a Newport Xenon Arc Lamp Solar Simulator set to 100 W power. Illumination times varied from 3 to 24 h, depending on the sample. Every sample was dialyzed to remove unreacted monomer and excess salt before characterization. The resulting conjugates were then either dialyzed to remove unreacted monomer

before being drop-cast to form multilayer films or filtered and rinsed to form a powder for solid-state characterization.

PPy Electropolymerization around PSI Multilayers

PSI was first dialyzed, and then it was deposited and dried on a gold substrate via drop-casting and was then placed in an electrochemical cell with a 0.5 M pyrrole solution with 1.0 M $NaClO_4$ as a doping electrolyte. To perform the polymerization, the gold electrode was biased to a set potential to initiate electropolymerization of pyrrole on the gold surface, and a set amount of charge was applied to ensure consistent amounts of polymer were formed.

Electrochemical Characterization

Photochronopotentiometry (PCP) & Photochronoamperometry (PCA)

In this work, photoactivity of PSI protein films is measured through analytical electrochemical techniques. PCP and PCA serve as one of the main identifiers of photoactivity in this work. PCP is a specialized form of chronopotentiometry, wherein a working electrode is held at a constant current of 0 A and the potential is measured. This potential is the open-circuit potential (OCP) of an electrode. Alternatively, PCA is a specialized form of chronoamperometry, wherein a working electrode is held at a measured open-circuit potential and the current passed through the electrode is measured over time. For PCP and PCA experiments, working electrodes are held either at a net current of 0 A or at the OCP measured in dark conditions, and the potential or current response, respectively, of the electrode is measured upon illumination of the electrode.

In electrochemical systems, current and potential can be measured using a three-electrode chemical cell that has a working electrode, reference electrode, and counter electrode. In this system, the working electrode is the electrode under examination, and potential is applied to it to measure oxidation and reduction reactions. The reference electrode contains a redox mediator of

known potential, such as the Ag/AgCl couple, that serves as a reference to measure the potential at the working electrode. The counter electrode is an inert electrode, typically a platinum mesh, that is able to perform oxidations or reductions counter to the working electrode to ensure a charge balance is maintained in the cell.

In an electrochemical reaction, there are oxidized species (O) that are reduced at the cathode and reduced species (R) that are oxidized at the anode. The potential of an electrode in an electrochemical cell is related to the concentration of O and R species near the electrode surface and is governed by the Nernst equation:

$$E(t) = E^{0'} + \frac{RT}{F} \ln \frac{C_O(0,t)}{C_R(0,t)} \quad [2\text{-}1]$$

where $E(t)$ is the electrode potential, $E^{0'}$ is the formal potential of the electrode at standard conditions, R is the universal gas constant, T is temperature, F is Faraday's constant, $C_o(0,t)$ is the concentration of O species at the electrode surface, and $C_R(0,t)$ is the concentration of R species at the electrode surface. In this work, the DCPIP/AscH is the most often used redox mediator to transfer charge and is further discussed in Chapter 3.

The current in an electrochemical cell is dependent on electron transfer between the O and R species and the electrode. In a cell with no convection, current is diffusion controlled because O and R must diffuse to an electrode before they can be reduced or oxidized. In this scenario, the current-time relationship behaves under "Cottrell conditions" and can be measured by the Cottrell equation:[6]

$$i(t) = nFAC^* \left(\frac{D}{\pi t}\right)^{\frac{1}{2}} \quad [2\text{-}2]$$

where $i(t)$ is the current at a given time, n is the number of electrons transferred, F is Faraday's constant, A is the surface area of the electrode, C^* is the bulk concentration of oxidized

or reduced species, D is the diffusion coefficient for the redox mediators. Cottrellian current has an initial spike in current known as the peak current, i_p, that then has a diffusional tail until it reaches a steady state current.

In electrochemical cells with PSI, protein multilayers are deposited on a working electrode. Upon illumination, the proteins perform rapid oxidations and reductions. In PSI integrated systems, the dominant redox reactions are:

$$P_{700}^{+} + R \rightarrow P_{700} + O \quad [2\text{-}3]$$

$$F_B^{-} + O \rightarrow F_B + R \quad [2\text{-}4]$$

These rapid redox reactions change the concentration of O and R species near the surface, which changes both the potential and current at the electrode. The response in current or potential to light is what is being measured in PCP and PCA, and representative curves for each experiment are shown in Figure 2.2. In this work, photoactivity of PSI-integrated systems are measured by PCP and PCA in Chapters 3, 4, and 5. In Chapter 3, a two-electrode cell is used and performs under different conditions than a three-electrode cell and is explained in more detail in the discussion of the reaction-diffusion model created for that system.

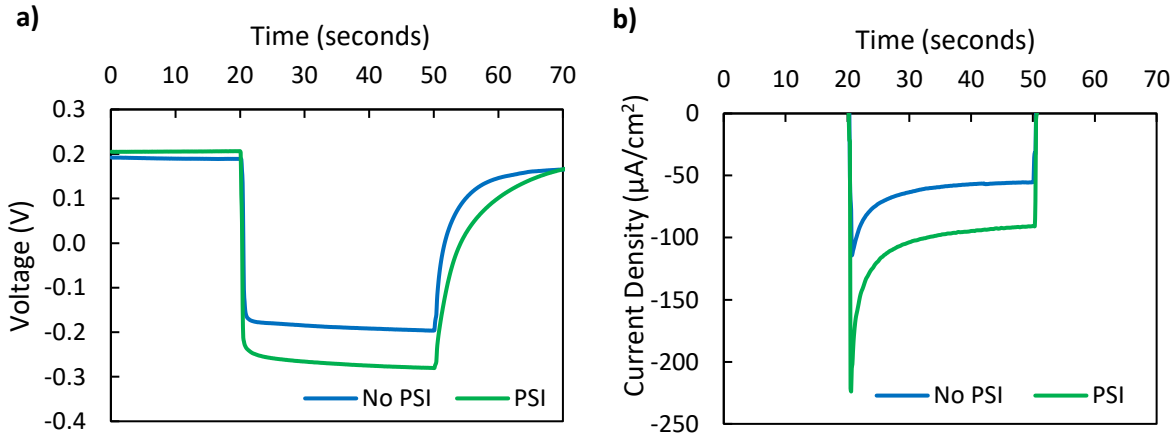

Figure 2.2: a) PCP and b) PCA curves of copper substrates with and without PSI multilayer films in 20 mM AscH: 1 mM DCPIP mediator.

j-V & Power Curves

Forward and reverse scan j-V (current-potential) curves were measured to determine the power output of the completed devices in Chapter 3. In a j-V curve, the current is measured as the potential across a two-electrode device is scanned between the OCP and 0 V. The current when the potential is 0 is known as the short-circuit current (J_{SC}). A forward scan starts at J_{SC} and scans to OCP, and a reverse scan does the opposite. The power output of the cell can be measured at any given potential by calculating the product of the current and potential. For the forward and reverse scans, the important photovoltaic parameters (fill factor (FF), $J_{SC,}$ OCP, and external quantum efficiency (η)) were measured for each scan. To determine a measure of steady-state device performance in Chapter 3, the forward and the reverse scans with and without PSI were averaged. A maximum power-point voltage was found from the averaged power curves, and steady-state power generation was measured at the maximum power-point voltage to obtain an accurate power output.

Cyclic Voltammetry (CV)

Cyclic voltammetry is a potential sweeping electrochemical experiment that repeatedly scans the potential at the working electrode from one set potential to another and back. The goal of cyclic voltammetry is to probe the redox behavior of a target molecular species by looking at its change in reduction potential and the magnitude of current produced during the scans. In Chapter 3, the behavior of the redox molecule, DCPIP, is investigated by CV to determine the pH in which the species is most electrochemically active.

Electrochemical Impedance Spectroscopy (EIS)

EIS is an electrochemical technique that measures current as the potential of the working electrode is varied in a sinusoidal manner at changing frequencies. The alternating current behavior

at various potentials can be used to determine the impedance behavior of the working electrode, which allows for the measurement of various parameters such as resistance and capacitance. Impedance is of an electrochemical system *Z* is calculated by:

$$Z = \frac{E(t)}{I(t)} \frac{E_o \sin(2\pi f t)}{I_o \sin(2\pi f t + \Phi)} \quad [2\text{-}5]$$

where *E(t)* is the applied potential at time *t*, *I(t)* is the measured current at time *t*, E_o is potential amplitude, I_o is current amplitude, f is the frequency, *t* is time, and Φ is the phase shift. Z is also related to the resistance and capacitance of a film on a surface by:

$$|Z| = \sqrt{R^2 + \left(\frac{1}{j2\pi f C}\right)^2} \quad [2\text{-}6]$$

where *R* is the film resistance, *j* is the square root of -1, *f* is frequency, and *C* is capacitance. Impedance is affected by the transport of redox mediators and ions to reach the working electrode to donate or accept electrons. The presence of films can significantly alter these diffusional processes. The changing the frequency allows more (lower frequencies) or less time (higher frequencies) for diffusion of these mediators and ions to occur. A high impedance indicates that electron carrying species have impeded transport to the working electrode, signaling a higher film resistance and/or low capacitance.

The results of an EIS experiment can be shown as either a Bode or Nyquist plot. A Bode plot shows the impedance values at different frequencies and can give information about the charge-transfer resistance of the electrode or ion transfer resistance of a film, the interfacial capacitance of the film or surface, and solution resistance by examining low, medium, and high frequencies, respectively. The areas of interest in a Bode plot are shown in Figure 2.3. These parameters can then be used to create an equivalent circuit of the electrochemical cell.

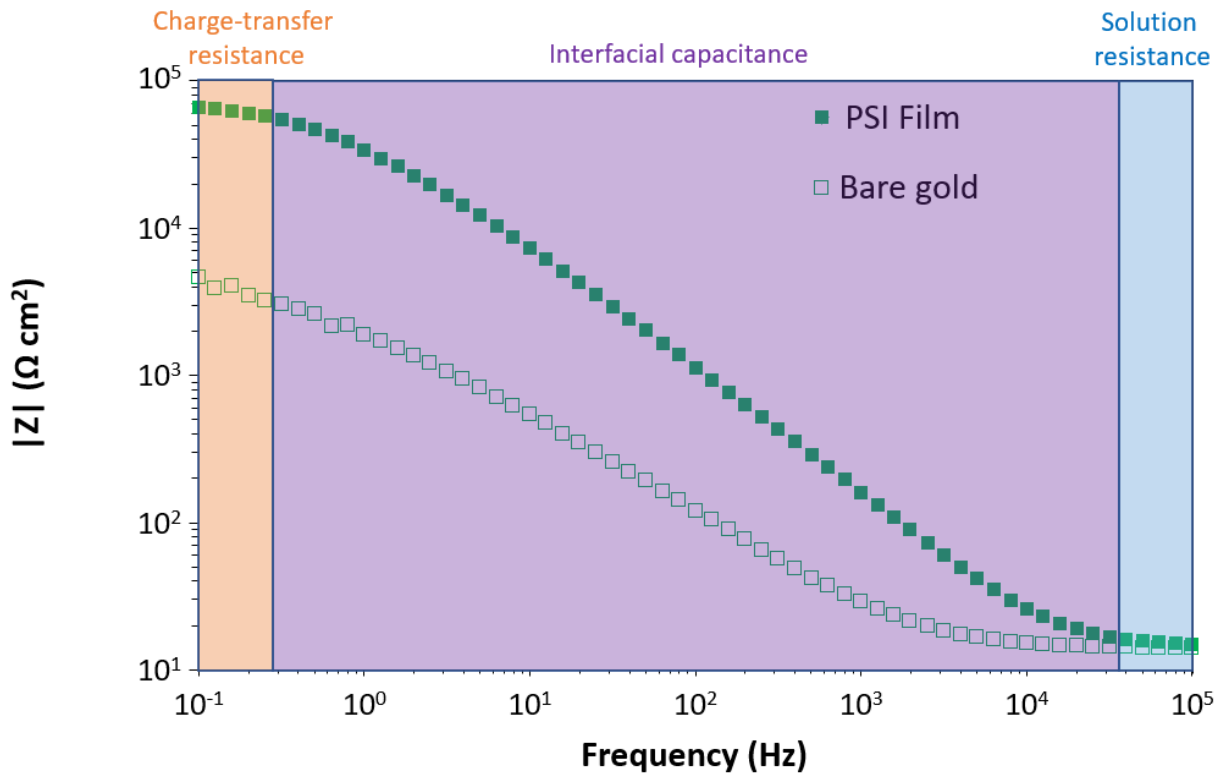

Figure 2.3: Bode plot of a gold substrate with and without a PSI multilayer film in a KCl electrolyte. |Z| is the measured impedance at a given frequency.

EIS is used to measure film properties for surfaces with and without PSI multilayers deposited to determine the resistance and capacitance of the films. Figure 2.3 shows an increase in impedance and charge transfer resistance of a gold electrode after the deposition of a PSI film because the film is blocking ions from diffusing to the electrode surface to accept or donate electrons.

Equipment

All PCP, PCA, and CV experiments were carried out on a CH Instruments 660a electrochemical workstation, and EIS and conductivity measurements were measured on a Gamry Reference 600 potentiostat. Ag/AgCl was used as the reference electrode and a platinum mesh was used as the counter electrode for all three-electrode experiments. Photoactivity measurements were made using a Leica KL 2500 LCD cold light source.

Other Characterization Methods

Attenuated Total Reflection-Fourier Transform Infrared Spectroscopy (ATR-FTIR)

ATR-FTIR analysis is a spectroscopic technique that can be used to identify the composition of a film based on its absorbance of infrared light. An IR beam is directed into the side of an ATR crystal at a set angle. The crystal then reflects the light to contact the sample, which needs to be in contact with the crystal to eliminate any reflectance effects by air. The sample absorbs energy and alters or attenuates the beam and reflects it back into the crystal, and this pattern repeats until the beam exits the other side of the crystal and is analyzed in a detector. An IR spectrum of the collected beam is generated by applying a Fourier transform on the raw interferogram data. Bonds of different types between different elements each absorb light at specific wavelengths, so measuring the light that is absorbed by the sample yields a fingerprint of what bonds and elements are present. A simplified visualization of the technique is shown in Figure 2.4.

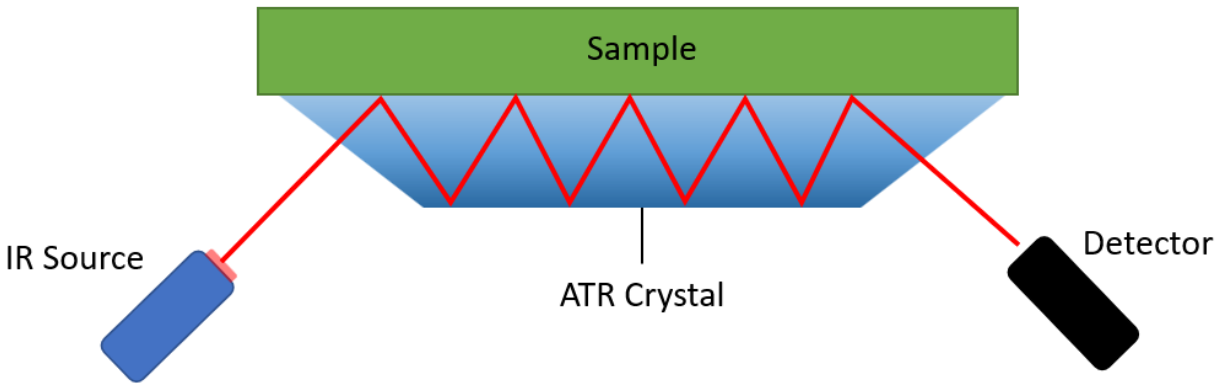

Figure 2.4: IR beam pathway through ATR crystal during an ATR-FTIR measurement.

ATR-FTIR is used in this work to identify components of the films being studied and to check if there is significant degradation of the protein structure by seeing if peaks of the protein shift and widen or narrow, signaling a change in structure. The technique is used in Chapters 4 and

5 to confirm the presence of both PSI and PPy in films. The FTIR used in this work is a Nicolet 6700 FTIR at 4 cm^{-1} resolution.

Scanning Electron Microscopy-Energy Dispersive X-Ray Spectroscopy (SEM-EDS)

SEM is an imaging technique that involves rastering a focused beam of electrons on a sample under vacuum to generate a high-resolution image at the nanoscale. When electrons hit the sample, secondary electrons, backscattered electrons, and X-rays are ejected from the surface and are picked up by a detector to convert them into a signal that can generate an image. This technique is used in Chapter 4 to identify the morphology of polymers and protein-polymer conjugates at the nanoscale.

EDS analysis is used to identify elements within a sample that is being imaged in an SEM. EDS uses the X-rays that are generated and ejected from the sample after being struck by an electron from the electron beam. Every element has an X-ray of unique energy that can be used to identify elemental composition in an SEM image. This technique is to confirm successful doping of PPy in Chapter 4 by confirming the presence of the doped element in the reaction product. The SEM used in this work is a Zeiss Merlin SEM with an accelerating voltage of 2.00 kV.

Contact angle

When a liquid comes into contact with a solid surface, molecular properties of the surface, air, and the liquid dictate the shape of the liquid on the surface. The static contact angle between the solid-liquid interface and the line tangent to the liquid profile at the three-phase contact line can be measured to assess the relative surface energy of the solid material. A force balance of the interfacial forces between the three phases affect the contact angle as described by the Young equation:

$$\gamma_{SV} - \gamma_{SL} = \gamma_{LV} \cos\theta \quad [2\text{-}7]$$

where γ_{SV} is the interfacial tension at the solid-vapor interface, γ_{SL} is the interfacial tension at the solid-liquid interface, γ_{LV} is the interfacial tension at the liquid-vapor interface, and θ is the static contact angle.

Contact angle measurements are typically used to measure the hydrophilicity/hydrophobicity or oleophilicity/oleophobicity of a surface. Hydrophilic and oleophilic surfaces will have low contact angles for water and oils, respectively, while hydrophobic and oleophobic surfaces will yield high contact angles.

Contact angle measurements are used in Chapters 4 and 5 to measure the relative coverage of protein or polymer at the surface of films that are grown or deposited onto a gold substrate. A pure PSI multilayer film has a higher contact angle than a pure PPy film, so measuring the contact angle of a film with both PSI and PPy can give details on the ratio of protein to polymer at the surface of the film according to the Cassie Equation:

$$\cos\theta = f_1 \cos\theta_1 + f_2 \cos\theta_2 \quad [2\text{-}8]$$

$$f_1 = 1 - f_2 \quad [2\text{-}9]$$

where θ is the measured contact angle of the material being investigated, θ_n is the contact angle of pure component n, and f_n is the fractional surface area of component n. If the contact angle is closer to PSI, then the protein has higher fractional surface area and vice versa. Contact angles were measured with a manual Rame-Hart Goniometer.

Profilometry

Contact profilometry is a technique to probe the 2D topography of a material by rastering a cantilever with a diamond tip across a surface. A light source is aimed at the top of the cantilever,

and the change in light deflections as the tip scans the surface is collected to measure the height of a film down to below 100 nm resolution. This technique was used to examine thicknesses of PSI and PSI-PPy films in Chapters 3 and 5. Profilometry was performed using a Veeco DEKTAK 150 contact profilometer.

Ultraviolet-visible spectrophotometry (UV-Vis)

UV-Vis a spectroscopic technique that is used to measure light absorbance of a liquid solution or material on a substrate. The technique works by either transmitting light through a liquid sample or reflecting light off a film on a reflective surface. The source can emit light from UV wavelengths to visible wavelengths. The transmitted or reflected light is then collected at a detector and analyzed to show the wavelengths at which a sample absorbs light. The amount of light absorbed is dependent on the chemical structure of the target sample because different molecules and bonds absorb light at different wavelengths. UV-vis was used in Chapter 4 to monitor the rate of polymerization of PPy in an aqueous solution. UV-vis was performed using a Cary 50 Bio and was operated in Dual Beam mode.

Thermogravimetric Analysis (TGA)

TGA is a characterization method that can investigate thermal properties of a material by exposing the material to high temperatures and measuring the change in mass as components begin to burn off. To measure the change in mass, a sample is loaded into a ceramic crucible that is placed on a hanging scale inside of a tube furnace. After loading the sample, the oven is closed and a purge gas of air or N_2 is flowed through the furnace during the experiment to purge the material as it is being burned off. The choice of gas determines whether the sample combusts (in air) or pyrolyzes (in N_2). The sample is then heated at a specified rate up to a specified temperature. The mass of PSI, PPy, and PSI-PPy conjugates and their thermal stability were measured in

Chapter 4 to compare the thermal properties of the conjugates to the pure materials. In this work, a STA-i 1000 TGA was used, and air was flowed through the furnace. Samples were heated to 100 °C at a rate of 10 °C/min and held for 30 min before a 10 °C/min ramp to 600 °C to remove excess water.

Sodium Dodecyl Sulfate-Polyacrylamide Gel Electrophoresis (SDS-PAGE)

SDS-PAGE is a technique that can measure the molecular weight of the subunits in various biological materials. To perform an SDS-PAGE, a biological material is exposed to a high concentration of the SDS surfactant, which breaks down proteins into their subunits and applies uniform negative charge around all the subunits. The material is then loaded onto the top of a polyacrylamide gel that has multiple lanes to investigate multiple samples. A reference ladder sample can be loaded into one of the wells that will separate into bands of specific molecular weights during the electrophoresis. The gel can be modified by changing the concentration of acrylamide to investigate different weight ranges for the materials under investigation. Once the samples and reference ladder are loaded, a charge is applied across the gel so that a positive charge is generated at the cathode that is opposite of where the samples are loaded. The negative charge of the SDS causes the subunits to migrate through the gel. The speed of migration is dependent on the weight of the material. Lighter subunits will travel faster through the gel, yielding a separation of bands specific to each subunit in the gel. Materials that are insoluble or are too large will not migrate through the gel. The applied charge should be turned off when the lightest subunits are near the bottom of the gel to maximize separation and avoid accumulating material at the bottom of the gel. The gel can then be dyed to see what bands have formed in the gel that can be attributed to different subunits of the target material.

SDS-PAGE was used in Chapter 4 to investigate if conducting polymer was successfully conjugated to PSI by seeing if any of the normal PSI protein bands shift after the polymerization step. SDS-PAGE was performed on samples that were exposed to illumination for 6 h. The samples were then concentrated in a 10K MWCO Pierce Concentrator. After concentration, the samples were prepared as recommended by Invitrogen guidelines using a NuPAGE 10% Bis-Tris Gel.

Powder Conductivity

The conductivity of powders can be measured by compressing the powders between two metal electrodes. The conductivity can be calculated using the following equation:

$$\kappa = \frac{h}{R * A} \qquad [2\text{-}10]$$

where κ = electrical conductivity (S/cm), h = powder height (cm), R = electrical resistance (Ω), and A = cross sectional area of powder (cm^2).[42]

Conductivity was measured in Chapter 4 using a 2-electrode experimental setup (Figure 2.5) connected to a Gamry Reference 600 potentiostat. The setup consists of a transparent glass tube with 2 stainless steel rods that fit snugly within the tube. Powder was placed between the rods and an external force of 300 N was applied to the top electrode to compress the powder. Samples were illuminated on one side of the tube using the same lamp as was used in the electrochemical measurements. The resistance across the powder and the compressed powder height were measured to use in Eq. 2-10 to calculate conductivity. For simplicity of measurement and because of the non-uniformity of particle sizes, the pellets were assumed to have no porosity due to the compressive force, which artificially lowers the measured conductivities.

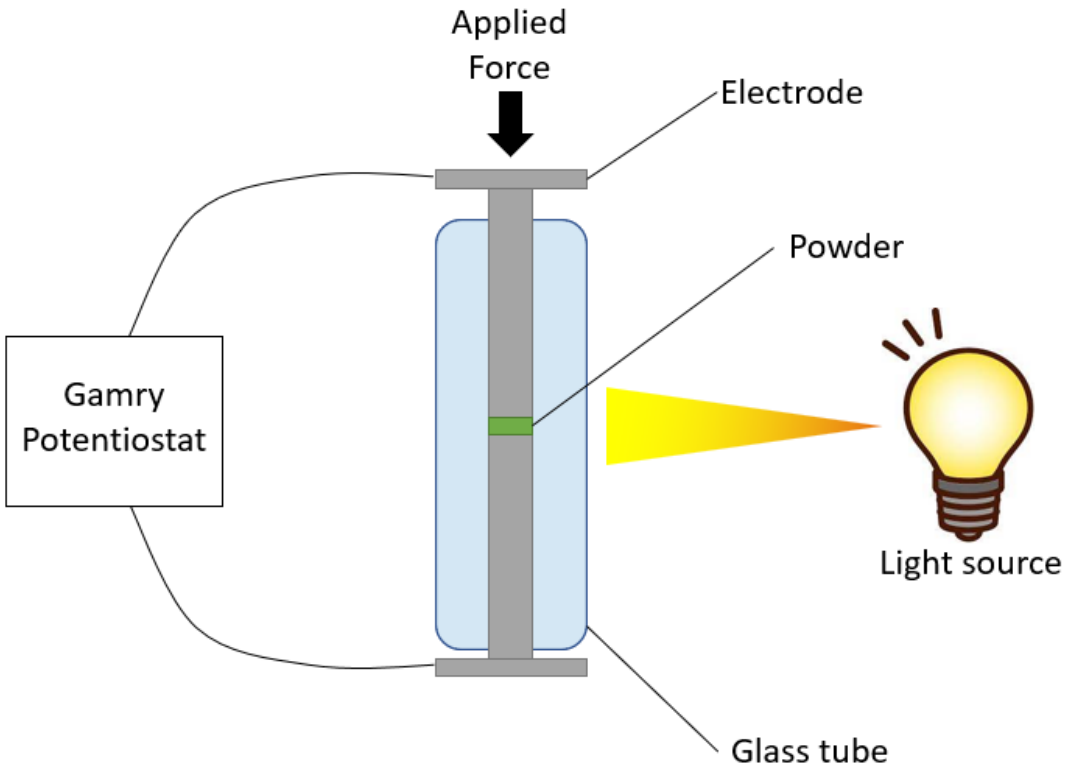

Figure 2.5: Two-piston experimental setup to measure conductivity and photoresponse for powders.

Gel Cell Reaction-Diffusion Model

The electrochemical reaction-diffusion model for the gel cells was generated in Matlab. The model examined the change in concentration of O and R species as well as photocurrent density during 30 s of illumination. The reaction-diffusion system was modelled via MATLAB using the *pdepe* and *lsqcurvefit* functions to solve the system of PDE's and apply the method of least squares, respectively. The MATLAB code is provided in Appendix C. Values after 30 s of illumination were taken as the pseudo-steady state for the device. Devices with and without a PSI film were modeled to investigate the function of PSI at various mediator concentrations.

The assumptions made for this simplified model are that the cathode is limiting the current and therefore is where heterogeneous electrode kinetics are modelled, the initial ratio of O to R is

the same with or without PSI for each initial total concentration, the diffusion coefficients for O and R are the same, the diffusion coefficients for 2,6-dichlorophenolindophenol (DCPIP) and ascorbic acid (AscH) in 0.5% agarose gel are 35% of their diffusion coefficients in liquid water, $0.77x10^{-9}$ and $0.87x10^{-9}$ m^2 s^{-1}, respectively,[7,8] the charge transfer coefficient for the DCPIP mediator is 0.5, the rate-determining step potential for DCPIP is 0.217 V vs. SHE, the exchange current is based on a single-electron transfer taken as the rate-determining step of the two-electron DCPIP reaction, the PSI multilayer acts as redox film and does not partition concentrations, and AscH does not react at the cathode. Values for variables and constants are shown in Table 2.1. Variables were fit using the *lsqcurvefit* command to match the model with experimental data.

Table 2.1: Variables and constants used in reaction-diffusion model.

Parameter	*Value*	*Units*	*Source*
C_{Tot}^*	2-200	mM	Model
C_O^*/ C_R^*	$1.08x10^{-4}$		Fit
C_O^*	$C_O^*/ C_R^* * C_{Tot}^*/20$	mM	Model
C_R^*	$(1- C_O^*/ C_R^*) * C_{Tot}^*/20$	mM	Model
C_{Asc}^*	$C_{Tot}- C_o^*- C_R^*$	mM	Model
D_o & D_R	270	$\mu m^2/s$	[7,8]
D_{Asc}	310	$\mu m^2/s$	[7,8]
n	2	e^-	
α	0.5		
f	0.0257	V	
E_{metal}	0.34	V vs. SHE	[9]
E_{DCPIP}	0.217	V vs. SHE	CV data
k_{PSI}	$2.03x10^{-5}$	s^{-1}	Fit
k_{Asc}	$2.99x10^{-1}$	$mM^{-1} s^{-1}$	[10]
j_0	0.19 with PSI 0.28 without PSI	$\mu A/cm^2$	EIS data

The Bulk Gel

Oxygen and AscH reactions occur homogeneously throughout the device with and without PSI. The equations are:

$$\frac{\partial C_o}{\partial t} = D_o \frac{\partial^2 C_o}{\partial x^2} - k_{Asc} C_o C_{Asc} \quad [2\text{-}11]$$

$$\frac{\partial C_R}{\partial t} = D_R \frac{\partial^2 C_R}{\partial x^2} + k_{Asc} C_o C_{Asc} \quad [2\text{-}12]$$

$$\frac{\partial C_{Asc}}{\partial t} = D_{Asc} \frac{\partial^2 C_{Asc}}{\partial x^2} - k_{Asc} C_o C_{Asc} \quad [2\text{-}13]$$

where $C_i(x,t)$ is the concentration of mediator *O*=oxidized [DCPIP], *R*=reduced [$DCPIPH_2$], and *Asc*=[AscH] at distance *x* and time *t*, D_i is the diffusion coefficient of mediator *i*, and k_{Asc} is the reaction rate of AscH with O. The equations are solved for $x = 0$ to $x = 400$ μm in the absence of a PSI film and for $x = 4$ to $x = 400$ μm with a PSI film, as Eq. [2-14]-[2-16] below account for the reaction when PSI is present.

The PSI Film

While a 4 μm thick film is present, PSI reacts with O and R, but the net reaction produces more O species throughout the film. The equations are:

$$\frac{\partial C_o}{\partial t} = D_o \frac{\partial^2 C_o}{\partial x^2} + k_{PSI} C_R - k_{Asc} C_o C_{Asc} \quad [2\text{-}14]$$

$$\frac{\partial C_R}{\partial t} = D_R \frac{\partial^2 C_R}{\partial x^2} - k_{PSI} C_R + k_{Asc} C_o C_{Asc} \quad [2\text{-}15]$$

[2-16]

$$\frac{\partial C_{Asc}}{\partial t} = D_{Asc}\frac{\partial^2 C_{Asc}}{\partial x^2} - k_{Asc}C_o C_{Asc}$$

where k_{PSI} is the *net* reaction rate of PSI converting O to R. When a PSI film is present, the PSI film is treated as a homogeneous redox active film. The unknown parameter k_{PSI} was fit to match the model with a PSI film present. The value for k_{PSI} was found by using the method of least squares fitting to experimental data with PSI.

Initial and Boundary Conditions

O, R, and AscH are all initially present, and the concentrations are assumed to be the same across the device resulting in the initial condition:

$$C_i(x,0) = C_i^* \qquad [2\text{-}17]$$

where $C_i(x,0)$ is the concentration at t = 0 and C_i^* is the initial concentration of *i*. The initial ratio of O to R was found by using the method of least squares to fit the model to experimental data without PSI.

The fluxes of O and R at the electrodes are related to the current (j_{cell}) flowing through the cell by the following boundary conditions:

$$j_{cell} = nFD_o\frac{dC_o}{dx}|_{x=0};\ -j_{cell} = nFD_o\frac{dC_o}{dx}|_{x=400} \qquad [2\text{-}18]$$

$$-j_{cell} = nFD_R\frac{dC_R}{dx}|_{x=0};\ j_{cell} = nFD_R\frac{dC_R}{dx}|_{x=400} \qquad [2\text{-}19]$$

where *n* is the number of electrons transferred and F is Faraday's constant. For both O and R, the fluxes are opposite to each other at both boundaries to maintain charge balance within the cell.

AscH is assumed to not be redox active at the electrodes leading to the boundary conditions:

$$0 = \frac{dC_{Asc}}{dx}|_{x=0}; \quad 0 = \frac{dC_{Asc}}{dx}|_{x=400} \qquad [2\text{-}20]$$

Heterogeneous Electrode Kinetics

At the cathode and anode, the surface concentrations of the species are related to current through Butler-Volmer electrode kinetics for a rate-determining electron process:[9,11]

$$j_{cell} = j_0 * \left[e^{-\alpha f \eta} - e^{(1-\alpha) f \eta}\right] \qquad [2\text{-}21]$$

$$\eta = \mathrm{E_{copper}} - \mathrm{E_{DCPIP}} + \frac{RT}{nF} \ln \frac{C_o(0,t)}{C_R(0,t)} \qquad [2\text{-}22]$$

where j_o is the exchange current density, α is the charge transfer coefficient, η is the overpotential, $\mathrm{E_{copper}}$ is the potential of the copper electrode, $\mathrm{E_{DCPIP}}$ is the $\mathrm{E_{1/2}}$ for DCPIP, and C_i-(0,*t*) is the surface concentration of *i*.

References

1. Reeves, S. G. & Hall, D. O. Higher Plant Chloroplasts and Grana: General Preparative Procedures (Excluding High Carbon Dioxide Fixation Ability Chloroplasts). *Methods Enzymol.* **69**, 85–94 (1980).

2. Shiozawa, J. A., Alberte, R. S. & Thornber, J. P. The P700-chlorophyll a-protein. *Arch. Biochem. Biophys.* **165**, 388–397 (1974).

3. Baba, K., Itoh, S., Hastings, G. & Hoshina, S. Photoinhibition of photosystem I electron transfer activity in isolated photosystem I preparations with different chlorophyll contents.

Photosynth. Res. **47**, 121–130 (1996).

4. Faulkner, C. J., Lees, S., Ciesielski, P. N., Cliffel, D. E. & Jennings, G. K. Rapid Assembly of Photosystem I Monolayers on Gold Electrodes. *Langmuir* **24**, 8409–8412 (2008).

5. Robinson, M. T., Armbruster, M. E., Gargye, A., Cliffel, D. E. & Jennings, G. K. Photosystem I Multilayer Films for Photovoltage Enhancement in Natural Dye-Sensitized Solar Cells. *ACS Appl. Energy Mater.* **1**, 301–305 (2018).

6. Cottrell, F. G. Application of the Cottrell equation to chronoamperometry. *Z Phys. Chem* (1902).

7. Fradet, E., Abbyad, P., Vos, M. H. & Baroud, C. N. Parallel measurements of reaction kinetics using ultralow-volumes. *Lab Chip* **13**, 4326–4330 (2013).

8. Pénicaud, C., Peyron, S., Bohuon, P., Gontard, N. & Guillard, V. Ascorbic acid in food: Development of a rapid analysis technique and application to diffusivity determination. *Food Res. Int.* **43**, 838–847 (2010).

9. Bard, A. J. & Faulkner, L. R. *Electrochemical Methods: Fundamentals and Applications*. (John Wiley & Sons, Inc., 2001).

10. Tonomura, B., Nakatani, H., Ohnishi, M., Yamaguchi-Ito, J. & Hiromi, K. Test reactions for a stopped-flow apparatus. Reduction of 2,6-dichlorophenolindophenol and potassium ferricyanide by L-ascorbic acid. *Anal. Biochem.* **84**, 370–383 (1978).

11. Newman, J. & Thomas-Alyea, K. E. *Electrochemical systems. Third edition*. *John Wiley & Sons, Inc.* (2004). doi:10.1192/bjp.112.483.211-a

12. Zimmermann, I. *et al.* Improved efficiency and reduced hysteresis in ultra-stable fully

printable mesoscopic perovskite solar cells through incorporation of CuSCN into the perovskite layer. *J. Mater. Chem. A* **7**, 8073–8077 (2019).

Chapter 3

Photosystem I Enhances the Efficiency of a Natural, Gel-Based Dye-Sensitized Solar Cell

Introduction

Photoelectrochemical investigations of PSI have commonly employed the use of a three-electrode liquid cell to enable a focused study of the photoelectrochemical interface between PSI and a single electrode.[1–3] In contrast, fewer researchers have reported the use of PSI in a two-electrode solar cell,[3–10] and most of those include solid-state devices.[4–6,9,10] Solid-state devices with PSI depend on direct electron transfer from electrodes or conducting materials to and from the P_{700} and F_B sites, which complicates device fabrication in comparison to devices dependent on mediated electron transfer (MET). Alternatively, liquid cells rely on MET, which benefits randomly oriented PSI because redox reactions can occur through a protein film and reactants freely diffuse to the electrodes.[11]

The dye-sensitized solar cell (DSSC) is a promising, liquid-based technology that is able to mimic photosynthesis and produce robust solar conversion efficiencies.[12] Traditionally, high performing DSSC's rely on an iodide/triiodide mediator in acetonitrile with a ruthenium-based dye to sensitize the electrode.[3] Issues with the traditional high-performance devices are the toxicity and high volatility of organic solvents as well as the high cost for the ruthenium-based dyes.[12,13] PSI has been explored as a way to boost DSSC performance, and in some cases, as a way to improve renewability and cost-effectiveness. PSI has provided improvement when used as a dye-sensitizer[14,15] and as a redox film on a blackberry dye-sensitized TiO_2 electrode.[16] In these

investigations, PSI was deposited onto TiO_2 to boost anode performance, but using PSI to boost cathode performance while paired with a dye-sensitized anode has not been previously explored.

Liquids are disadvantageous as electrolyte media in photovoltaic systems due to portability issues and continual maintenance resulting from leakage, evaporation, or sealant failure.[17] A quasi-solid-state gel medium negates the limitations prevalent in liquid cells while also providing similar transport capabilities for redox species. A gel analog of a DSSC with an iodide/triiodide mediator exhibited improved photocurrent stability after 125 days of operation versus an equivalent liquid cell.[18] These advantages allow for the minimization of evaporation and enhanced portability while still harnessing mediated electron transfer.

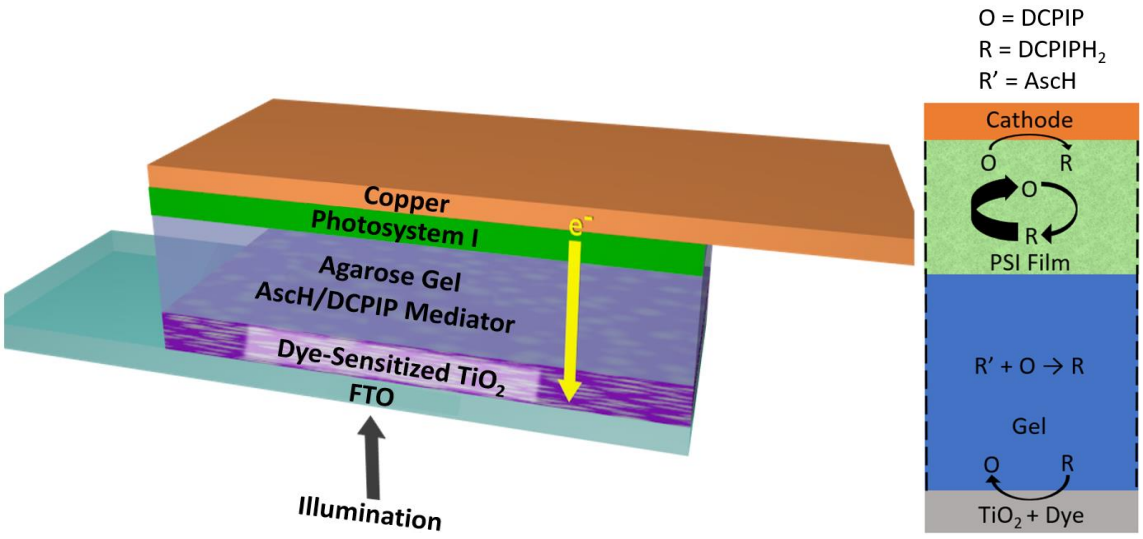

Figure 3.1. Schematic of biohybrid DSSC and suggested redox pathway.

Device Design

The goal for this investigation is to design a low-cost, renewable photovoltaic device that integrates a DSSC electrode with a gel-based medium and a PSI-coated cathode to elevate the performance of the cell, as measured via the short circuit current, open-circuit photovoltage, and power output. Figure 3.1 shows a schematic of the gel-based biohybrid solar cell. The device utilizes an FTO-coated glass slide as a transparent current collector upon which the TiO_2 film is

spin-coated, annealed, and loaded with anthocyanin dye. The gel media is 0.5% wt. agarose hydrogel with supporting electrolyte and an AscH/DCPIP mediator.

Agarose is a naturally derived polysaccharide that is a principal component of agar, a gel commonly used for gel electrophoresis. Agarose has been used in DSSCs and has shown performance enhancement over equivalent liquid cells.[19,20] Agarose can form a polymer matrix in an aqueous solution while maintaining similar ionic conductivity and negating environmental hazards introduced in other types of media.[20] The use of agarose here allows for simple addition of redox mediators to customize the internal environment of the cell. Badura et al. have confined PSI in a thin crosslinked Os-based redox hydrogel film of allylamine and vinylimidazole on a gold electrode in an aqueous three-electrode system purged with O_2 and a methyl viologen (MV) mediator to improve performance of immobilized PSI.[21] The success with the redox hydrogel system proves that PSI can function well in a gel, but the use of an organic chemical for the media, a precious metal electrode, and a toxic mediator suggest challenges in a renewable scale-up.

PSI has been shown to increase photovoltage from 0.22 V to over 0.50 V when deposited atop a TiO_2 anode in a three-electrode cell using a $[Fe(CN)_6]^{4-/3-}$ mediator couple. The improvement was attributed to PSI reducing $Fe(CN)_6^{3-}$ faster than it can oxidize $Fe(CN)_6^{4-}$ to create a higher concentration of the reduced species near the mesoporous anode, which effectively reduces charge recombination.[16] PSI is also known to produce the opposite kinetic asymmetry when exposed to the natural mediator couple AscH/DCPIP by more rapidly producing the oxidized form of DCPIP.[22] This asymmetry implies that the oxidized form of DCPIP would accumulate within the vicinity of the PSI/electrode interface, benefitting cathode performance. The opposite kinetic asymmetry for the $[Fe(CN)_6]^{4-/3-}$ and AscH/DCPIP mediator couples stems from the half-

wave potentials ($E_{1/2}$) being closer to either the reduction potential for the F_B or P_{700} reaction sites, respectively.

For this investigation, three mediator systems—AscH/DCPIP, MV, and $[Fe(CN)_6]^{4-/3-}$—were assessed via photochronoamperometry (PCA) as they are commonly used in PSI-integrated electrochemical investigations because they are good donors or acceptors with the P_{700} and F_B sites, respectively, of PSI.[11,22–26] MV is an oxygen scavenger and can rapidly accept electrons from the F_B site of PSI, creating an excess of reduced species near the cathode, which reduced performance of this device. In the case of $[Fe(CN)_6]^{4-/3-}$, $Fe(CN)_6^{4-}$ is a slow donator to $P_{700,}$ while $Fe(CN)_6^{3-}$ can quickly accept electrons from F_B, leading to an excess of reduced species.[27] In contrast to the reactions of MV and $[Fe(CN)_6]^{4-/3-}$ with PSI, the AscH/DCPIP mediator system is known to rapidly reduce P_{700}, causing an excess of oxidized species in solution.[22] The AscH/DCPIP couple enhances current compared to the other mediators when PSI is deposited onto the cathode (Figure 3.2). Some photocurrent is present in the supporting electrolyte (KCl) control. This photocurrent is attributed to water and oxygen reacting within the system, but this contribution to current is small (<5 $\mu A/cm^2$) in comparison to the overall current with AscH/DCPIP.[28]

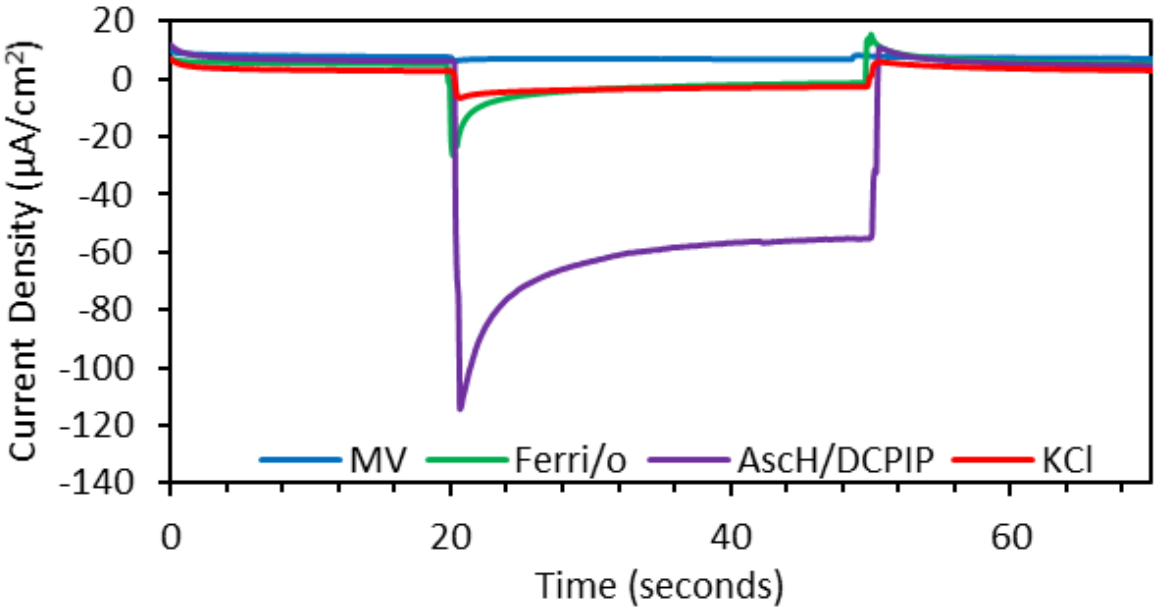

Figure 3.2. Comparison of mediators on a copper electrode containing 4 μm-thick PSI film. Ag/AgCl was used as a reference electrode and Pt as a counter electrode with a 100 mM KCl supporting electrolyte.

AscH, commonly known as vitamin C, is an abundant, non-toxic molecule that protects PSI from harmful reactive oxygen species in vivo[29,30] while DCPIP is a natural, non-toxic redox dye commonly used as a Hill reagent. Together, they are an efficient redox couple when paired with PSI.[31] The reaction between AscH and DCPIP is a catalytic electron transfer/homogenous chemical reaction couple (EC') that catalytically generates $DCPIPH_2$ by the following mechanism at neutral pH:[32]

$$DCPIP + AscH^- \rightleftarrows DCPIPH^\bullet + Asc^{\cdot -}$$

$$DCPIPH^\bullet + AscH^- \rightleftarrows DCPIPH_2 + Asc^{\cdot -}$$

Two ascorbate radicals ($Asc^{\cdot -}$) then react with surrounding protons to regenerate $AscH^-$ and dehydroascorbic acid (DHA) as shown:

$$2Asc^{\cdot -} + H^+ \rightleftarrows AscH^- + DHA$$

At low pH, the prolonged existence of the ascorbate radical becomes unfavorable and the reaction becomes:

$$DCPIP + AscH^- \rightleftarrows DCPIPH^\bullet + Asc^{\cdot -}$$

$$DCPIPH^\bullet + Asc^{\cdot -} + H^+ \rightleftarrows DCPIPH_2 + DHA$$

As shown in the energy diagram (Figure 3.3), PSI is able to generate a redox cycle with the AscH/DCPIP mediator because DCPIP, DHA ,and $Asc^{\bullet -}$ are capable of accepting electrons from F_B and reacting with surrounding protons to regenerate their oxidized forms.[29,33] DCPIP has been shown to be an electron acceptor that can compete with methyl viologen, a rapid and well known F_B electron acceptor, suggesting that its reaction with PSI is faster than the reactions of DHA or $Asc^{\bullet -}$.[33] $DCPIPH_2$ is a rapid electron donor to P_{700} and reacts faster than DCPIP with F_B, which leads to an excess of oxidized species around PSI. Having an excess of AscH serves to increase the concentration of $DCPIPH_2$ species in the cell by continually reducing DCPIP that is not reacted at the cathode. A schematic of the AscH/DCPIP mediator system with PSI is shown in Figure 3.3.[32,33] PSI can increase photocurrent at low mediator concentrations by converting the $DCPIPH_2$ back to DCPIP near the cathode, yielding a higher rate of reduction and increasing the performance of the cell. The reaction kinetics for the AscH/DCPIP reaction mechanism are pH-dependent, prompting a comparison of cell performance at different pH values.[34]

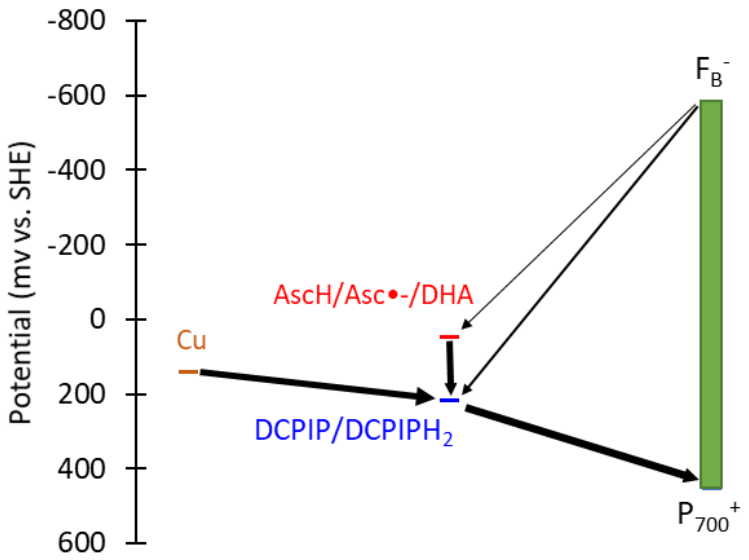

Figure 3.3. Energy diagram showing the redox cycle of the AscH/DCPIP mediator in the presence of PSI on a copper cathode at pH 7. Black lines show the electron flow direction. The potential of the copper electrode was found to be 140 mV vs. SHE by open-circuit potential measurements.

The placement of PSI on either the cathode or the anode was examined, with the observation that depositing a 4 μm thick, randomly oriented PSI film (thickness confirmed by profilometry, Figure 3.4a) on the cathode provided enhancement while placing the film on the anode showed no improvement. PM-IRRAS spectra (Figure 3.4b) were collected to verify the deposition of PSI onto the copper cathode. The IR spectra of a 4 μm thick PSI film show the presence of the characteristic Amide I and Amide II peaks at 1662 and 1545 cm^{-1}, respectively.[35] These results are consistent with the deposition of structurally intact PSI films on the copper cathode.

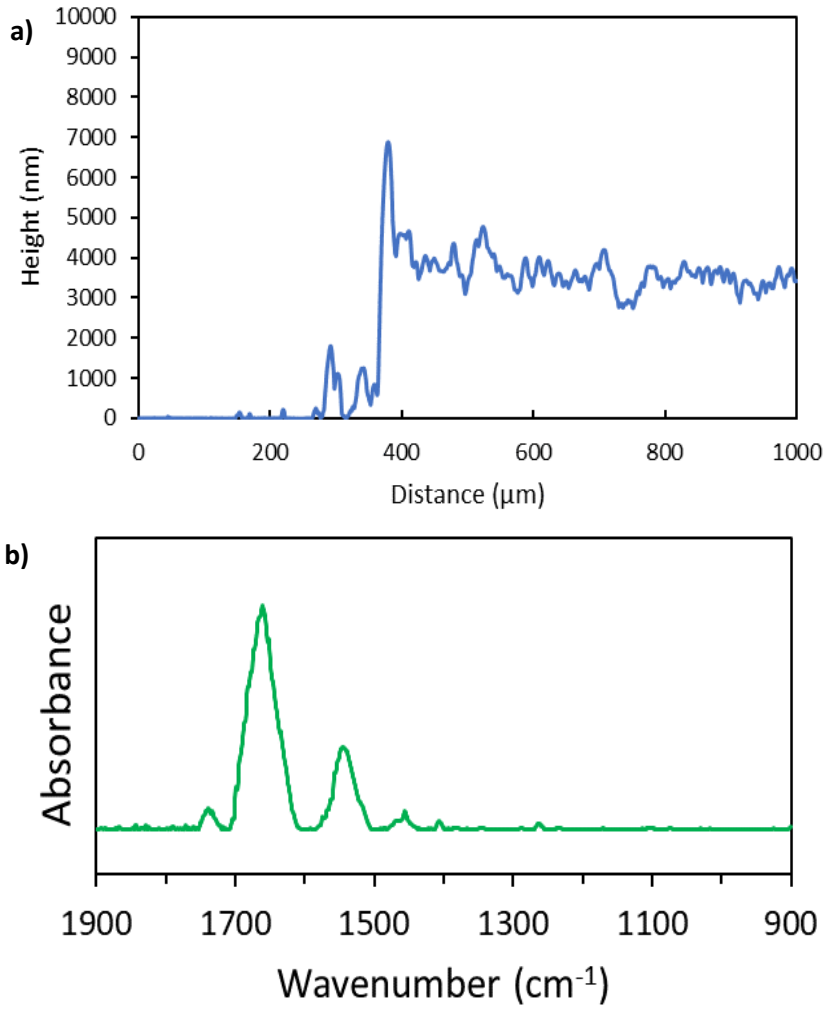

Figure 3.4. a) Profilometric thickness of a characteristic vacuum-assisted, drop-cast PSI multilayer film. b) PM-IRRAS FTIR spectra of a PSI multilayer film deposited on copper.

Copper was chosen as a suitable, inexpensive cathode because it has inherent energetic synergy with PSI and a substantial potential difference with the conduction band of TiO_2 (0.34 and -0.30 V vs SHE, respectively).[36] In nature, the oxidizing end of PSI, the P_{700} site, accepts electrons from the copper-containing protein plastocyanin. TiO_2 was selected as the semiconductor anode because it has a favorable energy band alignment with PSI and copper,[14] it absorbs UV light well, and it can be deposited as mesoporous films that can be sensitized with dyes to enhance light absorbance in the visible spectrum.[16] Anthocyanin (AC), a naturally occurring dye derived from blackberries, is used to sensitize the TiO_2 here because it absorbs light in the 500-650 nm

wavelength range, complementing the absorbance of both TiO_2 and PSI. PSI absorbs strongly in 400-500 nm and 650-700 nm wavelengths of visible light while TiO_2 absorbs strongly at <400 nm.[16] The TiO_2 and AC anode on FTO allows light at wavelengths complementary to PSI to pass through. The extracted dye consists of approximately 90 wt% cyanidin-3-glucoside and 10 wt% cyanidin-3-glucosyl-malonate.[16]

As dye-sensitized TiO_2 is known to be a good photoanode,[14,16,18,37,38] we focus here on improving copper cathode performance. We hypothesize that by using the naturally occurring mediator couple AscH/DCPIP, we can harness the asymmetry of PSI's redox capabilities and increase photocurrent with a PSI multilayer film deposited on the cathode of a photovoltaic device. Combining these materials yields a PSI-derived natural DSSC, and we investigate the effect of PSI film thickness, pH, and mediator concentration on the performance of the cell.

Results and Discussion

Device Performance

The effect of PSI on cell photovoltage and photocurrent over a range of mediator concentrations was examined. Additionally, devices were tested at two different pH ranges: low (2.5-3.5) and neutral (6.5-7.5). The pH-dependent mole fraction of the oxidized forms of DCPIP as described by the Henderson-Hasselbach equation with pKa's of 0.5 and 5.6 are shown in Figure 3.5, denoted as DH_2^+, DH, and D^-.[34] At the lower pH range, DH is the dominant oxidized form while at neutral pH, D^- is the dominant form, and these forms behave differently in electrochemical cells, with D- providing greater current during cyclic voltammetry (Figure 3.6). A similar trend in activity vs. pH was also observed by Petrova et al.[33] Additionally, D^- reacts with ascorbic acid at a kinetic rate that is two orders of magnitude slower than that for DH with ascorbic acid.[34] The

overall reduction of the oxidized forms of DCPIP to $DCPIPH_2$ occurs at all pH values, but the rate of reduction is pH dependent.[34]

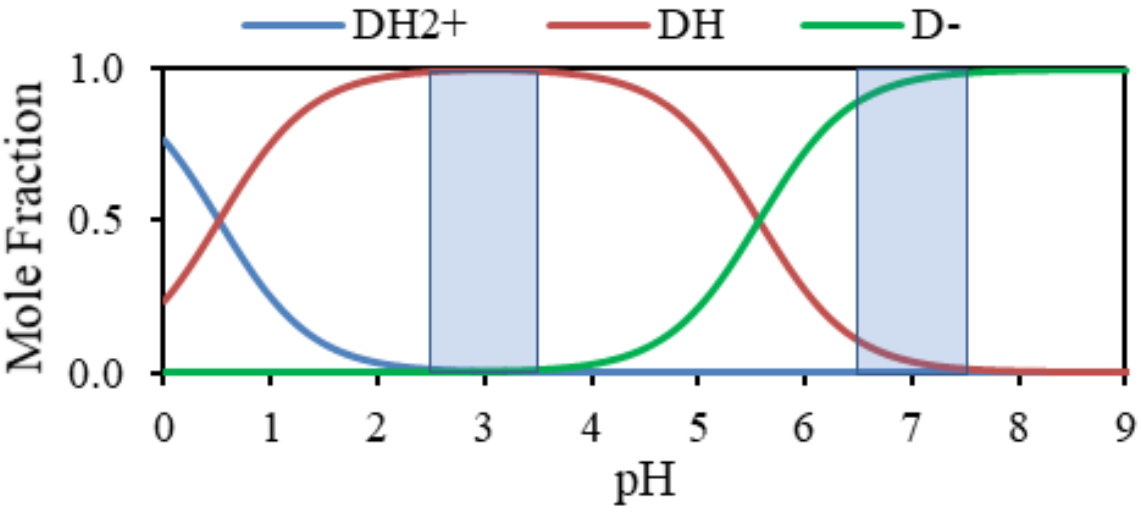

Figure 3.5. Mole fraction for pH-dependent forms of DCPIP. Shaded sections represent values in which devices were tested.

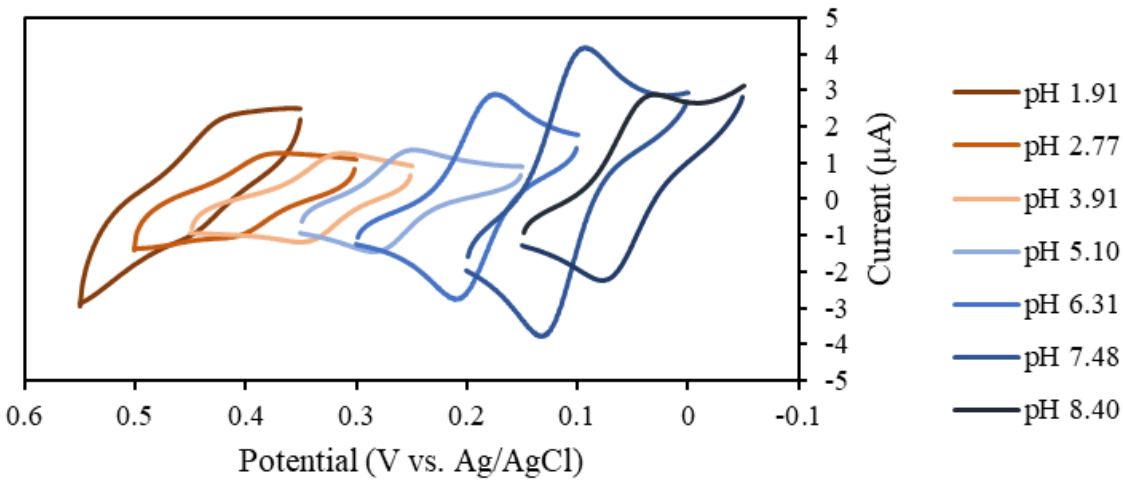

Figure 3.6. CV pH dependence on peak currents for 1 mM DCPIP in 100 mM phosphate buffer. Au working electrode, Pt counter electrode, and Ag/AgCl reference.

An advantage of a two-electrode device is that it enables the measurement of the photovoltage produced across the cell instead of examining the potential of only the working electrode that constrains three-electrode experiments. Figure 3.7a shows the photovoltage generated by the devices at all concentrations and each pH range. For a Nernstian equilibrium

process, the potential of an electrode is dependent on the ratio of the concentration of oxidized to reduced species and is therefore independent of bulk concentration as shown in the Nernst Equation:

$$E(t) = E_0 + \frac{RT}{nF} \ln \frac{C_O(0,t)}{C_R(0,t)} \quad [3\text{-}1]$$

Devices without PSI produce photovoltages of 0.35 V and 0.37 V at low pH and neutral pH, respectively, while the addition of a PSI film onto the copper cathode increases the photovoltage at each pH range. The photovoltages produced without PSI are attributed to the dye-sensitized TiO_2 semiconductor anode absorbing light and reacting with mediators. We expect that the faster reaction between PSI's $P700^+$ and $DCPIPH_2$ versus that between F_B^- and DCPIP generate higher concentrations of oxidized species near the cathode, increasing the ratio of oxidized to reduced species and, therefore, making the Nernstian potential at the cathode more positive. Consistent with that reasoning, the photopotential increases in the presence of PSI, raising the total photovoltage of the cell by 0.050 to 0.41 V, a 7-fold increase in the ratio of oxidized to reduced species for the devices measured at lower pH, and by 0.075 to 0.45 V, an 18.5-fold increase in the ratio for the devices measured at neutral pH. These large increases in the ratio of species are possible because of the ultralow concentration of oxidized species in the AscH/DCPIP system prior to light exposure and the localization of PSI on the cathode. The greater increase in photovoltage for the devices at neutral pH is attributed to DCPIP having a slower reaction with AscH at low pH, so the oxidized species generated by PSI are not consumed as rapidly, increasing the ratio of oxidized to reduced species at the cathode.[32,34]

Devices at low pH were linked in series to increase the total photovoltage (Figure 3.7b). The PSI-integrated devices exhibit a linear increase in photovoltage up to 2.1 V for five devices in

series as compared to 1.5 V for the devices without PSI. The photovoltage enhancement with PSI becomes important in scaling-up device fabrication because fewer materials would be needed.

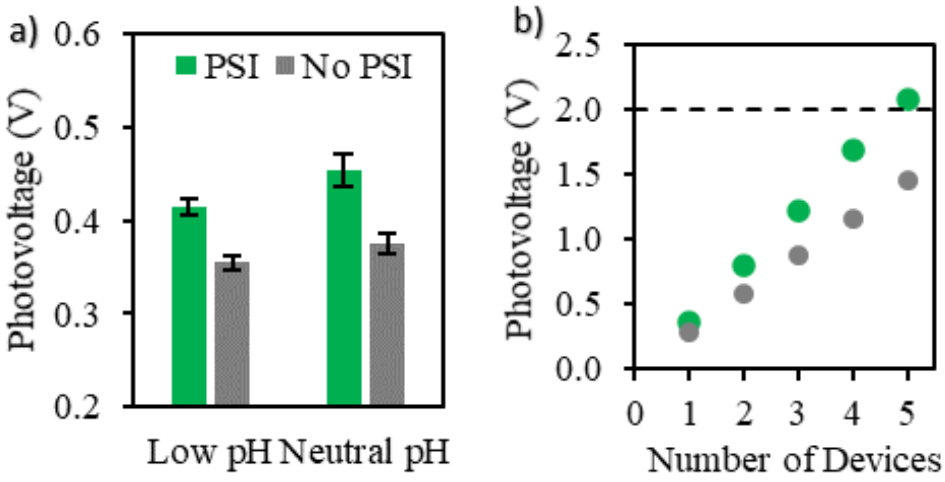

Figure 3.7. a) Single-device photovoltage enhancement with PSI at low pH (2.5-3.5) and neutral pH (6.5-7.5). b) Enhancement of photovoltage after connecting multiple devices at low pH in series.

PCA was used to determine how the PSI film affects the photocurrent generation at various AscH/DCPIP mediator concentrations. Figure 3.8 shows representative PCA curves for devices at low and neutral pH at a concentration of 20 mM AscH:1 mM DCPIP. The current densities for all devices follow a Cottrell-like decay under illumination, consistent with diffusional limitations for the gel devices that are similar to those observed in two- and three-electrode liquid-based PSI systems.[21,27] At both low and neutral pH, the peak photocurrent density and the pseudo-steady state photocurrent density (after 30 s of illumination) are higher in the presence of PSI at this mediator concentration. The diffusional decay is stronger at lower pH, which is likely due to the faster consumption of oxidized DCPIP species by AscH.[39] The devices at neutral pH outperformed those at low pH, suggesting that the D^- form performs better in this system than DH, likely because DH reacts faster with AscH and slower with the P_{700} site and the copper. The CV results from Figure 3.6 support this hypothesis because of the change in electrochemical activity.

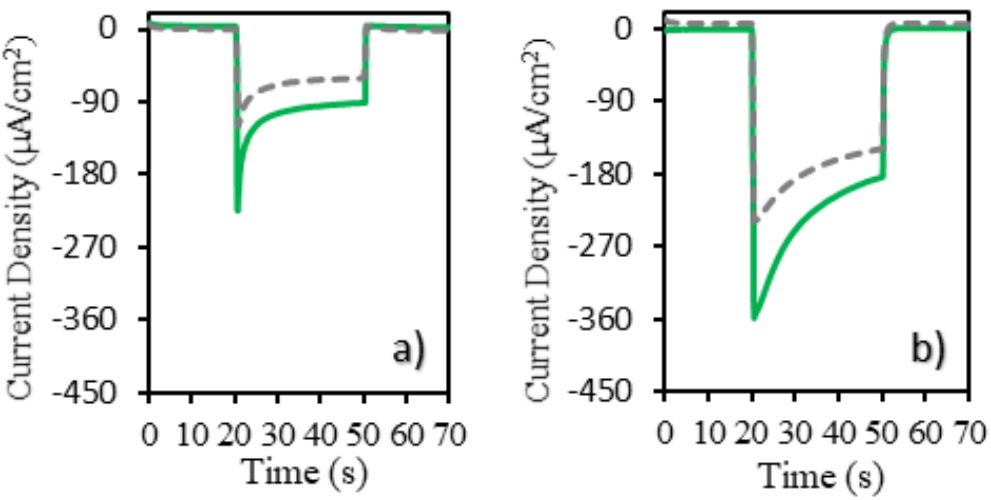

Figure 3.8. Photocurrent response for devices at low (a) and neutral (b) pH with (solid green line) and without (dashed gray line) a PSI film on the copper cathode in agarose gel with 100 mM KCl and 20 mM AscH:1 mM DCPIP. Devices were illuminated from 20-50 s.

Figure 3.9 shows the trend between pseudo-steady photocurrent and mediator concentration for all devices. Without PSI, the pseudo-steady photocurrent density increases as concentration increases. For all concentrations, the devices near neutral pH outperform those at low pH. The pH-induced change in performance is also observed in the devices with a PSI film on the cathode. At neutral pH, the presence of a PSI film contributes a 18-49% enhancement to photocurrent at intermediate concentrations but yields statistically similar photocurrents at high concentrations. Devices at low pH ranging from 2-20 mM AscH all showed improvements with PSI over the non-PSI devices, while at 60 mM, the performance was similar, but at higher concentrations, the photocurrent density was well below that of the non-PSI devices. In all cases, photovoltage was still enhanced by 50-75 mV.

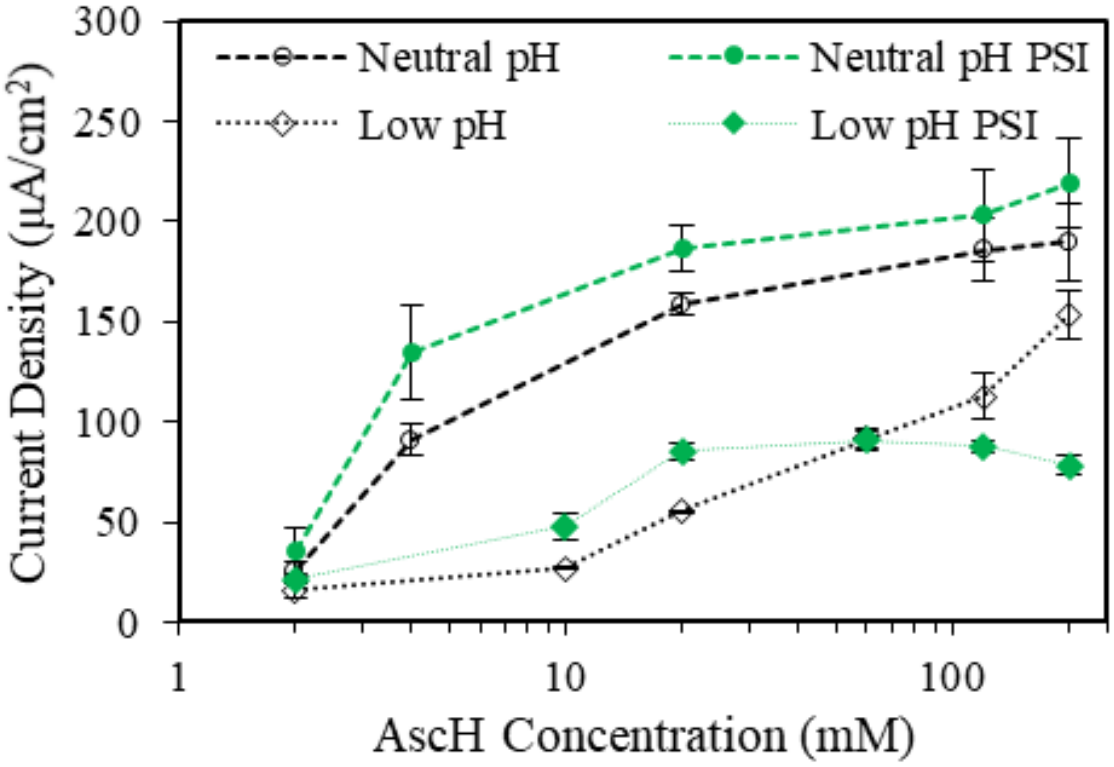

Figure 3.9. Steady-state photocurrent density of devices at low and neutral pH with and without a PSI multilayer. Values were measured after 30 s of illumination for each device. For each data point, the initial ratio of AscH to DCPIP concentrations is 20:1.

As the mediator concentration increases, the finite number of PSI reaction sites effectively becomes the limiting reagent in the production of O, and thus, the photocurrent in the presence of PSI begins to plateau. Saturation of PSI sites via Michaelis-Menten processes at high mediator concentration have also been attributed to such plateaus.[27,39] At low pH values, the devices with PSI plateau near 90 µA/cm^2 at a concentration of 20 mM AscH and above while the neutral pH devices appear to begin plateauing above 20 mM AscH at a value ~200 µA/cm^2. The difference in the plateaus with pH is attributed to the slower reaction of D^- with AscH that yields higher concentration of oxidized species near the cathode, in addition to the increased electrochemical activity of D^-.

The devices at neutral pH outperformed those at low pH, so power curves of devices at neutral pH were produced to measure the power output with and without PSI (Figure 3.10a). The power curves were obtained by taking the average of j-V curves done at forward and reverse scan directions to find the voltage where maximum power occurs. The reverse scan in which potential is decreased to approach maximum current provides much improved performance as compared to the forward scan and represents an instantaneous power output. The lesser performance of the forward scan is likely due to a depletion of charge carriers by starting the scan at the highest current. Hysteresis in dye-sensitized solar cells is common because of charge carrier trapping in the bulk TiO_2. Additionally, the diffusional nature of the cell likely also adds to the hysteresis.

Then, a steady-state power value was determined by measuring power output under illumination while devices were biased at the maximum power voltages until steady-state was reached to yield accurate power performance (Figure 3.10b).[40,41] Devices at 20 mM AscH:1 mM DCPIP with and without PSI showed a maximum power output of 0.033 and 0.023 mW/cm^2 and power conversion efficiencies of 0.042% and 0.028%, respectively. Table 3.1 shows the characteristic parameters for the j-V curves obtained from forward and reverse scans as well as the average values. Instantaneous power outputs were also measured by measuring a reverse scan j-V curve at 10 V/s. The instantaneous maximum power output and efficiencies with and without PSI were 0.24 and 0.14 mW/cm^2 and 0.30% and 0.18%, respectively (Figure 3.11).

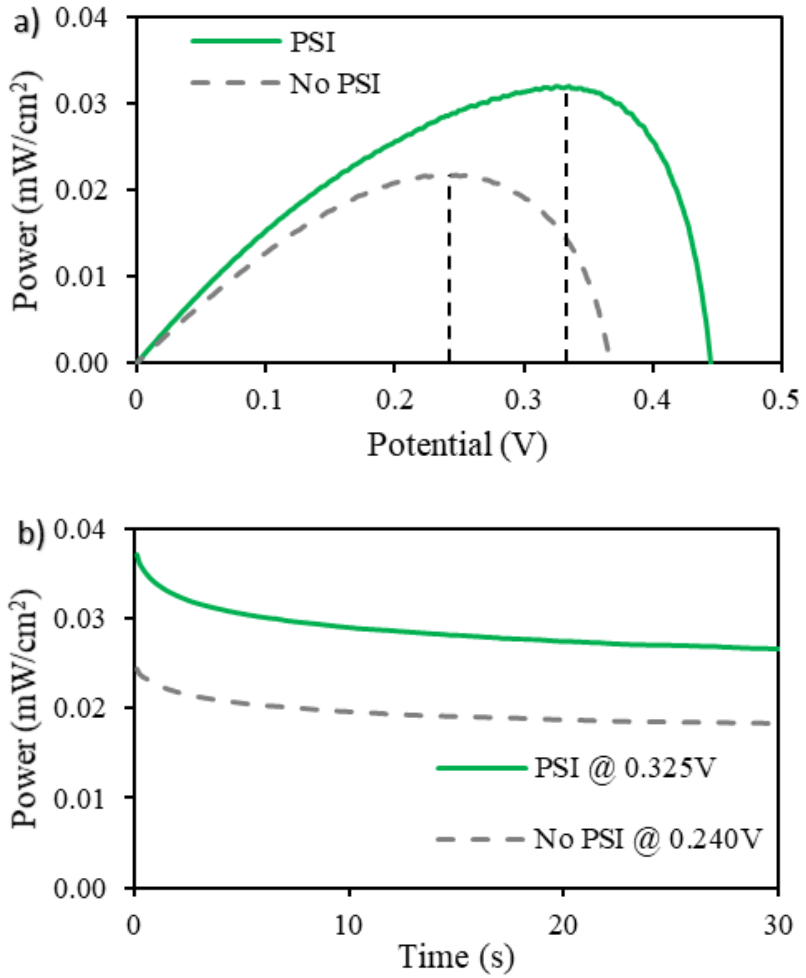

Figure 3.10. a) Power curves of devices at neutral pH and a concentration of 20 mM AscH to 1 mM DCPIP. The resulting power curve represents an average of forward and reverse j-V scans at 1 V/s. 80 mW/cm^2 of light intensity was used, and scans were run after 30 s of illumination. b) Steady-state power generation of devices biased at the voltage where maximum power occurs.

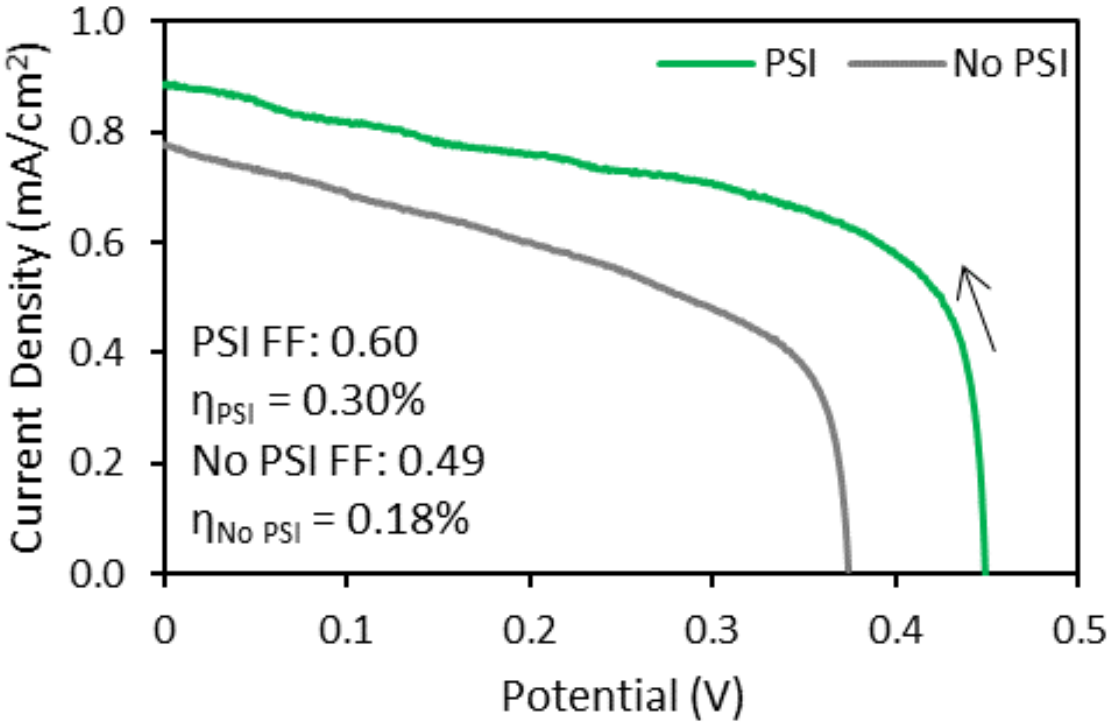

Figure 3.11. Reverse scan j-V curves for devices at neutral pH, with and without PSI, and a mediator concentration of 20 mM AscH to 1 mM DCPIP. Scan rate was 10 V/s. Samples were illuminated for 30 s at 80 mW/cm^2 before scans were taken while still under illumination.

Table 3.1: Power parameters fill factor (FF) short-circuit current density (Jsc), open circuit potential (OCP), and power conversion efficiency (η) at steady-state.

	FF	J_{SC} *(μA/cm^2)*	*OCP (V)*	*η (%)*
PSI_{Rev}	0.60	190.4	0.450	0.064
PSI_{For}	0.26	159.4	0.436	0.023
PSI_{Avg}	0.43	174.9	0.443	0.042
No PSI_{Rev}	0.47	170.9	0.375	0.037
No PSI_{For}	0.37	118.6	0.350	0.019
No PSI_{Avg}	0.42	144.8	0.363	0.028

To confirm that the decreased performance of the devices at low pH was due to pH and not the supporting electrolyte, replicate devices at low pH were fabricated using sodium nitrate as the supporting electrolyte, and the performance was the same as those in KCl. Additionally, devices at neutral pH with a KCl supporting electrolyte were tested and performed similarly to those with

phosphate electrolyte. Phosphate is the preferred supporting electrolyte because it is stable, acts as a buffer around neutral pH values, and is not corrosive toward the copper cathode.

The presence of the relatively thick, 4 μm PSI film raised concern that a barrier effect might cause changes in performance. To confirm that the redox capabilities of PSI were causing the enhancements, devices with varying film thicknesses were fabricated by diluting the initial PSI suspension (Figure 3.12). Additionally, devices at low pH with a 4 μm film of deactivated PSI (thermally deactivated by boiling for 2 min) were also made to test the barrier properties of the PSI film. PSI multilayer films increased device performance with an increase in the thickness of the protein film by multiple deposition steps up to 2.5 μm because of the availability of more active sites in the protein film for conversion of mediator.[42] Here, the performance continues to increase with thickness, but beyond a thickness of 2 μm, the rate of increase slows, likely caused by the film becoming thick enough that light is unable to penetrate completely through it as seen in previous models of light absorbance through a PSI multilayer film.[27] Additionally, the device with the deactivated 4 μm thick protein film yields the same photocurrent density and photovoltage as the devices without PSI, indicating that the performance enhancements provided by PSI are not dictated by barrier or partitioning effects. This conclusion is also confirmed by EIS because the presence of a PSI film does not significantly affect ion transfer to the electrode (Figure 3.13). Collectively, these results support the conclusion that the observed enhancements in photocurrent and photovoltage are driven by PSI-mediator reactions.

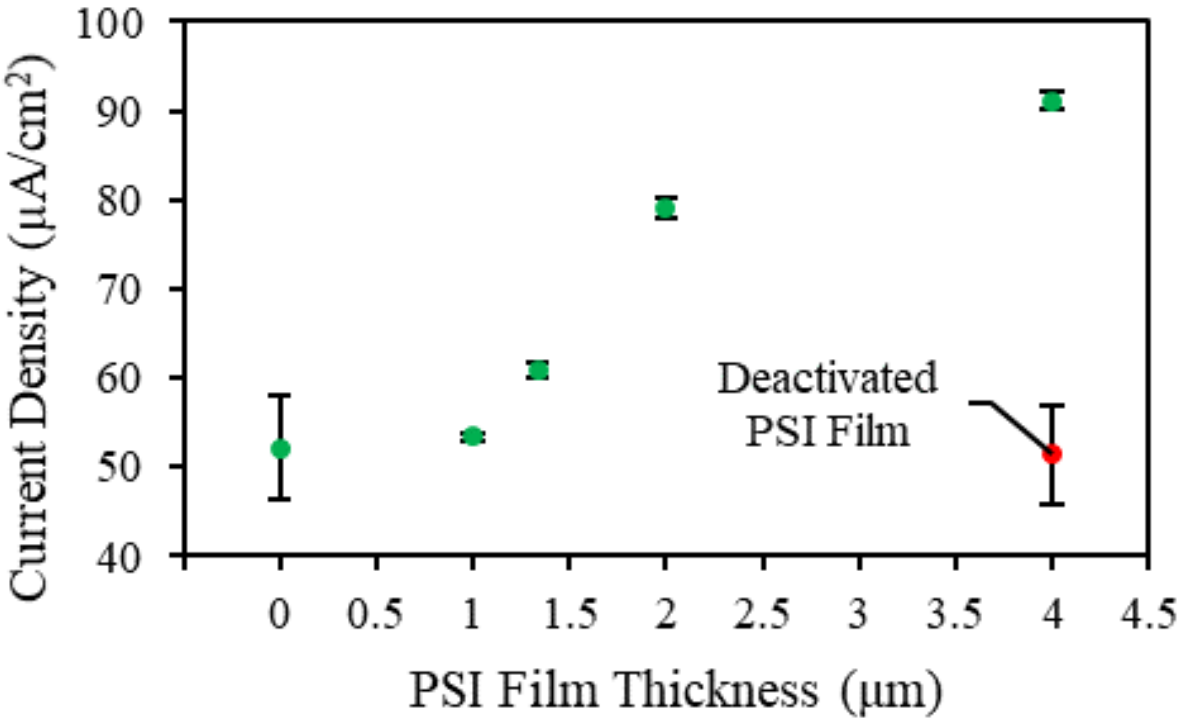

Figure 3.12. Effect of PSI film thickness on device performance for 20 mM AscH : 1 mM DCPIP at low pH. The deactivated data was collected by thermally denaturing PSI by boiling for 10 min before deposition. The photovoltage of the cell with the deactivated film of PSI is 0.35 V, which is the same as that of the cell without PSI (0.35 V).

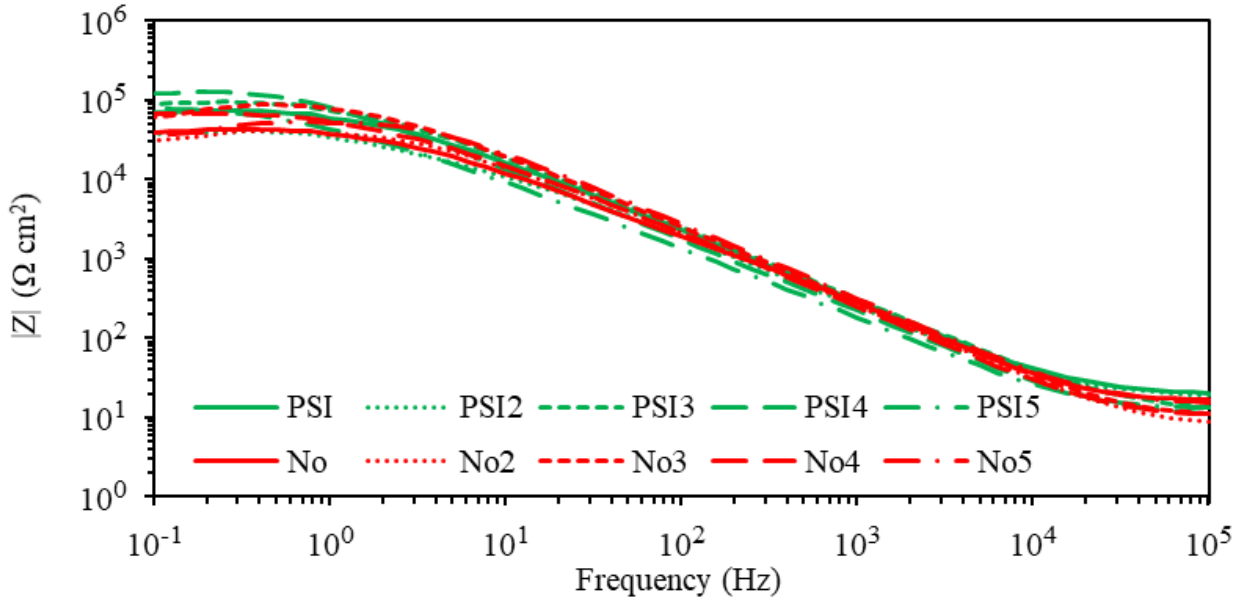

Figure 3.13. Electrochemical impedance spectra of copper electrodes with and without PSI films in 0.5 wt% agarose gel. The electrolyte solution for each sample consists of 20 mM AscH, 1 mM DCPIP, and 100 mM KCl.

PSI Model

We developed a simplified electrochemical reaction-diffusion model in Matlab that is discussed in further detail in Chapter 2. The model examined the change in concentration of oxidized and reduced species as well as photocurrent density during 30 s of illumination. Values after 30 s of illumination were taken as the pseudo-steady state for the device. Devices with and without a 4 μm-thick PSI film were modeled to investigate the function of PSI in the system at various mediator concentrations. Values for the variables and constants used or measured are shown in Table 3.2.

Table 3.2: Variables and constants used in reaction-diffusion model.

PARAMETER	VALUE	UNITS	SOURCE
C_{Tot}^*	2-200	mM	Model
C_O^*/ C_R^*	$1.08x10^{-4}$		Fit
C_O^*	$C_O^*/ C_R^**C_{Tot}^*/20$	mM	Model
C_R^*	$(1- C_O^*/ C_R^*)*C_{Tot}^*/20$	mM	Model
C_{Asc}^*	$C_{Tot}- C_o^*- C_R^*$	mM	Model
D_O & D_R	270	$\mu m^2/s$	[44,45]
D_{ASC}	310	$\mu m^2/s$	[44,45]
n	2	e^-	
α	0.5		
F	0.0257	V	
E_{METAL}	0.34	V vs. SHE	[36]
E_{DCPIP}	0.217	V vs. SHE	CV
k_{PSI}	$2.03x10^{-5}$	s^{-1}	Fit
K_{ASC}	$2.99x10^{-1}$	$mM^{-1} s^{-1}$	[34]
J_0	0.19 with PSI 0.28 without PSI	$\mu A/cm^2$	EIS

The model was used to estimate photocurrent density after 30 s of illumination in devices at neutral pH with and without PSI. The resulting photocurrent densities were then normalized to

the photocurrent density computed for a device without PSI at the same mediator concentration of 200 mM AscH to 10 mM DCPIP to compare the model to the experimental system (Figure 3.14).

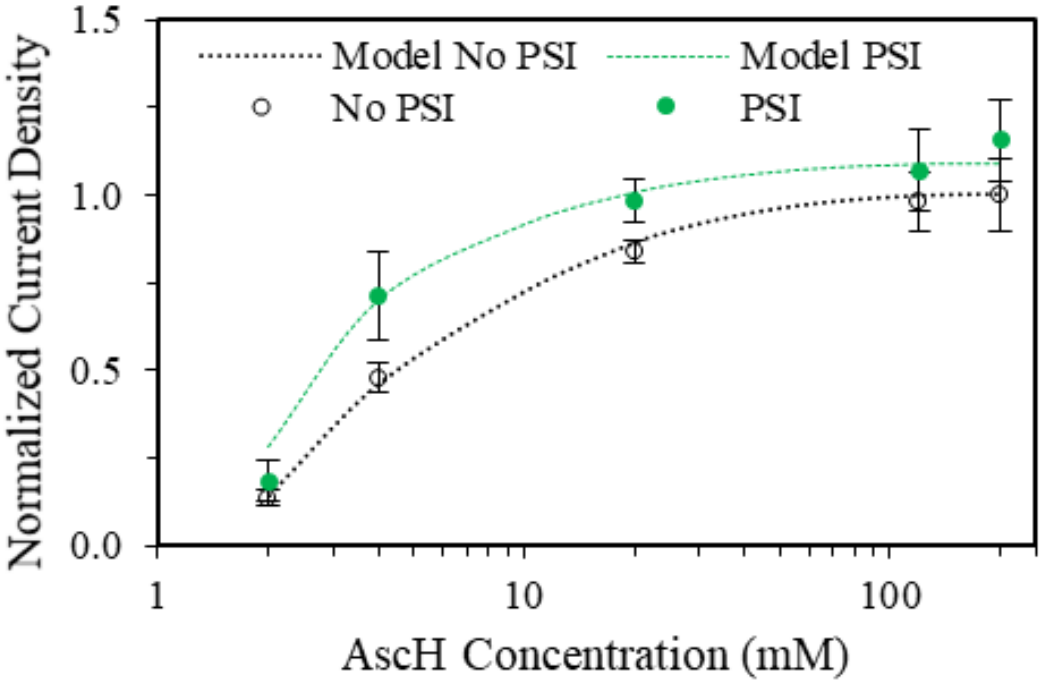

Figure 3.14. Comparison of model predictions (lines) for photocurrent density to experimental data (points) with PSI (filled points) and without PSI (open points) in devices at neutral pH. Values were normalized to the photocurrent density value of a device without PSI at a mediator concentration of 200 mM AscH to 10 mM DCPIP.

Two of the parameters were unknown while formulating the model: the initial ratio of O to R concentrations (C_O^*/ C_R^*) and the reaction rate constant for PSI (k_{PSI}). To find these parameters, the *lsqcurvefit* function was used to first match the model to experimental data without PSI to obtain the initial C_O^*/ C_R^* ratio. A value of 1.07×10^{-4} represents an initial conversion of ~99.99%, which is expected as the reaction of AscH with DCPIP is generally considered to approach completion.[34,43] A 99.99% conversion results in an ultralow initial concentration of O, allowing for PSI to provide a large (e.g. 18.5-fold) increase in the surface concentration ratios as seen by the photovoltage enhancements.

The value for the net rate of conversion of R to O by PSI (k_{PSI}) was determined by using *lsqcurvefit* to match the model to the experimental data with PSI, using the initial ratio of C_O^*/ C_R^* obtained by modeling the experimental data without PSI. The first-order rate constant was fit to be 1.98×10^{-5} s^{-1}, showing that a positive net reaction rate for the production of O does result in improved photocurrent performance compared to non-PSI devices. Additionally, the model shows that if the net kinetic rate of conversion by PSI remains constant, a plateauing effect on photocurrent occurs as concentration increases, confirming that the reaction sites provided by PSI do indeed become a limiting reagent.

Conclusions

A low-cost, renewable, gel-based biophotovoltaic device was designed and easily fabricated in this study. The device uses abundant, environmentally friendly, and inexpensive materials, including PSI, copper, TiO_2, blackberry anthocyanin dye, AscH, DCPIP, and agarose. The use of an agarose hydrogel enables redox reactions to occur as in a liquid device while allowing simpler construction of a two-electrode device. Within the tested concentration range, photovoltage was independent of bulk mediator concentration, but devices at neutral pH outperformed those at lower pH because of the pH-dependent nature of the AscH/DCPIP couple. A 4 μm thick PSI film increased photovoltage at low and neutral pH values by 50 and 75 mV, respectively, compared to devices without PSI to achieve values of up to 450 mV. Devices connected in series showed a linear increase in photovoltage with each device.

Photocurrent was dependent on mediator concentration, pH, and the presence of PSI. At both low and neutral pH, PSI enhanced photocurrent at low to moderate mediator concentrations as compared to devices without PSI, but enhancement diminished as mediator concentration increased because of the limiting reaction capabilities of the PSI films. j-V power curves obtained

at neutral pH with a 20 mM AscH to 1 mM DCPIP concentration showed that PSI devices had a power conversion efficiency of 0.042% compared to 0.028% without PSI. Additionally, a numerical model was developed to examine the effect of PSI-mediator oxidation kinetics on photocurrent. The model is consistent with experiments, showing that the asymmetric kinetic production of O species by PSI leads to photocurrent enhancements that are more dramatic at low and intermediate concentrations of mediator.

This investigation is the first to incorporate PSI in a two-electrode gel-based cell, showing that the asymmetric redox kinetics of the protein provides enhancement to both photocurrent and photovoltage when deposited on the cathode of a DSSC. The reported devices are environmentally friendly and made from easily sourced materials with low energy input compared to many other photovoltaic technologies.

References

1. Nguyen, K. & Bruce, B. D. Growing green electricity: Progress and strategies for use of Photosystem I for sustainable photovoltaic energy conversion. *Biochim. Biophys. Acta - Bioenerg.* **1837**, 1553–1566 (2014).
2. LeBlanc, G., Gizzie, E. A., Yang, S., Cliffel, D. E. & Jennings, G. K. Photosystem I Protein Films at Electrode Surfaces for Solar Energy Conversion. *Langmuir* **30**, 10990–11001 (2014).
3. Musazade, E. *et al.* Biohybrid solar cells: Fundamentals, progress, and challenges. *J. Photochem. Photobiol. C Photochem. Rev.* **35**, 134–156 (2018).
4. Das, R. *et al.* Integration of photosynthetic protein molecular complexes in solid-state electronic devices. *Nano Lett.* **4**, 1079–1083 (2004).
5. Gordiichuk, P. I. *et al.* Solid-state biophotovoltaic cells containing photosystem i. *Adv.*

Mater. **26**, 4863–4869 (2014).

6. Gizzie, E. A. *et al.* Photosystem I-polyaniline/TiO_2 solid-state solar cells: simple devices for biohybrid solar energy conversion. *Energy Environ. Sci.* **8**, 3572–3576 (2015).

7. Olmos, J. D. J. *et al.* Biofunctionalisation of p-doped silicon with cytochrome c_{553} minimises charge recombination and enhances photovoltaic performance of the all-solid-state photosystem I-based biophotoelectrode. *RSC Adv.* **7**, 47854–47866 (2017).

8. Zeynali, A., Ghiasi, T. S., Riazi, G. & Ajeian, R. Organic solar cell based on photosystem I pigment-protein complex, fabrication and optimization. *Org. Electron. physics, Mater. Appl.* **51**, 341–348 (2017).

9. Kazemzadeh, S., Riazi, G. & Ajeian, R. Novel Approach of Biophotovoltaic Solid State Solar Cells Based on a Multilayer of PS1 Complexes as an Active Layer. *ACS Sustain. Chem. Eng.* **5**, 9836–9840 (2017).

10. Dervishogullari, D., Gizzie, E. A., Jennings, G. K. & Cliffel, D. E. Polyviologen as Electron Transport Material in Photosystem I-Based Biophotovoltaic Cells. *Langmuir* **34**, 15658–15664 (2018).

11. Wolfe, K. D. *et al.* Photosystem I Multilayers within Porous Indium Tin Oxide Cathodes Enhance Mediated Electron Transfer. *ChemElectroChem* 1–9 (2019).

12. Ye, M. *et al.* Recent advances in dye-sensitized solar cells: From photoanodes, sensitizers and electrolytes to counter electrodes. *Mater. Today* **18**, 155–162 (2015).

13. Xiang, W., Huang, F., Cheng, Y. B., Bach, U. & Spiccia, L. Aqueous dye-sensitized solar cell electrolytes based on the cobalt(ii)/(iii) tris(bipyridine) redox couple. *Energy Environ. Sci.* **6**, 121–127 (2013).

14. Yu, D. *et al.* Enhanced photocurrent production by bio-dyes of photosynthetic

macromolecules on designed TiO_2 film. *Sci. Rep.* **5**, (2015).

15. Mershin, A. *et al.* Self-assembled photosystem-I biophotovoltaics on nanostructured TiO_2 and ZnO. *Sci. Rep.* **2**, 234 (2012).

16. Robinson, M. T., Armbruster, M. E., Gargye, A., Cliffel, D. E. & Jennings, G. K. Photosystem I Multilayer Films for Photovoltage Enhancement in Natural Dye-Sensitized Solar Cells. *ACS Appl. Energy Mater.* **1**, 301–305 (2018).

17. Grätzel, M. Dye-sensitized solar cells. *J. Photochem. Photobiol. C Photochem. Rev.* **4**, 145–153 (2003).

18. Tsai, C. H. *et al.* Efficient gel-state dye-sensitized solar cells adopting polymer gel electrolyte based on poly(methyl methacrylate). *Org. Electron. physics, Mater. Appl.* **14**, 3131–3137 (2013).

19. Bidikoudi, M., Perganti, D., Karagianni, C.-S. & Falaras, P. Solidification of ionic liquid redox electrolytes using agarose biopolymer for highly performing dye-sensitized solar cells. *Electrochim. Acta* **179**, 228–236 (2015).

20. Wang, W., Guo, X. & Yang, Y. Lithium iodide effect on the electrochemical behavior of agarose based polymer electrolyte for dye-sensitized solar cell. *Electrochim. Acta* **56**, 7347–7351 (2011).

21. Badura, A. *et al.* Photocurrent generation by photosystem 1 integrated in crosslinked redox hydrogels. *Energy Environ. Sci.* **4**, 2435–2440 (2011).

22. Bennett, T. H. *et al.* Jolly green MOF: confinement and photoactivation of photosystem I in a metal-organic framework. *Nanoscale Adv.* **1**, (2019).

23. Chen, G., LeBlanc, G., Jennings, G. K. & Cliffel, D. E. Effect of Redox Mediator on the Photo-Induced Current of a Photosystem I Modified Electrode. *J. Electrochem. Soc.* **160**,

H315–H320 (2013).

24. Kavan, L., Tétreault, N., Moehl, T. & Grätzel, M. Electrochemical characterization of TiO_2 blocking layers for dye-sensitized solar cells. *J. Phys. Chem. C* **118**, 16408–16418 (2014).

25. Manocchi, A. K. *et al.* Photocurrent Generation from Surface Assembled Photosystem I on Alkanethiol Modified Electrodes. *Langmuir* **29**, 2412–2419 (2013).

26. Baker, D. R., Simmerman, R. F., Sumner, J. J., Bruce, B. D. & Lundgren, C. A. Photoelectrochemistry of photosystem I bound in Nafion. *Langmuir* **30**, 13650–13655 (2014).

27. Robinson, M. T., Cliffel, D. E. & Jennings, G. K. An Electrochemical Reaction-Diffusion Model of the Photocatalytic Effect of Photosystem I Multilayer Films. *J. Phys. Chem. B* **122**, 117–125 (2018).

28. Gust, D. *et al.* Photoassisted Overall Water Splitting in a Visible Light-Absorbing Dye-Sensitized Photoelectrochemical Cell. *J. Am. Chem. Soc.* **131**, 926–927 (2009).

29. Trubitsin, B. V., Mamedov, M. D., Semenov, A. Y. & Tikhonov, A. N. Interaction of ascorbate with photosystem i. *Photosynth. Res.* **122**, 215–231 (2014).

30. Takagi, D., Takumi, S., Hashiguchi, M., Sejima, T. & Miyake, C. Superoxide and Singlet Oxygen Produced within the Thylakoid Membranes Both Cause Photosystem I Photoinhibition. *Plant Physiol.* **171**, 1626–1634 (2016).

31. Vernon, L. P. & Zaugg, W. S. Photoreductions by fresh and aged chloropasts: requirement for ascorbate and 2, 6-dichlorophenolindophenol with aged chloroplasts. *J. Biol. Chem.* **235**, 2728–2733 (1960).

32. Marchanka, A. & Van Gastel, M. Reversed freeze quench method near the solvent phase transition. *J. Phys. Chem. A* **116**, 3899–3906 (2012).

33. Petrova, A., Mamedov, M., Ivanov, B., Semenov, A. & Kozuleva, M. Effect of artificial redox mediators on the photoinduced oxygen reduction by photosystem I complexes. *Photosynth. Res.* **137**, 421–429 (2018).

34. Tonomura, B., Nakatani, H., Ohnishi, M., Yamaguchi-Ito, J. & Hiromi, K. Test reactions for a stopped-flow apparatus. Reduction of 2,6-dichlorophenolindophenol and potassium ferricyanide by L-ascorbic acid. *Anal. Biochem.* **84**, 370–383 (1978).

35. Robinson, M. T., Simons, C. E., Cliffel, D. E. & Jennings, G. K. Photocatalytic photosystem I/PEDOT composite films prepared by vapor-phase polymerization. *Nanoscale* 6158–6166 (2017). doi:10.1039/C7NR01158J

36. Bard, A. J. & Faulkner, L. R. *Electrochemical Methods: Fundamentals and Applications*. (John Wiley & Sons, Inc., 2001).

37. Kumara, N. T. R. N., Lim, A., Lim, C. M., Petra, M. I. & Ekanayake, P. Recent progress and utilization of natural pigments in dye sensitized solar cells: A review. *Renew. Sustain. Energy Rev.* **78**, 301–317 (2017).

38. Ferber, J., Stangl, R. & Luther, J. Electrical model of the dye-sensitized solar cell. *Sol. Energy Mater. Sol. Cells* **53**, 29–54 (1998).

39. Buesen, D., Hoefer, T., Zhang, H. & Plumere, N. A Kinetic Model for Redox-Active Film Based Biophotoelectrodes. *Faraday Discuss.* (2019). doi:10.1039/c8fd00168e

40. Wagner, L., Chacko, S., Mathiazhagan, G., Mastroianni, S. & Hinsch, A. High photovoltage of 1 V on a steady-state certified hole transport layer-free perovskite solar cell by a molten-salt approach. *ACS Energy Lett.* **3**, 1122–1127 (2018).

41. Jeon, N. J. *et al.* Compositional engineering of perovskite materials for high-performance solar cells. *Nature* **517**, 476–480 (2015).

42. Ciesielski, P. N. *et al.* Enhanced Photocurrent Production by Photosystem I Multilayer Assemblies. *Adv. Funct. Mater.* **20**, 4048–4054 (2010).

43. Karayannis, M. I. Comparative kinetic study for rate constant determination of the reaction of ascorbic acid with 2,6-dichlorophenolindophenol. *Talanta* **23**, 27–30 (1976).

44. Fradet, E., Abbyad, P., Vos, M. H. & Baroud, C. N. Parallel measurements of reaction kinetics using ultralow-volumes. *Lab Chip* **13**, 4326–4330 (2013).

45. Pénicaud, C., Peyron, S., Bohuon, P., Gontard, N. & Guillard, V. Ascorbic acid in food: Development of a rapid analysis technique and application to diffusivity determination. *Food Res. Int.* **43**, 838–847 (2010).

46. Newman, J. & Thomas-Alyea, K. E. *Electrochemical systems. Third edition*. *John Wiley & Sons, Inc.* (2004).

Chapter 4

Oxidative Polymerization from Photosystem I Proteins

Introduction

Protein-polymer conjugates are a unique class of biohybrid materials that offer the combination of properties of both synthetic polymers and biomolecules. These conjugates have been used to advance research in a wide range of fields such as medicine,[1] enzymatic performance,[2] muscle-inspired actuators,[3] and catalysis.[4]

Herein, we present a novel route for protein-polymer conjugates in which we use a photoactive redox protein to polymerize an electroactive monomer. Specifically, we demonstrate a photopolymerization technique where unmodified Photosystem I (PSI) protein complexes can directly polymerize pyrrole monomer (Py) to form PSI-polymer conjugates.

PSI has been interfaced with conducting polymers in multiple applications. A common constraint for PSI-polymer systems is the dependence on mediated electron transfer to small redox species because of a lack of direct connection to the active sites for direct electron transfer.[5–7] To ensure connection, protein-polymer conjugates have been formed by other groups using a modified protein complex with a molecular wire connected to a catalyst or enzyme at the F_B site for hydrogen production.[8,9]

The oxidative capability of the P_{700} is energetically favorable to perform oxidative polymerizations,[10] such as with Py, as described in this chapter. This process is able to achieve direct connections between the conducting polymer, polypyrrole (PPy), and the P_{700} site to yield a PSI-PPy conjugate capable of photoelectrochemistry. This polymerization technique is one of the first known cases of a photoactive protein-polymer conjugate where the polymer was formed by an unmodified protein. This technique could be expanded by using other monomers to tailor

conjugate functionality or other photoactive proteins. The ability to create protein-polymer conjugates to combine the photo-redox properties of PSI with special properties of the polymer should facilitate the generation of inexpensive, biohybrid solar conversion technology.

Results and Discussion

Visual Properties

The initial evidence of successful polymerization of Py by PSI proteins was visual. The addition of Py monomer with $NaClO_4$ as an anionic dopant to a dispersion of PSI followed by subsequent illumination of solar light leads to the formation of dark green (characteristic color of PPy)[11] aggregates that eventually precipitate to the bottom of the solution (Figure 4.1a). The aggregates become increasingly darker with additional light exposure, and a darker green solid approaches black in color after 30 h of solar illumination. As controls, when exposed to simulated sunlight, Py (alone) does not visibly change, and a PSI protein solution becomes bleached by the UV radiation in the solar simulated light. The polymerization also occurs in white light.

To confirm this was a light-dependent reaction, the same experiment was carried out by illuminating monomer and PSI-monomer solutions for 6 h while another set of monomer and PSI-monomer solutions was left in the dark (Figure 4.1b). The illuminated PSI-monomer solution yielded the darker green aggregates while the solutions in the dark remained the same color as in the initial conditions.

$NaClO_4$ was selected as dopant for the polymer because of the large anionic size, compared to other simple anions, and its lack of reactivity with Py, compared to other dopants that act as a chemical oxidizer. For these oxidizing dopants that can chemically polymerize Py, the addition of PSI accelerates the production of polymer.

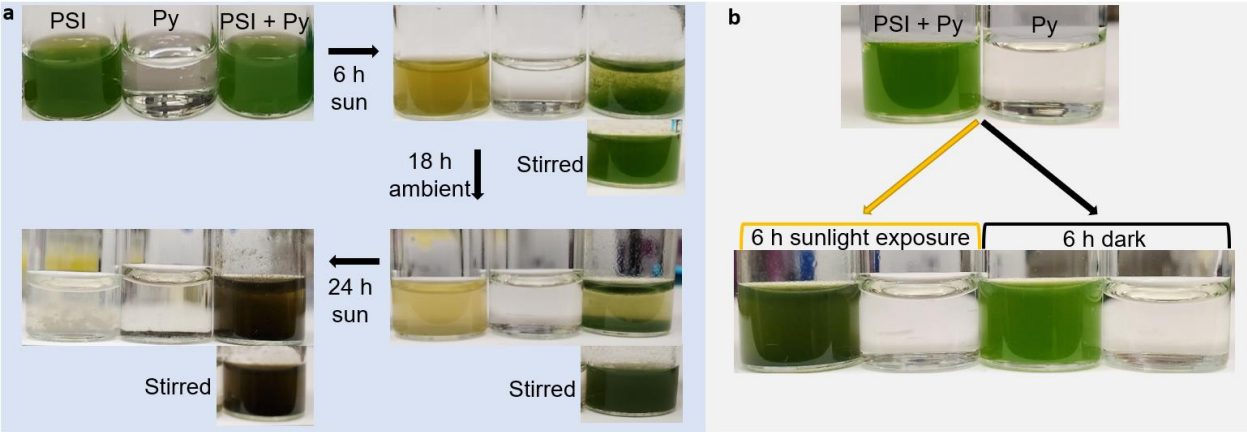

Figure 4.1: a) Changes in visual solution properties over time after illumination. From left to right: PSI, Py monomer, PSI + Py monomer. b) Comparison of visible solution changes after 6 h of illumination or no light.

Polymerization by mixing PSI and Py with a dopant that results in oxidative polymerization was also examined. The chemical polymerization of PPy by polystyrene sulfonate (PSS) occurs on a timescale of hours as compared to the much faster timescale for other chemical oxidants such as ferricyanide and ferric chloride. The slower reaction allows for examination of the effects of the addition of PSI and illumination to the mixture. PSS is commonly used as a dopant for the polymer poly-3,4-ethylenedioxythiophene (PEDOT) because of its ability to result in a water-soluble, conducting polymer, which allows for easier processibility. The inherent insolubility of conducting polymers is an issue when trying to homogeneously process the polymers. Polymerization of Py with PSI containing Triton X-100, which is a surfactant used during the protein extraction for solubilization, was also compared to the polymerization of Py with dialyzed protein. Figure 4.2 shows the visible changes in 3 systems of Py and PSS suspensions exposure to ambient light for 24 h.

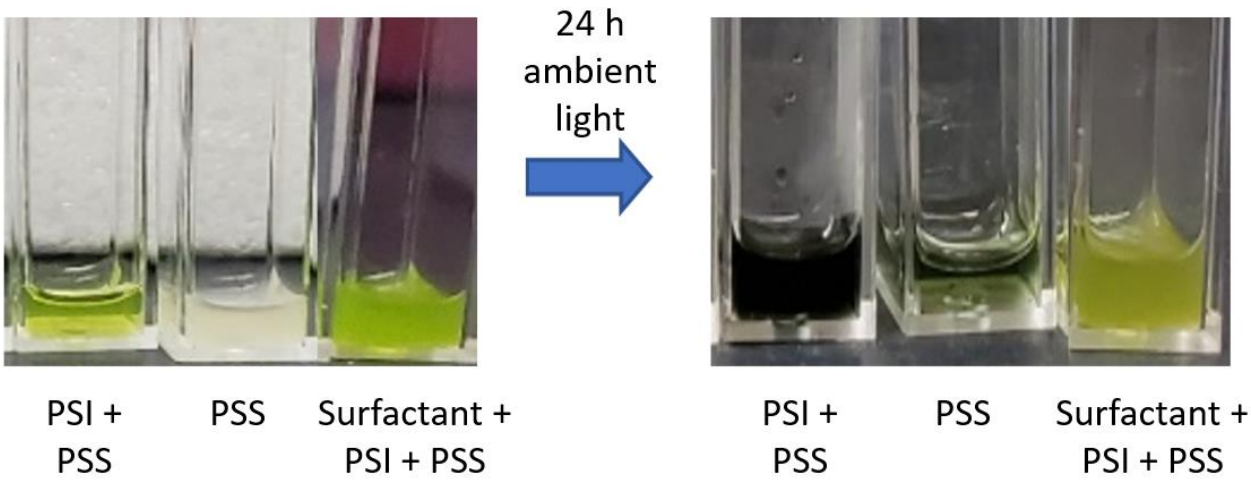

Figure 4.2: Samples with Py monomer and PSI, PSS, and/or Triton X-100 surfactant before and after 24 h of ambient light.

After 24 h, the samples without Triton X-100 surfactant both show a significant change in color from either a light green or opaque white to deep green, suggesting successful PPy polymerization. Comparatively, the sample with surfactant and PSI slightly changes color, but the color change is minimal compared to the samples without surfactant. The likely reason is that in the presence of surfactant, PSI proteins are surrounded by a surfactant shell that is blocking access of the P_{700} reaction sites to monomer in solution, severely limiting the reaction rate with the protein. The surfactant shell is needed to remove PSI from an ion-exchange chromatography column during the protein extraction and allows the protein to remain suspended in solution.

The extent of the polymerization was further examined through UV-Vis spectroscopy. Visible spectra taken from 0 to 190 min of illumination are shown in Figure 4.3. The darkening of the solution is indicative of the continued polymerization, leading to higher absorbance in the spectra. PSI has a strong absorbance peak at 680 nm due to the chlorophylls in the protein. A PPy spectrum has a broad peak from 650-1000 nm. Growth in this region is not seen in the samples that had either only Py or PSI or the sample with PSI and PSS with no monomer, confirming that the peak is a result of the Py polymerization.

The growth of a broad peak ranging from 650 to 1000 nm is indicative of the growth of PPy. The peak exists when Py monomer is exposed to PSS alone, but the Visible spectra show that PSI can catalyze the polymerization because the absorbance is increased over time more than 2-fold when PSI is present in the solution.

For the systems with PSS and surfactant, the reaction products were more water-soluble than reaction products of dialyzed PSI and monomer, which settle out of solution over time. However, the surfactant is undesirable because it slows the reaction. To further explore the effect of PSI in this reaction, $NaClO_4$ was selected as the desired dopant for further study because it does not react with the monomer.

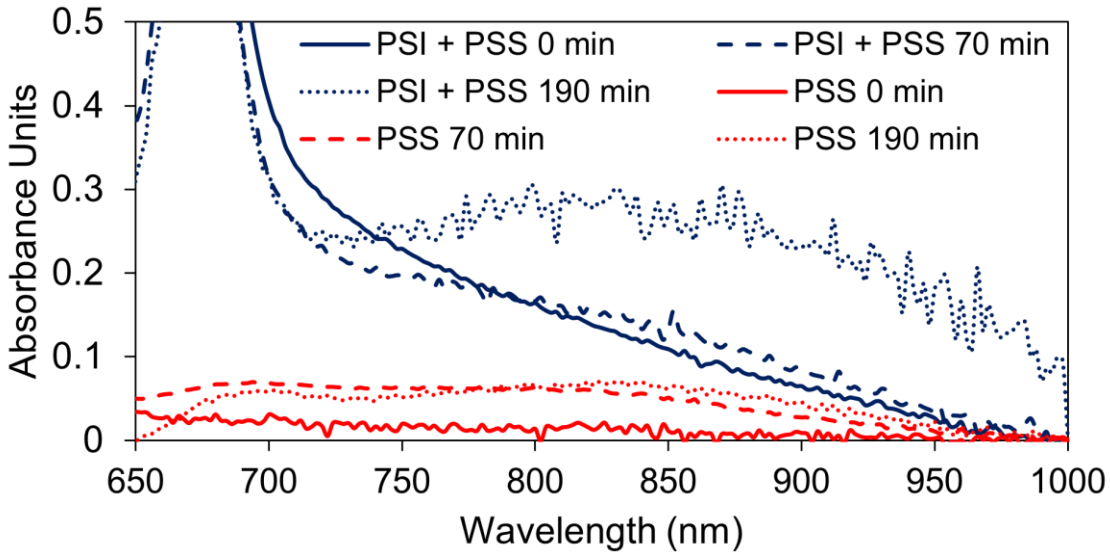

Figure 4.3: Visible spectra comparing reaction with and without PSI that include PSS and Triton X-100 surfactant.

ATR-FTIR analysis was used to identify the composition of the products formed upon illumination of PSI with Py monomer (Figure 4.4). After illumination in white light, the solution was dialyzed to remove excess Py, drop-cast onto a gold surface, rinsed with water, and then analyzed by FTIR. Figure 4.4a shows the characteristic spectra for a film of pure electropolymerized PPy with significant peaks at 1594 (N-H bending), 1462 (C=C aromatic

stretching), 1250 (C-N stretching), 1159 (C-N stretching), 1074 (C-N stretching), and 942 (C-H sp^2 bending) cm^{-1} that are broader and distinct from those peaks of the Py monomer. Figure 4.4b shows the spectra of pure PSI with peaks at 1627 (Amide I), 1529 (Amide II), 1448 (C-H bending), 1391 (C-H bending), and 1239 (C-N stretching) cm^{-1}. Figure 4.4c shows the spectra for the reaction product obtained by mixing PSI with monomer and illuminating for 3 h. Most notably, the spectra for the reaction product shows similar peaks for both PPy (peaks below 1300) and PSI (Amide I and II peaks). Additionally, the valley between the Amide I and II peaks is higher than the pure spectra, suggesting growth of an aromatic N-H peak as in the PPy spectra.

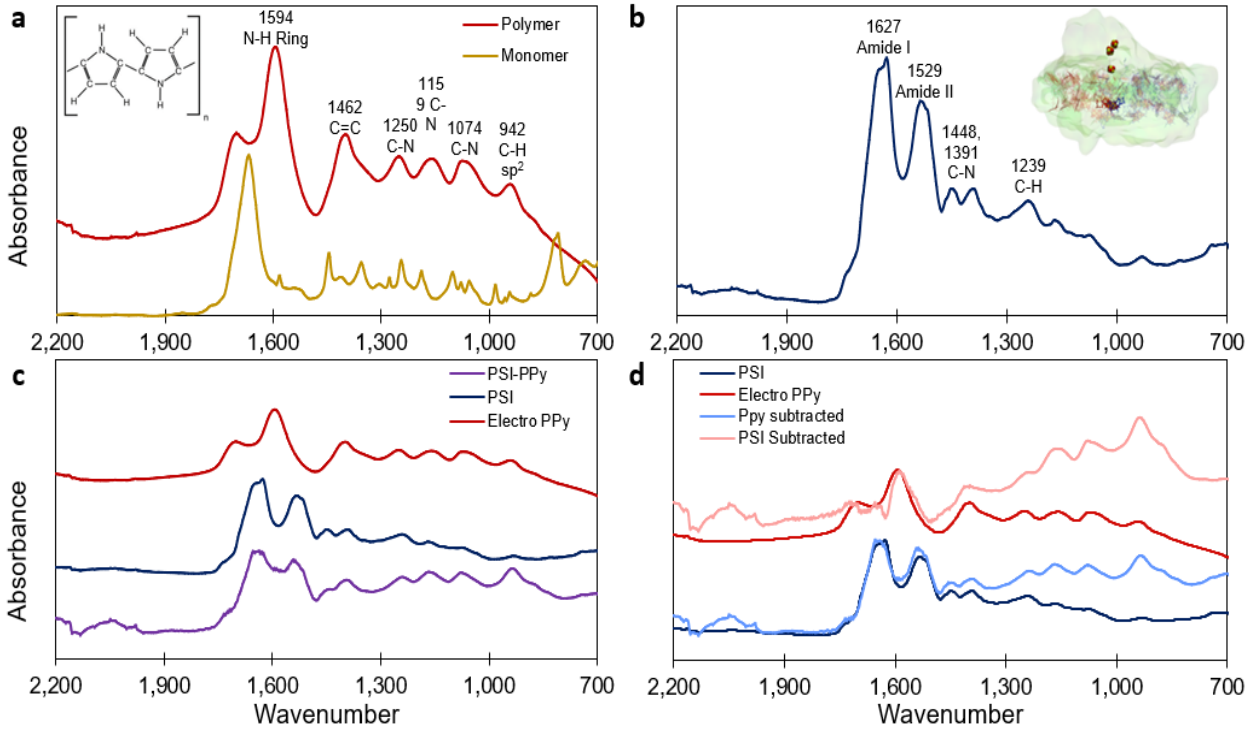

Figure 4.4: a) FTIR spectra of Py and electropolymerized PPy film along with characteristic peaks, b) PSI spectra and characteristic peaks, c) Comparison of PPy grown by PSI to pure PPy and PSI spectra, d) Result of spectral subtraction of pure components from reaction product compared to pure component.

To compare the reaction product spectra to the two pure components, each spectrum of the pure components was subtracted from the spectrum of the reaction product (Figure 4.4d). After

subtraction of the pure components, the characteristic peaks for both PSI and PPy can be seen in the resultant spectra. The PPy characteristic peaks at 1594, 1462, 1250, 1159, 1074, and 942 cm^{-1} are all prominent in the PSI-subtracted spectrum, and there is no evidence of the monomer peaks at 1663 (C=C stretching) cm^{-1} and 808 (C-H bending) after spectral subtraction, indicating the successful synthesis of PPy that is compositionally consistent with an electropolymerized PPy film. The characteristic peaks for PSI appear at 1627, 1529, 1448, 1391, and 1239 cm^{-1} and are all prominent in the PPy-subtracted spectra with no peak shifting or change in peak shape, suggesting that PSI is still present in the product without degradation.[12]

Contact angles of films of pure PSI, pure PPy, and the PSI-PPy reaction product were measured on gold substrates to examine surface property changes. The solutions were dialyzed to remove excess monomer before being drop-cast, and the films were rinsed in distilled water to remove any excess buffer and monomer, leaving only protein and polymer. The contact angles show a significant decrease from 44 ± 3° for the PSI films to 26 ± 7° for the PSI-PPy films while pure PPy films exhibit a lower contact angle of 21 ± 7°. The decrease in contact angle for the PSI-PPy films is consistent with a surface that contains both PSI and PPy, supporting the successful polymerization of Py by PSI.

SEM morphologies of powders of traditionally grown PPy and the PSI-monomer reaction product are shown in Figure 4.5. The chemically synthesized PPy from the addition of ferrocyanide as an oxidant shows a commonly reported morphology of PPy nanoparticles that are coalesced to make a large, networked structure.[13–15] PPy electropolymerized on a gold-coated surface shows similar morphology with connected spherical nanoparticles. The PSI-PPy powder shows a different morphology of solid platelet-like structures instead of a connected nanoparticle network. The formation of PPy platelets has been reported and is most commonly the result of

polymerization that is kinetically slower than the more rapid oxidation with ferrocyanide or that by an applied potential on an electrode.[16–18] Additionally, other experiments have shown that longer polymerization times lead to larger nanoparticles with lower definition between each particle.[19]

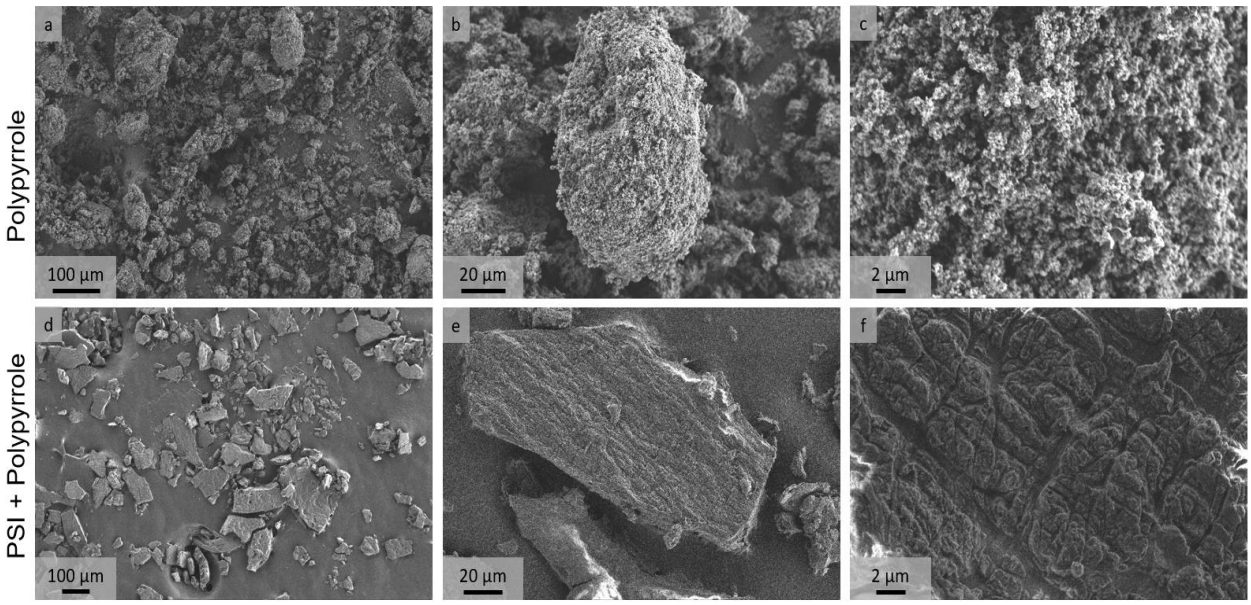

Figure 4.5: Scanning electron microscope images of PPy (a-c) and PSI-PPy powders (d-f). Magnification increases from left to right.

To confirm that the $NaClO_4$ successfully doped the polypyrrole, EDS was performed to confirm the presence of Cl in the polymer (Figure 4.6). The imaged protein-polymer conjugate was rinsed with DI water, so no excess ions should appear unless they are connected to the conjugate. The EDS spectra show that there is a significant Cl signal coming from the polymer, confirming successful doping.

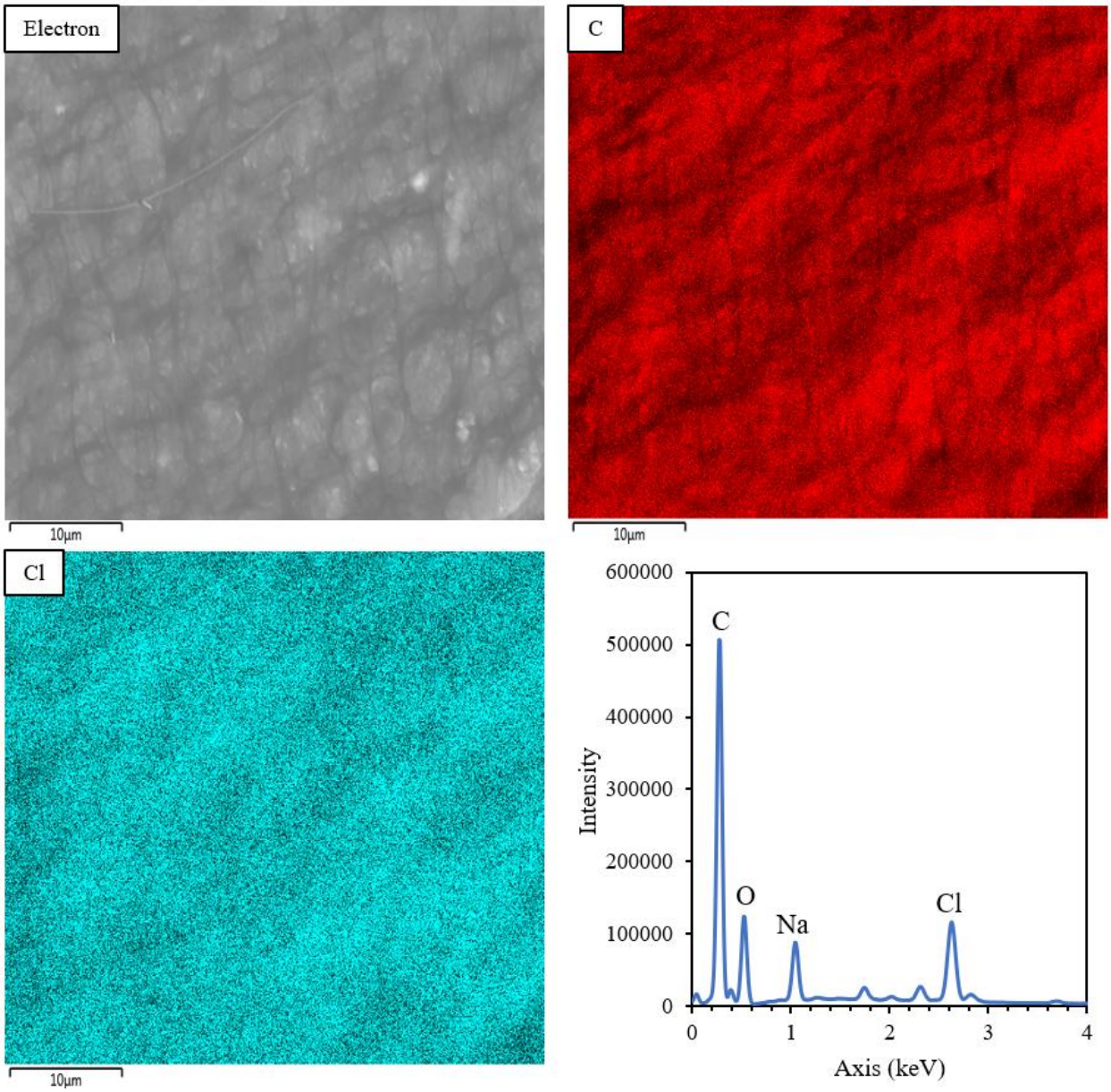

Figure 4.6: EDS map and spectra of PSI-PPy powder showing presence of Cl, indicating successful doping with $NaClO_4$.

Formation of Protein-Polymer Conjugates

A sodium dodecyl sulphate-polyacrylamide gel electrophoresis (SDS-PAGE) was run to assess whether the grown polymer is chemically connected or conjugated with the protein, such as by electropolymerizing monomer directly from the protein, or in contrast, if the polymer is grown in solution by oxidatively formed radicals by PSI, akin to a chemical polymerization. Conjugation

between the protein and polymer should result in an increased molecular weight of the conjugate because the bond would remain unbroken after addition of surfactant. A change in molecular weight of the conjugate should be measureable through SDS-PAGE. If PPy is conjugated to the P_{700} active site of PSI, then the bands in the gel for subunits PsaA and PsaB, which comprise the special chlorophyll pair, should shift upward in an SDS-PAGE gel because of the additional mass. In contrast to conjugation, steric attachments between solution-grown polymer and PSI would likely be broken apart upon addition of surfactant. In such a case, PPy should not diffuse into the gel because of its insolubility, and PSI should separate into subunits that appear in the gel, the same as pure protein.

The gel in Figure 4.7 shows a comparison of the PSI-Py reaction product to the monomer, PSI, UV-deactivated PSI with and without the monomer, and chemically polymerized PPy with and without PSI. All of the samples were subjected to 6 h of illumination before being run through the gel.

The first 3 lanes are the monomer, free protein, and UV-deactivated free protein controls. No bands appear for the monomer or deactivated protein, but multiple bands appear in the unmodified free protein, with subunits PsaA and PsaB comprising the large band at 50 kDa. If PPy is formed and is conjugated to the PSI, the most likely attachment point would be at or near the P_{700} chlorophyll pair reaction site, which is part of PsaA and PsaB and is the site of the most favorable potential for oxidation of Py. As such, the PsaA/PsaB band at 50 kDa should shift up due to an increase in molecular weight. Polyaniline, another conducting polymer, has been grown by using a chlorophyll derivative to seed the polymerization,[20] so attachment to P_{700} is likely if the oxidation occurs at the chlorophyll pair.

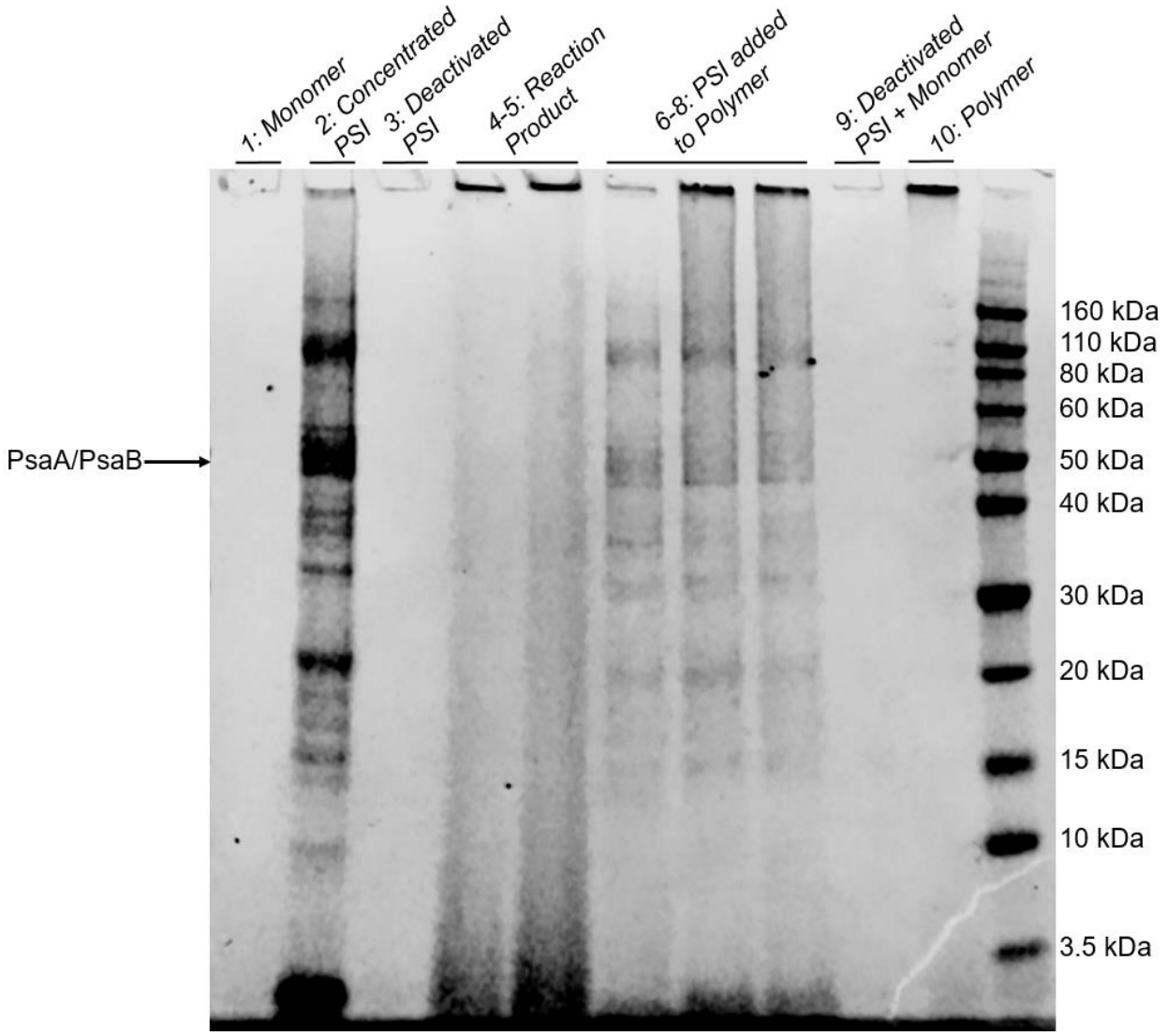

Figure 4.7: SDS-PAGE gel. Lane 1) 0.5 M monomer, lane 2) 20 μM unmodified PSI, lane 3) 20 μM UV-deactivated PSI, lanes 4 & 5) reaction product of 0.5 M monomer with 8 μM & 16 μM PSI, respectively, lanes 6, 7, 8) 4 μM PSI mixed with PPy chemically synthesized from 0.01 M, 0.1 M, and 0.5 M monomer concentrations, respectively, lane 9) 0.5 M monomer with 16 μM of UV-deactivated, lane 10) PPy chemically synthesized from 0.5 M Py, lane 11) reference ladder.

Lanes 4 and 5 show the reaction product of PSI and Py monomer after 6 h of illumination. In these lanes, there is an appearance of a large mass collected at the top of the lanes and some streaking throughout the lower portion of the lanes. The band appears at the top of all the lanes that are expected to have PPy in them (lanes 4, 5, 6, 7, 8, and 10). This band at the top is synthesized PPy that is unable to migrate through the gel because of either insolubility or extensive size.[21,22]

Lane 10 is the PPy control and the only present feature is the band collected at the top, confirming that the band is polymer.

In lanes 4 and 5, the free protein bands seen in lane 2 are no longer present, which suggests conjugation between the polymer and protein.[21] To ensure that the disappearance of the bands is not due simply to aggregation of protein with polymer, PSI was added to differing concentrations of chemically synthesized PPy (lanes 6, 7, and 8). In these three bands, the free protein bands all appear alone with the polymer collecting at the top of the lanes. The presence of bands related to protein in lanes 6, 7, and 8 compared to the absence of bands in lanes 4 and 5 indicate that the protein has been chemically conjugated to the polymer. The absence of all free protein bands and not only the PsaA/PsaB subunits suggests that the conjugated protein is protected by the polymer from denaturation by the SDS.

PSI that is bleached by strong UV light shows no photoactivity in electrochemical cells[23] and was used here as a control to address whether the polymerization reaction was due the photo-assisted redox capabilties of PSI or the presence of protein as a seeding site (lane 9). The absence of bands and polymer at the top of the well in the UV-deactivated protein samples, with and without monomer, show that there is no polymerization; thus, the polymer is formed by a photo-initiated reaction with PSI.

Properties of the PSI-PPy Conjugates

Thermal properties of the PSI-PPy product were compared to pure PSI films by thermogravimetric analysis (TGA). Figure 4.8 shows the TGA curve for PSI, PPy, and PSI-PPy after holding at 100 °C for 30 min to evaporate residual water or monomer. The mass of the samples after the 30 min temperature hold was 0.5 mg, 8.7 mg, and 8.5 mg for PSI, PPy, and PSI-PPy, respectively.

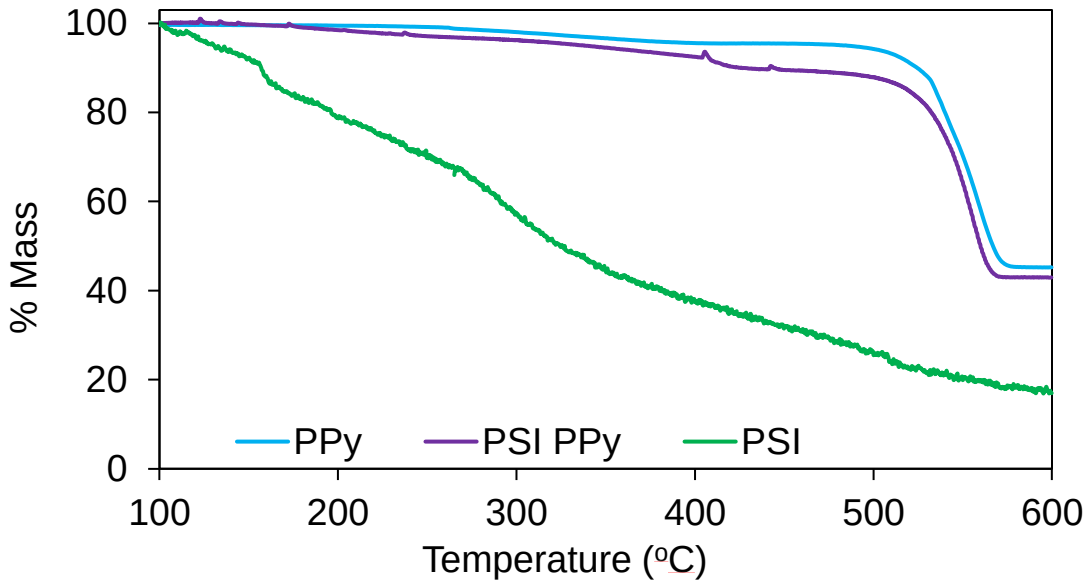

Figure 4.8: Thermogravimetric analysis curves of PPy, PSI, and the PSI-PPy reaction product. Samples were held at 100 °C for 30 min before 10 °C/min ramp to 600 °C.

The PSI-PPy sample exhibits significantly more robust thermal properties as compared to PSI and shows a curve similar to pure PPy. The PPy and PSI-PPy samples lose mass at a slower rate than that of PSI alone until 520 °C where PPy begins to burn off. Comparing the PPy and PSI-PPy curves, both follow a similar trend, but the PSI-PPy sample loses mass at a slightly faster rate than PPy up to 520 °C, which is attributed to the PSI present in the powder. The similarity between the PPy and PSI-PPy curves further supports the successful polymerization of PPy. The PSI-PPy degrades at a slower rate than PSI alone, suggesting that the PPy is thermally protecting the PSI. This trend holds true if the PPy contribution is subtracted from PSI-PPy to compare only the PSI contributions to the thermal properties (Figure 4.9). The TGA data were normalized to remove the behavior of the polymer based on the pure PPy curve.

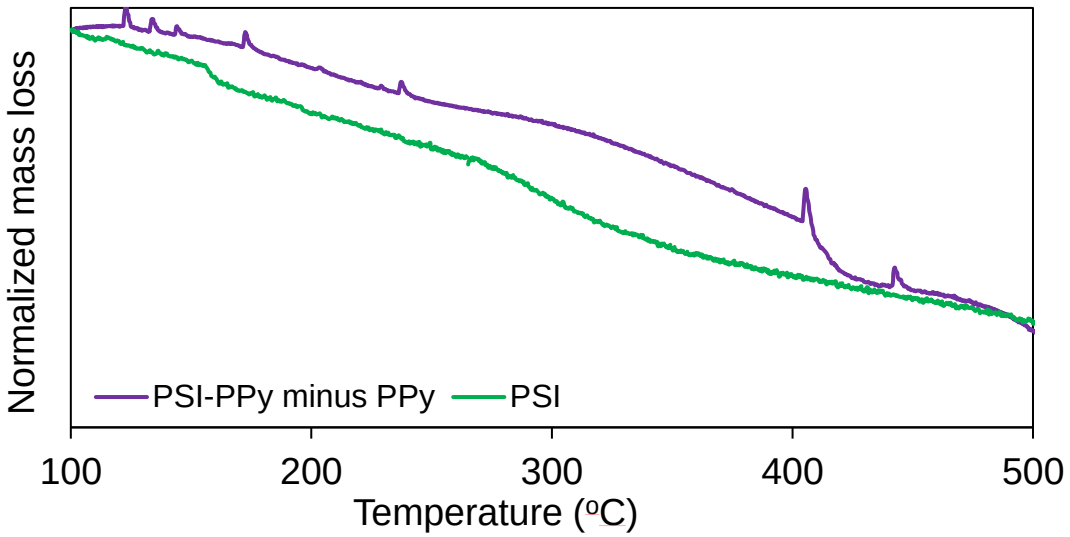

Figure 4.9: Normalized TGA comparing the relative mass loss of PSI in both the pure and PSI-PPy samples.

Electrochemical properties of the protein-polymer conjugates were investigated by measuring the photopotential and photocurrent of the films in an ascorbic acid (AscH):2,6-dichlorophenolindophenol (DCPIP) redox mediator system and comparing them to unmodified PSI films. Figure 4.10a shows the average open circuit potential of seven independently prepared PSI and PSI-PPy multilayer films deposited on gold as well as the photopotential response of PSI deposited atop a PPy film polymerized on gold via applied potential. Figure 4.10b shows the comparison of the magnitude of the photopotential change by normalizing the potential at 20 s to 0 V. Figure 4.10c shows the comparison of photocurrents.

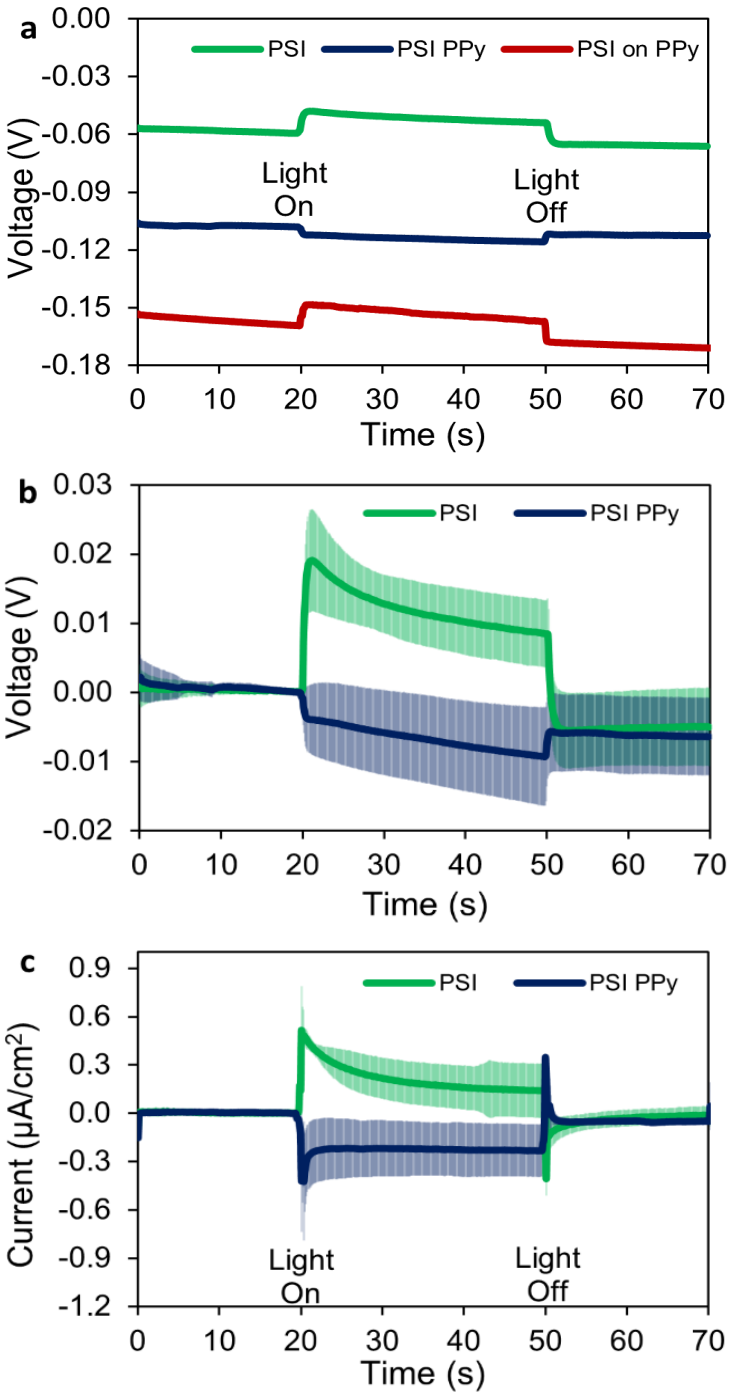

Figure 4.10: Open-circuit potential (OCP) response to photo-illumination of films on gold in a 1:20 mM AscH:DCPIP mediator. Illumination begins at 20 s and ends at 50 s and potentials are vs. Ag/AgCl. Shaded regions are indicative of standard deviation over 7 samples. a) Potential response for pure PSI, PSI-monomer reaction product, and PSI deposited on a PPy film, b) OCP's normalized to 0 V for response magnitude comparison, c) photocurrent response for PSI and PSI-PPy films held at the dark OCP.

A PSI film on bare gold shows a dark open circuit potential around -59 mV, which is increased by 10 mV after 30 s of illumination. The redox potential of PPy is known to be -200 mV vs. Ag/AgCl;[24] therefore, PPy deposited onto a gold substrate should lower the potential. Both bare gold and an independently electropolymerized PPy film show no photoactivity, so any change in Figure 4.10 results from the redox properties of the protein. The PSI-PPy reaction product has a dark open circuit potential of -110 mV, and the potential decreases by 10 mV after 30 s of illumination, the opposite potential change of PSI alone. A decrease in photopotential indicates that there is a decrease in the ratio of oxidized to reduced species near the electrode and an increase indicates the opposite.

The photocurrent trends mirror the photopotential trends where PSI generates 0.14 $\mu A/cm^2$ of cathodic current and PSI-PPy generates -0.23 $\mu A/cm^2$ of anodic current. This cathodic photocurrent for PSI alone in the AscH:DCPIP couple has been attributed to the fast oxidation of $DCPIPH_2$ at the P_{700} site of PSI to yield an excess of oxidized species that are readily reduced at the electrode.[25] An anodic photocurrent for PSI-PPy suggests that the presence of the polymer alters the relative redox kinetics at the PSI active sites.

To investigate connection between the protein and polymer, PSI was deposited on top of an independently grown PPy film. This film has a lower dark OCP of -156 mV because of the presence of pure PPy on the electrode, but the potential increases upon illumination, showing the same trend as PSI on bare gold. Drop-casting PSI on top of a PPy film does not result in direct connections between the protein and the polymer, so the electrochemical properties of PSI remain the same as PSI on a metal electrode. This result further supports the direct connection between the polymer and protein in the PSI-PPy reaction product because of the change in photoelectrochemical capabilities.

PPy is an instrinsically conducting material, and if sufficient polymer is grown and connected to photoactive PSI, then the resulting product should be a photoactive and conductive composite. The conductivity of PPy and PSI-PPy reaction product powders was measured by compressing the powders between two metal electrodes. The setup can be seen in Figure 2.5. The conductivity was calculated using the following equation:

$$\kappa = \frac{h}{R * A} \quad [4\text{-}1]$$

where κ = electrical conductivity (S/cm), h = powder height (cm), R = electrical resistance (Ω), and A = cross sectional area of powder (cm^2).[26] For simplicity of measurement and because of the non-uniformity of particle sizes as shown in the SEM images, the pellets were assumed to have no porosity due to the compressive force, which artificially lowers the measured conductivities.

The conductivity for pure PPy was measured to be $2.3x10^{-4} \pm 1.4x10^{-4}$ S/cm, similar to other PPy powder conductivities in the literature.[27] If the PSI-PPy powder is photoactive, then there should be a difference in conductivity when measured in darkess and under illumination. In the dark, the conductivity was $1.93x10^{-5} \pm 7.5x10^{-8}$ S/cm and in the light it was $3.09x10^{-5} \pm 1.8x10^{-6}$ S/cm, a 60% increase in conductivity upon illumination. Due to the constraints of the testing apparatus, the powders were illuminated only from the side, leaving the majority of the cross sections of the pellets in the dark, so the conductivity of the PSI-PPy powder should be higher under more complete illumination. The order of magnitude decrease in conductivity compared to the pure PPy is likely due to the insulating properties of the non-electron conducting portions of PSI. The conductivity measurements confirm that conducting polymer was grown and is interfaced with PSI protein to form a photoactive, conducting network.

Conclusions

Pyrrole was successfully polymerized using the photo-oxidative properties of PSI to form a photoactive and conductive PSI-PPy conjugate. The polymerization occurs by mixing PSI with both Py monomer and a dopant and then illuminating the solution to initiate the polymerization. Growth of PPy was confirmed by comparing the reaction product to both PSI and independently polymerized samples through FTIR, TGA, and contact angle. TGA showed that the PSI-PPy conjugate is more thermally robust than PSI alone, and the conjugation to a polymer protects the protein from early degradation. SEM images showed a platelet morphology for the PSI-PPy conjugates and coalesced nanoparticle morphology for electrochemically and chemically grown polymer. Successful conjugation between PSI and the grown PPy is supported by SDS-PAGE results showing that protein is attached to the polymer and does not migrate into the gel as compared to protein that was mixed with pre-synthesized polymer. Additionally, the PSI-PPy conjugate alters the photoelectrochemical properties compared to pure PSI because the connected conjugate can transfer electrons directly from an electrode to PSI. The conjugate was also measured to be conductive and photoactive in solid-state systems, proving that conducting PPy was grown and is well-connected to the PSI proteins.

This is the first proof of polymerization by PSI to form a protein-polymer conjugate and among the first that uses an unmodified protein to grow a chemically connected conducting polymer. The conjugate is both conductive and photoactive, enabling use in both liquid and solid-state solar conversion processes. Integrating PSI into solid-state systems is notoriously difficult because of connectivity issues between the protein and conducting polymers, and the PSI-PPy conjugate can greatly mitigate this issue. The capability of PSI to perform an oxidative polymerization can be expanded to grow different polymers to obtain new classes of protein-

polymer conjugates with unique photoelectrochemical properties through facile synthesis methods.

References

1. Grigoletto, A., Tedeschini, T., Canato, E. & Pasut, G. The evolution of polymer conjugation and drug targeting for the delivery of proteins and bioactive molecules. *Wiley Interdiscip. Rev. Nanomedicine Nanobiotechnology* **13**, 1–33 (2021).

2. Thiele, M. J. *et al.* Enzyme-Polyelectrolyte Complexes Boost the Catalytic Performance of Enzymes. *ACS Catal.* **8**, 10876–10887 (2018).

3. Chen, C., Ng, D. Y. W. & Weil, T. Polymer bioconjugates: Modern design concepts toward precision hybrid materials. *Prog. Polym. Sci.* **105**, 101241 (2020).

4. Li, X. *et al.* Highly active enzyme–metal nanohybrids synthesized in protein–polymer conjugates. *Nat. Catal.* **2**, 718–725 (2019).

5. Saboe, P. O. *et al.* Biomimetic wiring and stabilization of photosynthetic membrane proteins with block copolymer interfaces. *J. Mater. Chem. A* **4**, 15457–15463 (2016).

6. Gizzie, E. A. *et al.* Photosystem I-polyaniline/TiO_2 solid-state solar cells: simple devices for biohybrid solar energy conversion. *Energy Environ. Sci.* **8**, 3572–3576 (2015).

7. Kazemzadeh, S., Riazi, G. & Ajeian, R. Novel Approach of Biophotovoltaic Solid State Solar Cells Based on a Multilayer of PS1 Complexes as an Active Layer. *ACS Sustain. Chem. Eng.* **5**, 9836–9840 (2017).

8. Lubner, C. E., Grimme, R., Bryant, D. A. & Golbeck, J. H. Wiring photosystem I for direct solar hydrogen production. *Biochemistry* **49**, 404–414 (2010).

9. Grimme, R., Lubner, C., Bryant, D. & Golbeck, J. Photosystem I/molecular wire/metal nanoparticle bioconjugates for the photocatalytic production of H2. *Chemtracts* **21**, 207–209 (2008).

10. Sadki, S., Schottland, P., Brodie, N. & Sabouraud, G. The mechanisms of pyrrole electropolymerization. *Chem. Soc. Rev.* **29**, 283–293 (2000).

11. Jung, Y., Spray, R. L., Kim, J. H., Kim, J. M. & Choi, K. S. Selective polymerization of polypyrrole in silica mesopores using an in situ generated oxidizing agent on a silica surface. *Chem. Commun.* **46**, 6566–6568 (2010).

12. Arrondo, J. L. R. & Goñi, F. M. Structure and dynamics of membrane proteins as studied by infrared spectroscopy. *Prog. Biophys. Mol. Biol.* **72**, 367–405 (1999).

13. Saoudi, B. *et al.* XPS study of the adsorption mechanisms of DNA onto polypyrrole particles. *Spectroscopy* **18**, 519–535 (2004).

14. Istakova, O. I., Konev, D. V., Medvedeva, T. O., Zolotukhina, E. V. & Vorotyntsev, M. A. Efficiency of Pyrrole Electropolymerization under Various Conditions. *Russ. J. Electrochem.* **54**, 1243–1251 (2018).

15. Karami, H. & Nezhad, A. R. Investigation of pulse-electropolymerization of conductive polypyrrole nanostructures. *Int. J. Electrochem. Sci.* **8**, 8905–8921 (2013).

16. Lima, R. M. A. P., de Oliveira, M. C. A. & de Oliveira, H. P. Wearable supercapacitors based on graphene nanoplatelets/carbon nanotubes/polypyrrole composites on cotton yarns electrodes. *SN Appl. Sci.* **1**, 1–11 (2019).

17. Wang, T., Zhong, W., Ning, X., Wang, Y. & Yang, W. Facile Route to Hierarchical

Conducting Polymer Nanostructure: Synthesis of Layered Polypyrrole Network Plates. *J. Appl. Polym. Sci.* **114**, 3855–3862 (2009).

18. Shinde, S. S., Gund, G. S., Dubal, D. P., Jambure, S. B. & Lokhande, C. D. Morphological modulation of polypyrrole thin films through oxidizing agents and their concurrent effect on supercapacitor performance. *Electrochim. Acta* **119**, 1–10 (2014).

19. Chen, X., Devaux, J., Issi, J. P. & Billaud, D. Chemically oxidized polypyrrole: Influence of the experimental conditions on its electrical conductivity and morphology. *Polym. Eng. Sci.* **35**, 642–647 (1995).

20. Thanpitcha, T., Sirivat, A., Jamieson, A. M. & Rujiravanit, R. Synthesis of polyaniline nanofibrils using an in situ seeding technique. *Synth. Met.* **158**, 695–703 (2008).

21. Wilson, J. T. *et al.* Enhancement of MHC-I Antigen Presentation via Architectural Control of pH-Responsive, Endosomolytic Polymer Nanoparticles. *AAPS J.* **17**, 358–369 (2015).

22. Theodorou, A. *et al.* Protein-polymer bioconjugates via a versatile oxygen tolerant photoinduced controlled radical polymerization approach. *Nat. Commun.* **11**, 1–11 (2020).

23. Wolfe, K. D. *et al.* Layer-by-Layer Assembly of Photosystem I and PEDOT:PSS Biohybrid Films for Photocurrent Generation. *Langmuir* **37**, 10481–10489 (2021).

24. G. Street, T. Clarke, R. Geiss, V. Lee, A. Nazzal, P. P. & Uger, J. S. Characterization of Polypyrrole. *J. Phys. Colloq.* **44**, 9 (1983).

25. Passantino, J. M., Wolfe, K. D., Simon, K. T., Cliffel, D. E. & Jennings, G. K. Photosystem I Enhances the Efficiency of a Natural, Gel-Based Dye-Sensitized Solar Cell. *ACS Appl. Bio Mater.* **3**, 4465–4473 (2020).

26. Hoffmann, V., Rodriguez Correa, C., Sautter, D., Maringolo, E. & Kruse, A. Study of the electrical conductivity of biobased carbonaceous powder materials under moderate pressure for the application as electrode materials in energy storage technologies. *GCB Bioenergy* **11**, 230–248 (2019).

27. Håkansson, E., Lin, T., Wang, H. & Kaynak, A. The effects of dye dopants on the conductivity and optical absorption properties of polypyrrole. *Synth. Met.* **156**, 1194–1202 (2006).

Chapter 5

Photoactive, Conductive Biohybrid Films by Polymerization of Polypyrrole through Voids in PSI Multilayer Films

Introduction

Embedding PSI within a polymer matrix to provide more direct connections to donate or accept electrons from PSI has been explored in multiple systems. Badura *et al*. entrapped PSI within an Os containing redox polymer hydrogel to immobilize PSI and serve as an electron donor in an electrochemical cell.[1] Vapor-phase polymerization of poly(3,4-ethylenedioxythiophene) polystyrene sulfonate (PEDOT:PSS) over multilayer PSI films of varying thickness in liquid electrochemical cells showed enhanced film pseudo-capacitance up to a limiting thickness of PSI before the PSI blocked polymer connection to the electrode, lowering performance.[2] PSI has also been interfaced with conducting polymer matrices into solid-state devices to help move away from liquid devices. Gordiichuck *et al.*[3] explored PSI monolayers on TiO2 trapped in polytriarylamine, whereas Kazemzadeh *et al.*[4] and Dervishogullari *et al.*[5] both explored layering PSI multilayers with conducting polymers.

To improve connection in solid-state applications, Gizzie *et al*. explored using the films of Pani-PSI that were electropolymerized directly from an aniline and PSI solution.[6] This approach improves connections between the polymer and protein compared to the layering systems, but the concentration of PSI entrapped within the film was estimated to be very low at approximately 15 nmol/cm^3. This approach was also used to make a solid-state device using the same polymerization technique. The device was also shown to retain over 85% of the original photocurrent output over 20 days.[7] Solid-state devices are expected to retain performance longer than liquid analogues

because PSI readily creates reactive oxygen species that degrade the protein in aqueous solutions and the absence of antioxidants.[8]

In this work, an approach is explored to embed high concentrations of PSI into a conducting polymer matrix that can be used for both liquid and solid-state applications. A thick multilayer of PSI is deposited onto a gold surface and pyrrole is electrochemically polymerized around the protein film. This method allows for much higher concentrations of protein within the film as compared to Gizzie's approach,[6,7] and the amount of protein deposited can be controlled. This method leads to potential connections between the proteins and the polymer to increase performance.

Results and Discussion

Visual Properties

Multilayer films of PSI were drop cast on gold substrates that were covered with an electrochemical mask that had a hole punched out to create an active electrochemical surface with a known geometric area. These substrates were then exposed to pyrrole (Py) monomer solution and were biased at a set potential until a specified amount of polypyrrole (PPy) was grown, which was measured by the charge passed through the electrode. Representative visual images of the resulting films are shown in Figure 5.1.

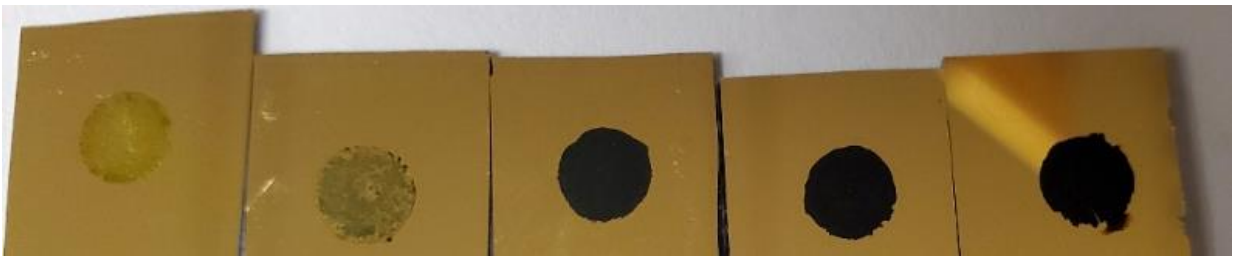

Figure 5.1: PSI multilayer films after polymerization of PPy. From left to right, the amount of charge passed was 0, 1, 5, 10, 15 mC total or 0, 14, 70, 140, and 210 mC/cm^2.

Visually, the pure multilayer of PSI is a non-uniform, translucent, and relatively bright green film. The non-uniformity is typical of the drop casting deposition approach. After 14 mC/cm^2 of PPy is deposited, the film visually remains non-uniform, but it becomes less transparent and a darker shade of green, characteristic of PPy. At 70 mC/cm^2 and beyond, the entire surface is covered by PPy and is completely opaque.

ATR-FTIR analysis was used confirm the presence of both PSI and PPy in electropolymerized films. Figure 5.2 shows the characteristic spectra for films of pure electropolymerized PPy with significant peaks at 1594 (N-H bending) and 930 (C-H sp^2 bending) cm^{-1}, films of pure PSI with peaks at 1656 (Amide I) and 1531 (Amide II), and two films of PPy that were electropolymerized at a potential of 0.65 V vs. Ag/AgCl, through a film of PSI. Most notably, the spectra for the PSI-PPy films show a peak growing at 930 cm^{-1}. Additionally, the valley between the Amide I and II peaks is higher than the pure spectra, suggesting growth of an aromatic N-H peak as in the PPy spectra. This valley becomes shallower and the ratio of the height of the Amide I peak to that evolving at 1540 cm^{-1} decreases from 1.71, to 1.03, to 0.98 as polymerization time is increased, consistent with the presence of more PPy. Importantly, the IR spectra shows that the PSI remains in the film after electropolymerization.

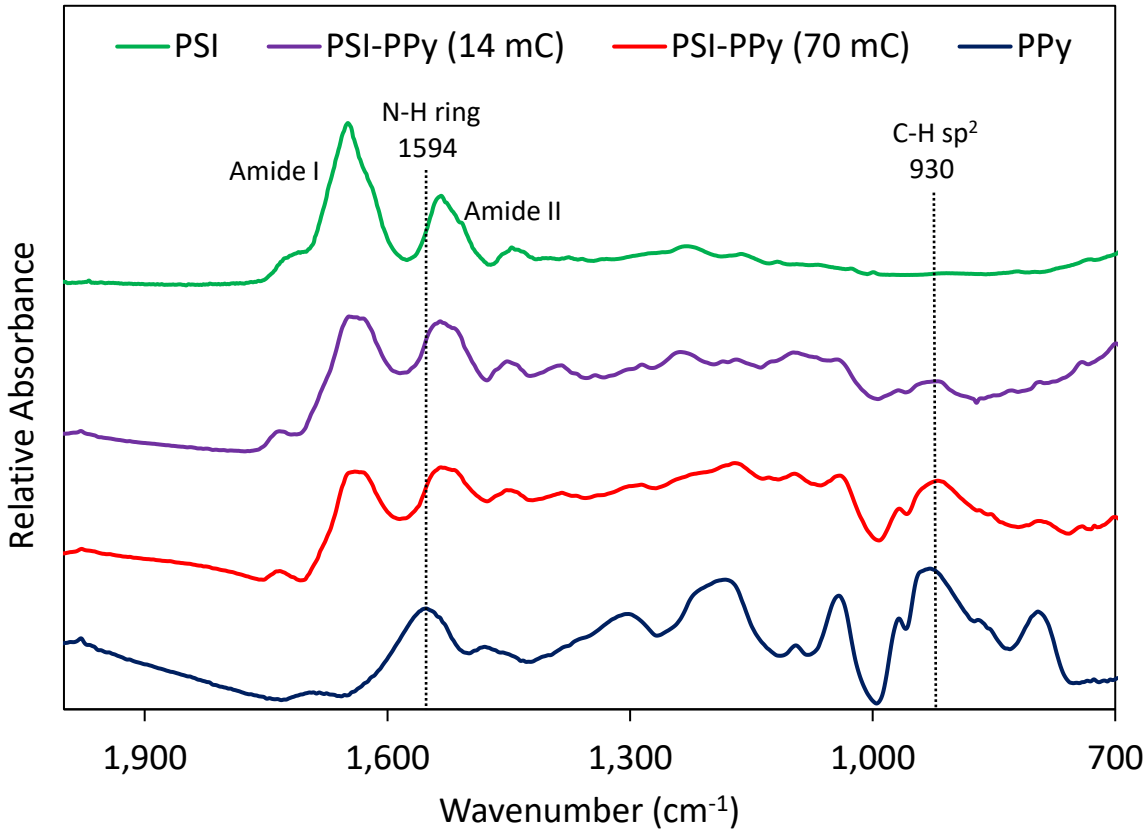

Figure 5.2: IR spectra of PSI, PPy, and PSI-PPy films. PPy was grown at an applied potential of 0.65 V vs. Ag/AgCl for bare gold for samples with PSI multilayers.

Polymerization Kinetics

After PSI was confirmed to be present in the polymer films, thicknesses were measured to determine if the Ppy grows around the protein film or rather, pushes the PSI film up as it grows. Figure 5.3 shows the average thickness of films that were polymerized around a multilayer of PSI or on bare gold. If the polymer film raises the PSI film during polymerization, then a similar change in average height should be seen. At 210 mC/cm^2 of PPy deposited onto bare gold, the film is 1500 nm thick. In the PSI-PPy films, there is a height difference of only 600 nm between the pure PSI multilayer and the composite film with 210 mC/cm^2 of PPy applied. Additionally, there is no major change in height until 210 mC/cm^2 was applied on bare gold, but the average height increased after only 140 mC/cm^2 was applied with a PSI film present. Visually, the entire surface

has a dark film of PPy at 70 mC/cm^2, but the height is not increased above that for the pure PSI multilayer. These two trends suggest that the PPy film being polymerized through a PSI multilayer is growing through the film and filling in void space inside the PSI multilayer instead of pushing the protein film up.

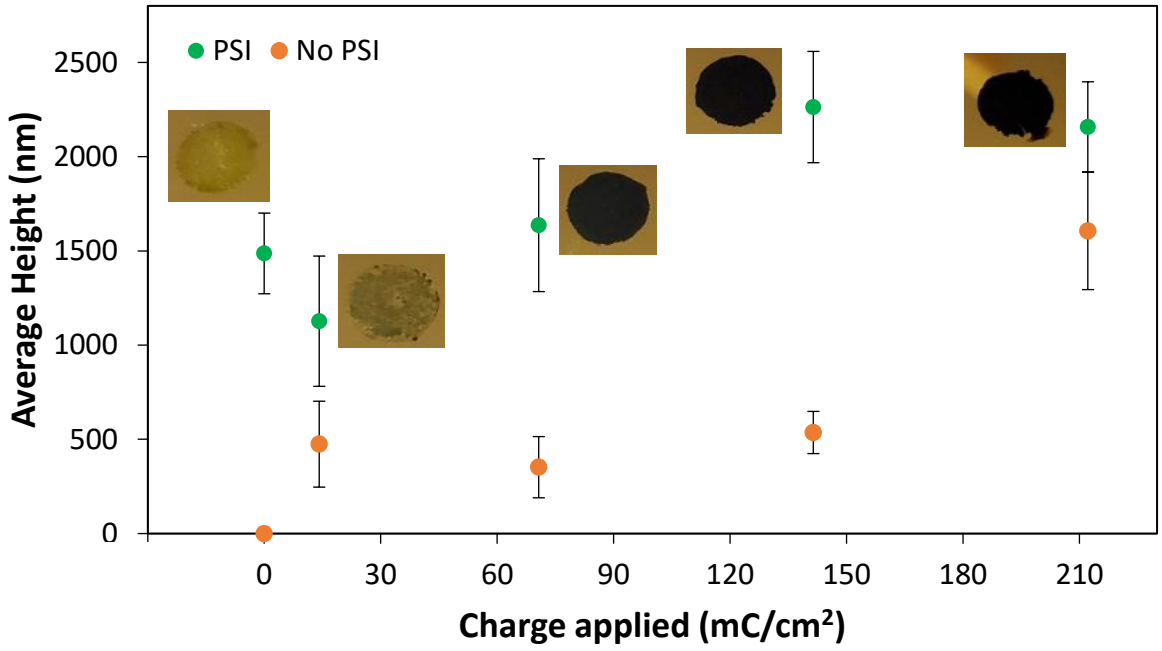

Figure 5.3: Average height of PPy films grown on bare gold or on a gold surface with a multilayer film of PSI.

A PSI film of 2.5 µm or greater that is drop-cast on a gold surface begins to block light from penetrating through the entire film, providing a theoretical maximum multilayer height.[9] However, the PPy will absorb some light, effectively lowering the maximum thickness that allows full light penetration in the film. The thickness measurements show the amount of polymer that can be added without increasing the composite film thickness too much. In the case of the 1.5 µm multilayer films, a deposition of 70 mC/cm^2 visually covers the active surface area without significantly raising the average film height. Profilometry scans for the PSI, PPy, and PSI-PPy films are shown in Figure 5.4. The profilometry data show that the films containing PSI had more

variability in the surface compared to the PPy samples, which had smooth sections as well as large clusters of islands.

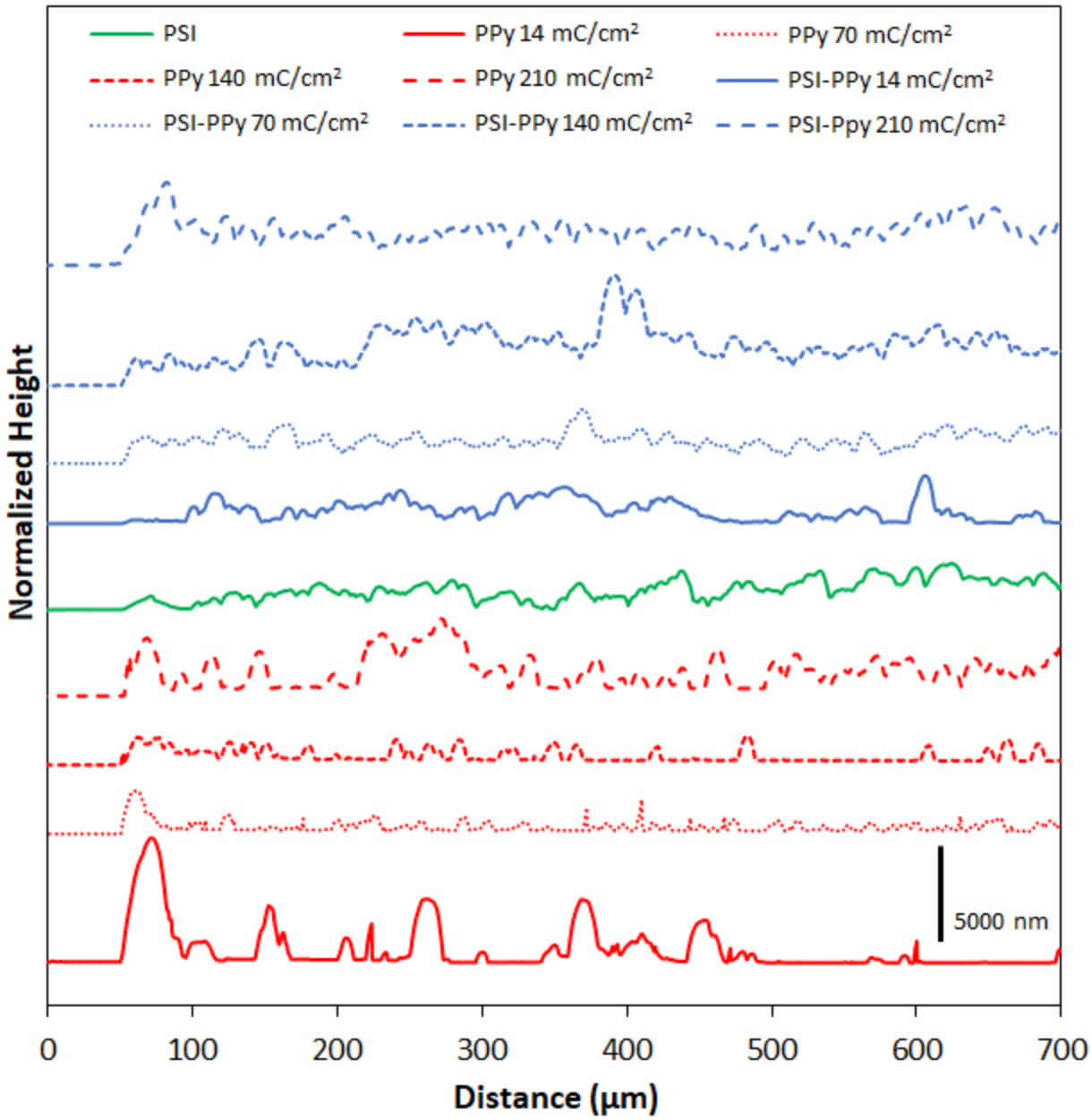

Figure 5.4: Profilometry topographic scan of PSI, PPy, and PSI-PPy films on gold. All data is normalized to show relative heights.

The PSI multilayers were drop-cast from a 40 µL drop of 4 µM PSI. The drop-casting results in a film of approximately 1.5 µm, as shown in Figure 5.3. This multilayer film is estimated to have a PSI molar concentration of 440 nmol/cm^3 by modeling the film as a cylinder of 1.5 µm

height. This is 30x more protein than in previous work where Pani was electropolymerized in the presence of PSI solution; in that work, the concentration of PSI proteins was calculated to be 15 nmol/cm^3 in the polymer film.[7]

The rate of film growth can be investigated by measuring the amount of charge passed at a set applied potential over time, which is directly related to the amount of polymer deposited.[10] A multilayer of PSI proteins should reduce the Ppy growth rate by hindering Py diffusion to the electrode and constraining film growth to certain void regions of the PSI film.[11] A goal for this research is to improve PSI loading and connectivity in a PPy film, so determining if a PSI film can be too thick for polymer to grow is important.

Figure 5.5 shows the time required to deposit 15 mC of charge over a gold substrate for bare gold and PSI films of varying thicknesses. The thickness was controlled by changing the concentration (4, 2, and 1 μM) of PSI in a 40 μL drop that was drop-cast on an active surface area of 0.24 cm^2. The concentration of PSI in the 40 μL drop is proportional to the thickness of the multilayer film on the surface since the deposition area is held constant.[12] The presence of PSI has a dramatic effect on the polymerization rate. 15 mC was deposited after 60 s on bare gold but took over 220 s (nearly a four-fold increase) if there was a film of PSI on the substrate. The amount of PSI in the concentration ranges examined had negligible effect on the growth rate, but PPy was able to grow through all PSI films similarly. This similarity in growth rates despite the PSI thickness indicates that Ppy growth is limited to networks of voids in the PSI film, as we expect similar PSI void fractions near the electrode surface in all of these films. By growing through the PSI voids, we expect that the composite film has PSI-rich and PPy-rich regions with good interfacial contact between the protein and polymer regions.

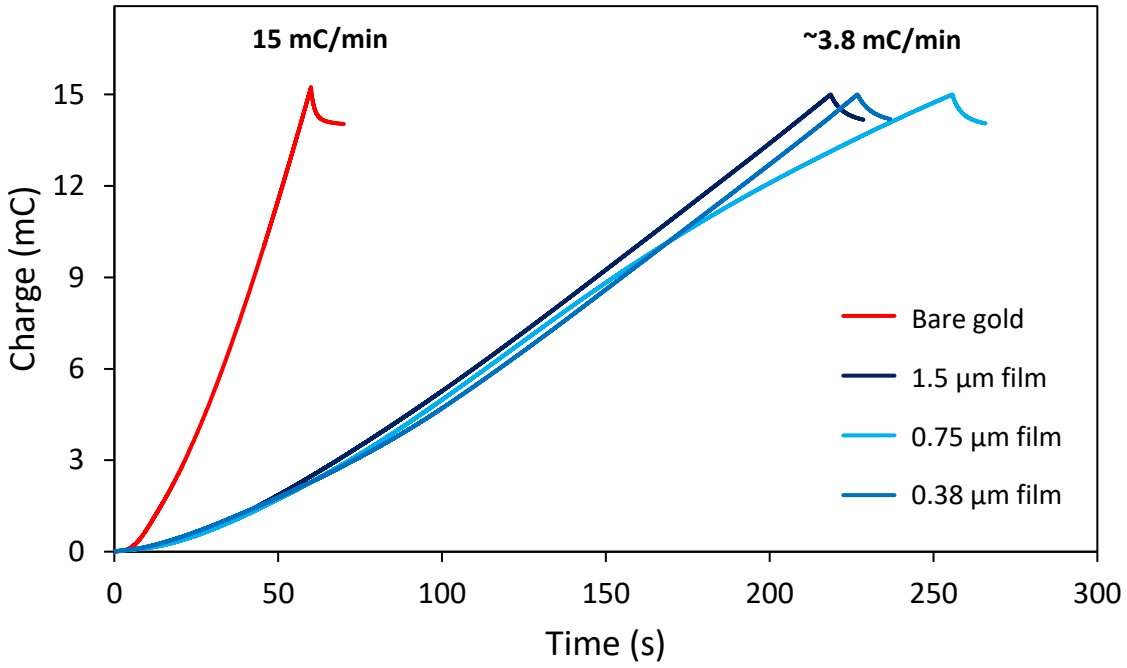

Figure 5.5: Growth rate in the presence and absence of PSI with an applied voltage of 0.65 V vs. Ag/AgCl in a 0.242 cm2 active area. 40 µL drops of PSI solution was drop-cast for each film.

Contact angles were measured to investigate the surface properties of the protein-polymer films. Using the principles of the Cassie Equation [Eq. 2-8] described in Chapter 2, the composition of the surface area of the film can be estimated by contact angles. If PPy grows around the PSI proteins in the film, there should be a critical thickness where all the PSI becomes covered so that the surface should produce the same contact angle as a pure PPy film at that thickness and beyond. If the contact angle does not change to have properties similar to a pure PPy surface, then that would suggest that the PSI is being raised as the film grows and remains on the surface of the film. Figure 5.6 shows the measured contact angles for PSI-PPy films with increasing amounts of polymer, as well as the contact angles for the pure species and the gold substrate.

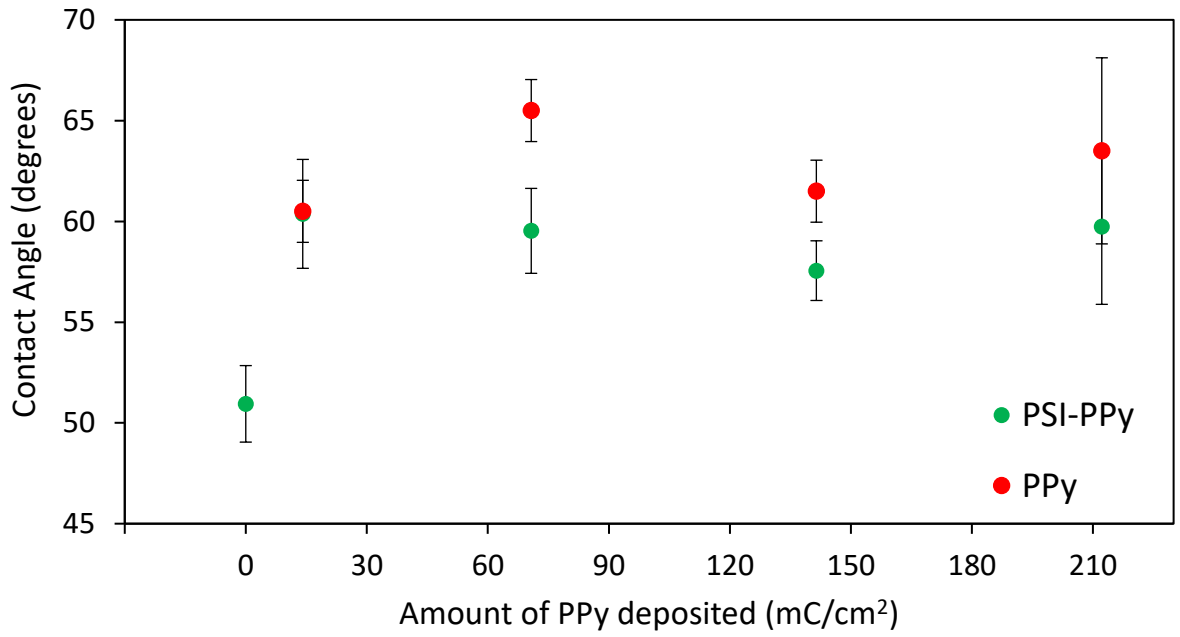

Figure 5.6: Contact angles of PPy and PSI-PPy films with different amounts of PPy grown. Error bars represent the standard deviation of 3 measurements.

The contact angles of all PSI-PPy films are significantly higher than a PSI multilayer even with 14 mC/cm^2 of polymer, which does not completely alter the visual appearance of the protein film as seen in Figure 5.1. The contact angle of pure PPy is dependent on the redox state of the polymer and can range from superhydrophilic to superhydrophobic by externally applying charge to the polymer and changing the roughness.[13] A more positive charge is related to higher contact angles.[14] The presence of PPy is influencing the contact angle of the surfaces with PSI, even at low concentrations. The rise in contact angle does confirm that PPy is growing through the PSI film rather than raising the PSI film because the contact angle of the film increases with polymer growth to a value that is similar to that of a pure Ppy film.

Electrochemical Performance

EIS was used to examine the ion transfer characteristics of the PPy films. Figure 5.7 shows the EIS spectra with increasing amounts of PPy grown at a constant applied potential on a bare gold surface (Figure 5.7a) and on a gold surface coated with a PSI multilayer film (Figure 5.7b).

In both cases, the impedance of the films decreases with more PPy growth, which is indicated by the lowering of the spectra at the low- to mid-range of frequencies in both plots. This lowering of the impedance spectra is due to the high pseudocapacitance of PPy. Pseudocapacitance is a result of charge transfer processes between the electrode and electrolyte interface that show similar behavior to a true capacitor.[15] Figure 5.7b shows that a PSI film has a slightly higher impedance than that of bare gold due to the resistance of the film against ion transfer. PSI films tend to have a lower capacitance, and thus higher impedance, than those for films with conducting polymer present due to the insulating properties of the protein.[2,16,17]

The shape of the curves in the low- to mid-range frequencies is also different between the two cases at similar impedances. This is most noticeable for the PSI film with 7 mC/cm^2 polymer deposited. In the region between 10^1 and 10^3 Hz, the impedance value is higher than that for bare gold closer to 10^3 Hz and then has a lesser slope and shows less impedance as the frequency approaches 10^1 Hz and lower. This behavior at this low charge is consistent with a dense composite film near the electrode but a higher ratio of PSI to polymer moving away from the electrode. At intermediate frequencies, we are sampling the properties near the solution-film interface, but at low frequencies, we are examining the properties near the metal-film interface. These results show that, even though the protein film has insulating properties, PPy can be grown through the protein multilayer and yield composite films that perform similarly or better than a pure PPy film.

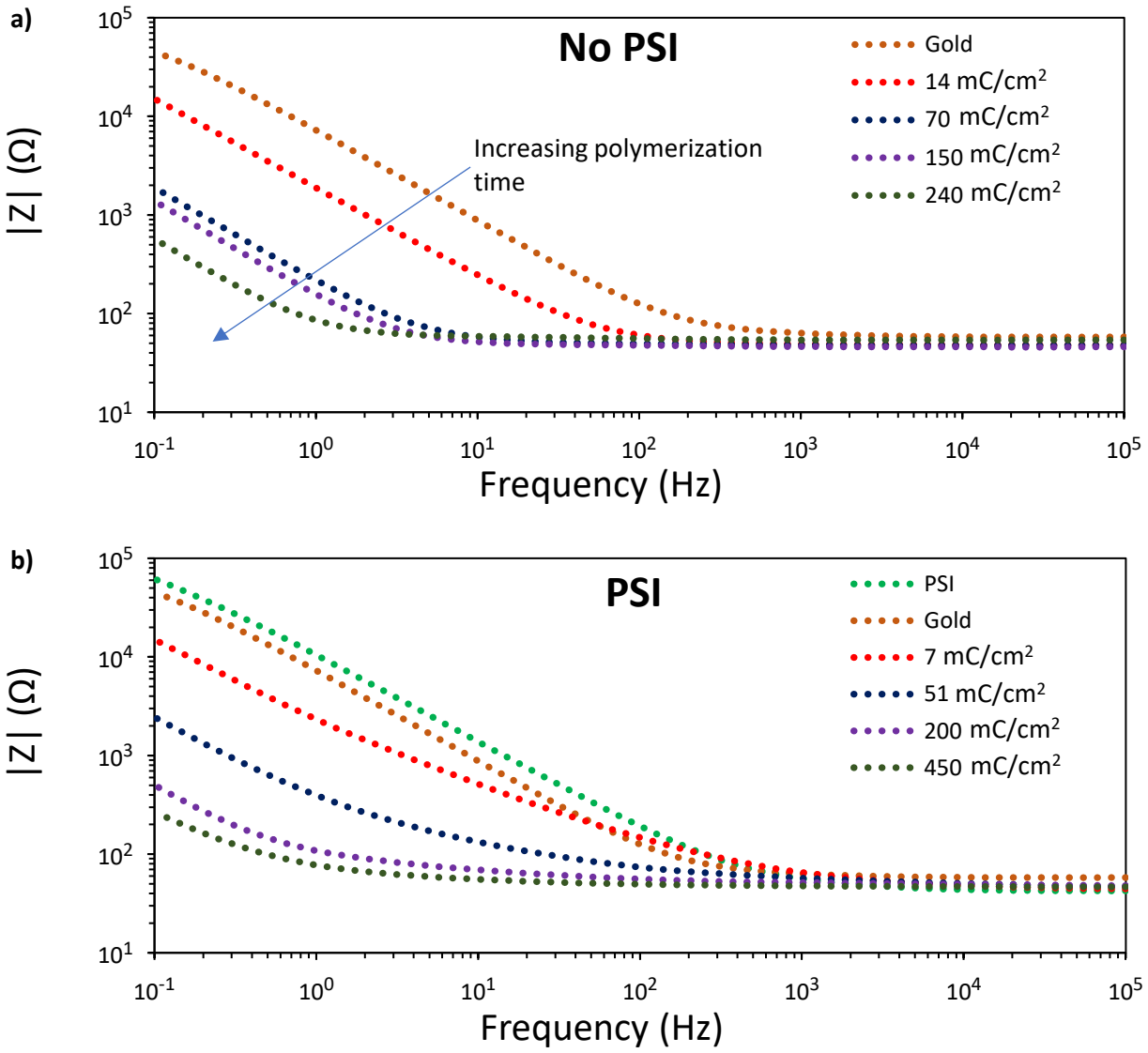

Figure 5.7: EIS spectra of PPy films grown at constant potential on a) bare gold and b) around a PSI multilayer film on bare gold. Measurements were taken in an aqueous solution of KCl.

The EIS data were fit to the equivalent circuit model shown in Figure 5.8. The equivalent model has four components: R_s is the solution resistance, R_{ct} is the charge-transfer resistance, C_{dl} is the double layer capacitance, and Z_w is the Warburg impedance. The circuit was used to compare the change in the four component parameters of the system, which is shown in Table 5.1.

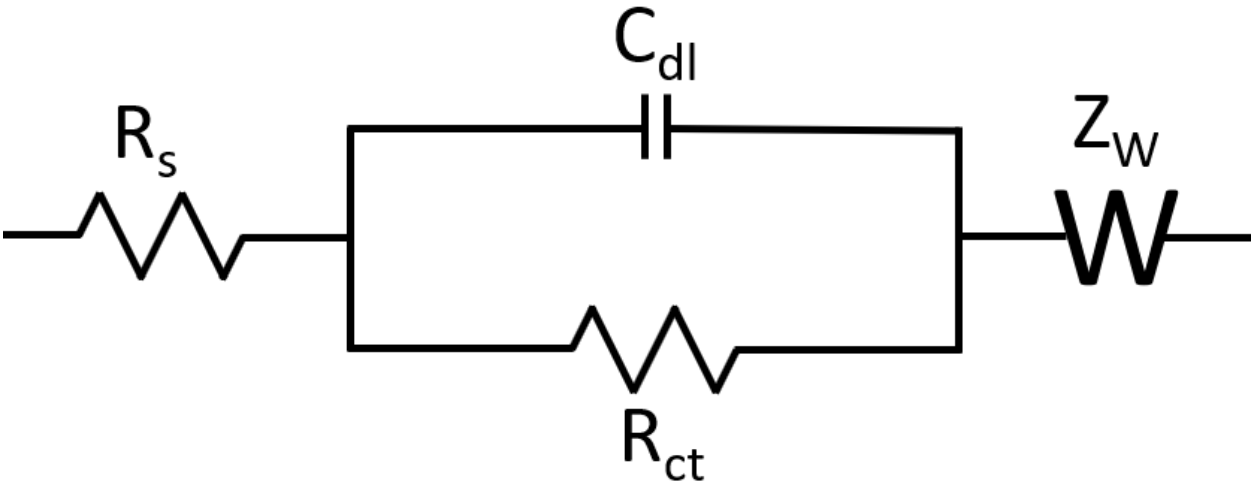

Figure 5.8: Equivalent circuit of PPy and PSI-PPy films on gold surface.

Table 5.1: Extracted electrochemical parameters of PSI, PPy, and PSI-PPy films.

	PSI					No PSI				
Charge (mC/cm^2)	**0**	**7**	**51**	**200**	**450**	**0**	**14**	**70**	**150**	**240**
C_{dl} ($\mu F/cm^2$)	64	469	4186	19806	36314	91	375	4851	4806	12372
Z_W ($S\ s^{1/2}$)	$5x10^{-4}$	$4x10^{-4}$	0.002	0.008	0.014	0.001	0.002	0.016	0.030	0.036

The R_s values for each spectrum was between 40-50 Ω. The value for R_{ct} could not be accurately calculated from the given spectra but was fit to be under 100 Ω for all spectra except the 200 and 450 mC/cm^2 samples with PSI. The capacitance of each film increases as more PPy is deposited due to the high pseudocapacitance of the conducting polymer. A pure PSI film has similar capacitive properties to bare gold, but as PPy is polymerized, the capacitance rises more than that for a PPy film without PSI. A higher capacitance is indicative of good connectivity between the conducting polymer and the electrode. After 7 mC/cm^2 of PPy is applied to a PSI film, the capacitance is 469 $\mu F/cm^2$, which is 7-fold more than PSI by itself and is also higher than a PPy film produced from twice the amount of charge. At an applied charge of 200 mC/cm^2, the PSI-PPy film has a capacitance of 19806 uF/cm^2, which is more than double that of the PPy film

of similar charge (240 mC/cm^2). The higher pseudocapacitance for the composite films suggests that the composite film has more conductive interface to charge with ions than the pure Ppy film.

Both photovoltages and photocurrents were measured to investigate the electrochemical properties of the protein-polymer films. These were measured by illuminating the samples for 30 s and measuring the change in potential and flow of current. The photovoltages were measured in a ferri/ferrocyanide mediator solution while the photocurrents were measured with an ascorbic acid: 2,6-dichlorophenolindophenol (AscH:DCPIP) mediator couple.

For the photovoltages shown in Figure 5.9a, the films are still photoactive up to at least 140 mC/cm^2 of deposited PPy. The most notable difference between the films is that the dark open circuit potential decreases as the amount of PPy increases. The potential of PPy is lower than a bare gold surface or PSI-covered gold surface, so the decrease in dark open circuit potential is consistent with the growth of more PPy, which is affecting the electrochemical properties.[18] Even with thicker films of PPy, the PSI-PPy film still maintains similar photopotential activity.

Figure 5.9b shows the peak photocurrents measured for an unmodified PSI film and PSI films with increasing amounts of PPy grown through them. Pure PPy shows no photoactivity with the AscH:DCPIP mediator on gold, but the addition of PSI results in cathodic photocurrent generation. As more PPy grows, the photocurrent decreases due to the PPy absorbing more light, reducing the amount that is absorbed by PSI. The photocurrent decreases from 490 to 310 nA/cm^2 of after 14 mC/cm^2 of PPy is grown, and the photocurrents continue to decrease and plateau once 70 mC/cm^2 of PPy is deposited.

PSI is known to strongly absorb light at 680 nm wavelength of light while PPy does not, so even with a thick layer of PPy, PSI is still able to absorb some light and generate a limited photocurrent.[19] This performance is different compared to previous PSI-PPy films made by Gizzie

et al. where the presence of PSI boosted performance in a film of Pani.[7] However, in that work, the film thickness reached a maximum of 250 nm and were grown directly on a TiO_2 anode compared to this investigation with films in excess of 1.5 µm and no semiconductor substrate. The current plateauing after 70 mC/cm^2 is consistent with the film appearance and thickness because the PPy appears to completely cover the active electrode surface at 70 mC/cm^2, and subsequent growth adds polymer well above the PSI layer, so it is not changing the performance of the film.

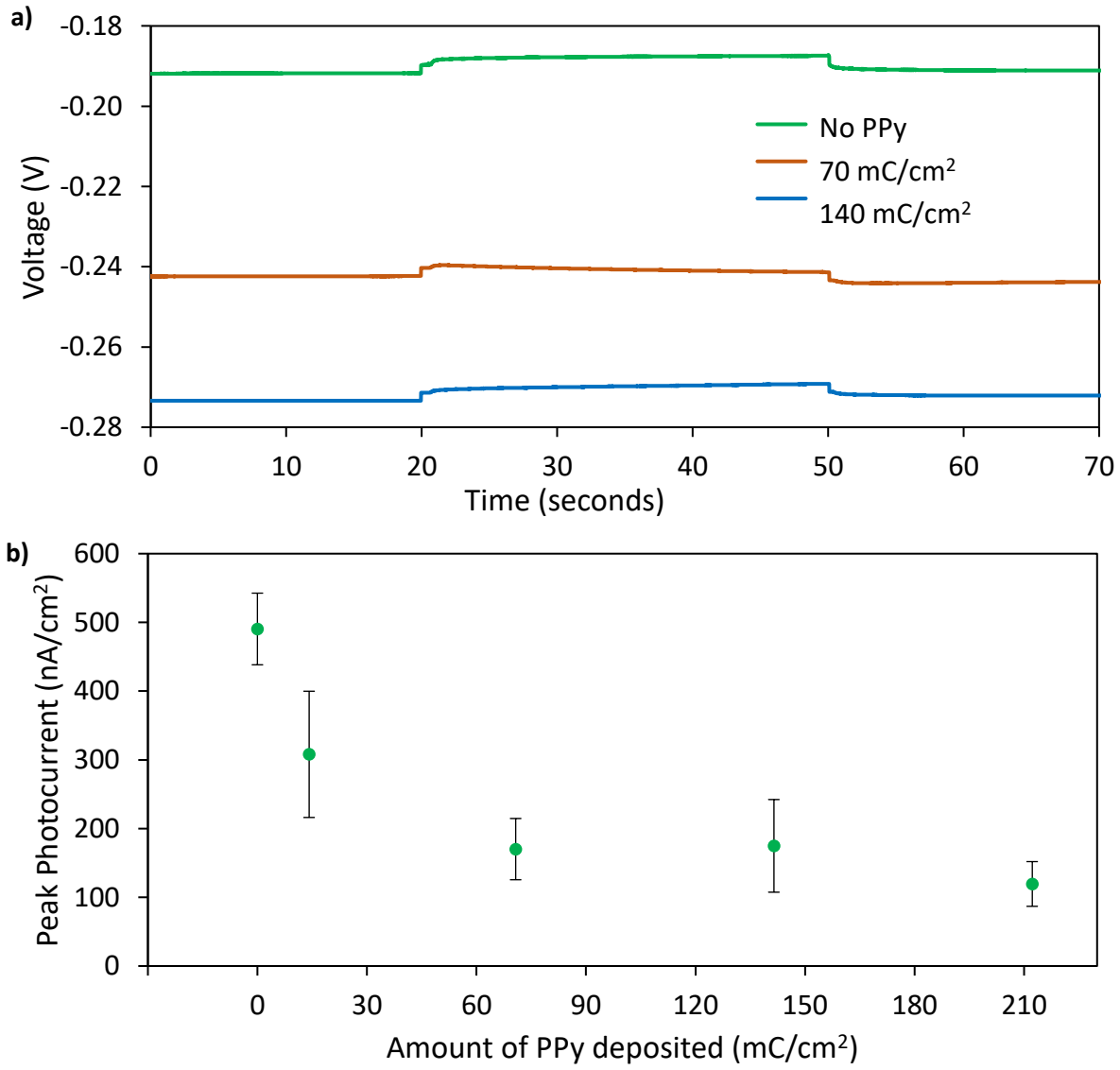

Figure 5.9: a) photovoltage measurements of PSI and PSI-PPy films in ferri/ferrocyanide solution. b) photocurrent measurements of PSI and PSI-PPy films in AscH/DCPIP mediator solution. All films were illuminated for 30 s.

Conclusions

PPy can be electropolymerized within the void spaces of a thick multilayer of PSI to generate a photoactive composite film that has a high contribution of protein in the polymer matrix. During electropolymerization, the PPy grows around PSI clusters and fills in the voids of the protein film before continuing to grow beyond the PSI film and increase the average thickness of the film. PSI is retained in the composite film during this growth process. The surface energy of the film shifts towards pure PPy after even a small extent of Ppy growth, suggesting that the PSI film was not raised during polymerization. The presence of a PSI multilayer does slow the polymerization rate of PPy due to the insulating nature of disconnected protein, but PPy was still able to grow through the voids in the protein film. The pseudocapacitance of PPy films increased as more polymer was deposited, but the capacitance was higher in the PSI-PPy films, indicating both a good connection between the polymer and electrode, even with the presence of a PSI multilayer, and higher interfacial area for the conducting polymer. The PSI-PPy films showed photo response in both potential and current, even with large amounts of the photo-inert polymer grown around the protein. A critical thickness of the polymer was found where continued polymerization would increase the film thickness, but the photocurrent response would remain the same. This work shows that PSI can be easily integrated into a Ppy matrix at high concentrations to produce a photoactive film with high interfacial area between protein and polymer. We believe that this approach can be used as a framework to produce biohybrid solid-state materials with high loadings of PSI.

References

1. Badura, A. *et al.* Photocurrent generation by photosystem 1 integrated in crosslinked redox hydrogels. *Energy Environ. Sci.* **4**, 2435–2440 (2011).

2. Robinson, M. T., Simons, C. E., Cliffel, D. E. & Jennings, G. K. Photocatalytic photosystem I/PEDOT composite films prepared by vapor-phase polymerization. *Nanoscale* 6158–6166 (2017). doi:10.1039/C7NR01158J

3. Gordiichuk, P. I. *et al.* Solid-state biophotovoltaic cells containing photosystem i. *Adv. Mater.* **26**, 4863–4869 (2014).

4. Kazemzadeh, S., Riazi, G. & Ajeian, R. Novel Approach of Biophotovoltaic Solid State Solar Cells Based on a Multilayer of PS1 Complexes as an Active Layer. *ACS Sustain. Chem. Eng.* **5**, 9836–9840 (2017).

5. Dervishogullari, D., Gizzie, E. A., Jennings, G. K. & Cliffel, D. E. Polyviologen as Electron Transport Material in Photosystem I-Based Biophotovoltaic Cells. *Langmuir* **34**, 15658–15664 (2018).

6. Gizzie, E. A., Leblanc, G., Jennings, G. K. & Cliffel, D. E. Electrochemical preparation of photosystem I-polyaniline composite films for biohybrid solar energy conversion. *ACS Appl. Mater. Interfaces* **7**, 9328–9335 (2015).

7. Gizzie, E. A. *et al.* Photosystem I-polyaniline/TiO_2 solid-state solar cells: simple devices for biohybrid solar energy conversion. *Energy Environ. Sci.* **8**, 3572–3576 (2015).

8. Wolfe, K. D. *et al.* Improving the Stability of Photosystem I-Based Bioelectrodes for Solar Energy Conversion. *Curr. Opin. Electrochem.* **19**, 27–34 (2019).

9. Robinson, M. T., Cliffel, D. E. & Jennings, G. K. An Electrochemical Reaction-Diffusion Model of the Photocatalytic Effect of Photosystem I Multilayer Films. *J. Phys. Chem. B* **122**, 117–125 (2018).

10. Sharma, P. S., Pietrzyk-Le, A., D'Souza, F. & Kutner, W. Electrochemically synthesized polymers in molecular imprinting for chemical sensing. *Anal. Bioanal. Chem.* **402**, 3177–

3204 (2012).

11. Chen, G., Hijazi, F. M., Leblanc, G., Jennings, G. K. & Cliffel, D. E. Scanning Electrochemical Microscopy of Multilayer Photosystem I Photoelectrochemistry. *ECS Electrochem. Lett.* **2**, H59–H62 (2013).

12. Ciesielski, P. N. *et al.* Enhanced Photocurrent Production by Photosystem I Multilayer Assemblies. *Adv. Funct. Mater.* **20**, 4048–4054 (2010).

13. Teh, K. S., Takahashi, Y., Yao, Z. & Lu, Y. W. Influence of redox-induced restructuring of polypyrrole on its surface morphology and wettability. *Sensors Actuators, A Phys.* **155**, 113–119 (2009).

14. Xu, L., Chen, W., Mulchandani, A. & Yan, Y. Reversible conversion of conducting polymer films from superhydrophobic to superhydrophilic. *Angew. Chemie - Int. Ed.* **44**, 6009–6012 (2005).

15. Fleischmann, S. *et al.* Pseudocapacitance: From Fundamental Understanding to High Power Energy Storage Materials. *Chem. Rev.* **120**, 6738–6782 (2020).

16. Amdursky, N. *et al.* Electronic Transport via Proteins. *Adv. Mater.* **26**, 7142–7161 (2014).

17. Yang, S., Robinson, M. T., Mwambutsa, F., Cliffel, D. E. & Jennings, G. K. Effect of Cross-linking on the Performance and Stability of Photocatalytic Photosystem I Films. *Electrochim. Acta* **222**, 926–932 (2016).

18. G. Street, T. Clarke, R. Geiss, V. Lee, A. Nazzal, P. P. & Uger, J. S. Characterization of Polypyrrole. *J. Phys. Colloq.* **44**, 9 (1983).

19. Robinson, M. T., Armbruster, M. E., Gargye, A., Cliffel, D. E. & Jennings, G. K. Photosystem I Multilayer Films for Photovoltage Enhancement in Natural Dye-Sensitized Solar Cells. *ACS Appl. Energy Mater.* **1**, 301–305 (2018).

Chapter 6

Conclusions and Outlook

Summary

In this dissertation, multiple investigations targeting specific reaction centers of the Photosystem I (PSI) protein complex were performed. Historically, PSI has been used and analyzed in three-electrode electrochemical cells to study the electrochemical capabilities of the protein, typically through mediated electron transfer (MET). One of the primary goals of the work contained in this dissertation is to find ways to improve the performance and utilization of PSI for more applied systems, such as gel-base two-electrode photovoltaic devices, solid-state devices, and the production of value-added materials.

In Chapter 3, the fabrication of a natural, PSI-integrated, dye-sensitized solar cell device was explored. PSI has robust redox capabilities between the F_B and P_{700} reaction sites. In this chapter, the mediator-based asymmetry of the redox reactions was targeted to show that careful selection of mediators can be used to improve performance of PSI based on its position in an electrochemical cell. The mediator couple, ascorbic acid:2,6-dichlorophenolindophenol (AscH:DCPIP), was used to generate an excess of oxidized species near the cathode of a two-electrode photovoltaic device because the oxidation of reduced DCPIP by the P700 reaction center is much faster than the reduction of oxidized mediator species at the F_B site of PSI. The cathode served as the limiting electrode compared to the blackberry anthocyanin based dye-sensitized TiO_2 anode. Other mediators that have reduction potentials more favorable for the generation of excess reduced species by PSI were shown to provide negligible or significantly less photocurrent production in this arrangement of the PSI film on the cathode. Previously, placement of a PSI film

on a dye-sensitized TiO_2 anode was shown to boost photovoltage production by using one of the mediator systems that is more easily reduced by PSI.[1]

The device used a gel-based electrolyte to allow facile fabrication of a two-electrode system that has advantages compared to liquid-based cells while still being able to operate via MET. The two-electrode setup allowed solar conversion efficiencies to be measured for the devices. Simple addition of a PSI multilayer was shown to provide a 50% performance increase over devices without the protein, producing one of the best performing PSI-integrated two-electrode systems to date. Additionally, an electrochemical reaction-diffusion numerical model was developed to determine kinetic capabilities of PSI in the two-electrode system. The empirical data was used to calculate a reaction rate coefficient for PSI in the AscH:DCPIP mediator system.

In Chapter 4, the ability of PSI to perform oxidative polymerizations was successfully proven by showing that unmodified PSI can form protein-polymer conjugates by mixing protein and the monomer, pyrrole (Py), under illumination to generate polypyrrole (PPy). The polymerization of Py to form PPy by PSI is one of the first known reports of an unmodified protein that is able to grow a chemically connected conducting polymer. This reaction targeted the oxidative capabilities of the P_{700} reaction site, which has been far less examined as compared to the robust reductive capabilities of the F_B reaction site. The protein-polymer conjugates were shown to be photoactive and yield photocurrents and photovoltages of the same magnitude as pure PSI, but with opposite direction. While PSI produces positive photovoltage and cathodic current, the PSI-PPy conjugates produced negative photovoltage and anodic current of similar magnitude. This change indicates that the addition of the PPy is altering the redox properties of the protein so that more reduced species are being formed than unmodified PSI, changing the ratio of oxidized to reduced species within the protein-polymer conjugate films. The similar magnitude also

indicates that the protein retains its robust redox abilities. Additionally, the conjugates were shown to be conductive and photoactive when dried into a powder form. A photoactive and conductive powder is consistent with conjugation occurring directly at the P_{700} site on the PSI, because the powder can only be photoactive in a solid-state form if there is direct connection between the polymer and protein. This is the first report of PSI being able to successfully polymerize a conducting polymer. The reaction also forms a protein-polymer conjugate, and the resulting conjugate is shown to be photoactive in both solid and liquid solar conversion cells.

In Chapter 5, PPy was electrochemically polymerized around a multilayer film of PSI to create a photoactive and conductive polymer matrix. Growing polymer through a multilayer film allowed for the incorporation of more protein dispersed throughout the polymer film than previous generations of PSI-polymer systems.[2–4] Growing the polymer through a protein film also increases the probability of direct connection to the active sites of PSI because the polymer was shown to fill in voids of the protein film during the polymerization. These conclusions are supported by multiple experiments investigating physical and electrochemical properties of the films. Polymer growth was examined through profilometry and contact angle measurements to measure properties of the films. The presence of PPy in all films led to a decrease in contact angle, suggesting that the PPy can affect properties even in small amounts. The open-circuit potential of the film decreased as the amount of polymer increased, while still producing photovoltage. The photocurrent produced decreased as the amount of polymer increased, but the photocurrent remained constant after 70 mC/cm^2 was formed. The PPy films that were grown through PSI also showed significantly higher pseudocapacitance than pure PPy films, indicating that there is still good connection between the polymer and electrode. This research can act as the groundwork for developing biohybrid solid-state materials with high PSI loadings

Outlook

The work detailed in this dissertation shows emerging technology and methods to ultimately make the use of photosynthetic proteins a commercially viable alternative in the field of solar energy conversion. PSI is a naturally occurring and abundant material that has nearly perfect internal quantum efficiency and vast quantities of proteins can be easily extracted for use in any number of applications. Kelvin probe force microscopy studies have shown that micrometer-thick, crystalline PSI layers could produce a photovoltage of nearly 50 V under 1 W/cm^2 of illumination, signaling that there is room for massive improvement of PSI utilization.[5]

The protein has been shown to function for at least 280 days with similar performance in a liquid electrochemical and can likely continue performing for even longer.[6] Stability is expected to increase even further if the protein is used in solid-state applications because there is no reactive oxygen species to degrade the protein.[7] Exploring targeted reactions to improve the performance of PSI in solar energy harvesting systems facilitates the innovation of more biohybrid technologies by finding ways to maximize performance.

The biohybrid dye-sensitized solar cell in Chapter 3 shows that PSI can be used to significantly boost the performance of a functional photovoltaic device and that these devices can be connected to produce even higher voltages. The materials used in the solar cell are natural, inexpensive, environmentally friendly, and abundant. The design can further be optimized in many ways to further decrease the environmental and economic cost per watt of energy and make PSI a stronger candidate for commercial viability. Optimizations include discovering more suitable electrode materials, reversible redox mediators, or combinations of multiple mediators that energetically align with PSI better than what was used in this work. Additionally, with the use of

a mixed mediator system that targets both reaction centers, PSI could be placed on both an anode and a cathode to simultaneously increase performance of both electrodes.

The numerical model developed in this work provides the basis for an even more advanced model that can predict performance with other mediators and electrodes to find the optimal conditions and materials for a gel-based device. Investigating other mediator systems in this gel cell could ultimately lead to finding a relationship between mediator reduction potential and its reaction rate constant with PSI, which can be used to determine electrochemical properties of synthetic redox molecules to maximize performance with PSI in an electrochemical cell.

The novel method to use PSI to polymerize conducting materials and make conductive protein-polymer conjugates presented in Chapter 4 opens the door to design and produce a wide range of PSI-integrated materials for high impact work. This research expands the applications for photosynthetic proteins to include inexpensive and facile production of value-added polymers and could lead to the creation of an entirely new class of protein-polymer conjugates. The PSI-PPy conjugates formed in this study were shown to be active both in liquid and solid-states systems, further increasing the potential applications. Additionally, the direct connection to the active sites of PSI with a conducting polymer could allow for higher potentials to be produced in solid-state systems. Many other polymers that are formed through oxidative polymerization can be investigated to yield protein-polymer conjugates with a wide range of properties for different applications such as supercapacitors, solid-state solar cells, bio-electrodes, and more. Connecting polymers to proteins has been shown to provide an increase in stability for proteins. Photosystem II (PSII) is a less stable protein than PSI, limiting its use in some electrochemical systems.[8] The technique detailed in this chapter could be applied to PSII to form protein-polymer conjugate systems, which would increase protein stability. PSII has a reduction potential 0.8 V higher than

PSI at its oxidizing reaction site, so being able to use PSII would increase the range monomer candidates to be polymerized via oxidative polymerization.[9]

In Chapter 5, I present a method to increase the amount of electrically connected PSI proteins inside of a conducting polymer matrix to produce a highly functioning solid-state electrolyte or bioelectrode. This technique is another approach to directly connect conducting polymer to the P_{700} reaction site to close in on extracting the full 1.1 V of potential that PSI can achieve. Finding a method that maximizes the number of available proteins in a conducting matrix can dramatically increase the viability of PSI solid-state systems. The work in this chapter shows that conducting polymer can be easily grown around a multilayer of PSI without destroying the protein or suppressing its photo-capabilities, but more investigation is needed to determine how much of the protein film is in direct connection with the polymer. There is potential to produce protein-polymer conjugates via the method presented in Chapter 4 to create a molecular wire that is directly connected to the P_{700} reaction site and protrudes from the protein. If a multilayer of the conjugates is deposited and conducting polymer is grown around it, then there would be a much higher likelihood of connecting the protein with the conducting polymer matrix because of the connection points being available outside of the lumenal pocket.

Conclusion

PSI is a protein that is vital for the process of photosynthesis, which powers our natural world. Annually, green vegetation is converting five times more energy from the sun than humans consume globally. Finding ways to utilize the abundant and renewable resource found in virtually every corner of the globe can help solve the current energy crisis the world is facing. PSI has been proven to be an exceptional candidate for inexpensive and powerful solar energy conversion technologies, but more knowledge is still needed to maximize its potential.

In this dissertation, different methods are presented that target specific electrochemical reactions to improve PSI performance in biohybrid applications. We have shown that PSI can be integrated with other materials easily found in nature to generate inexpensive and renewable solar energy, and we developed a method to help improve materials selection to produce even more energy. A novel ability of PSI has been presented and shows that PSI can produce a unique class of protein-polymer conjugates. We also present progress towards successfully incorporating PSI in a conducting solid-state system. As more research is done utilizing PSI, the resulting biohybrid technologies and techniques continue to become more efficient while remaining low cost and environmentally friendly. In the future, there is an increasing possibility that someone will be able to grow their own sources of PSI, extract the protein, and then use it to generate their own green energy.

References

1. Robinson, M. T., Armbruster, M. E., Gargye, A., Cliffel, D. E. & Jennings, G. K. Photosystem I Multilayer Films for Photovoltage Enhancement in Natural Dye-Sensitized Solar Cells. *ACS Appl. Energy Mater.* **1**, 301–305 (2018).

2. Robinson, M. T., Simons, C. E., Cliffel, D. E. & Jennings, G. K. Photocatalytic photosystem I/PEDOT composite films prepared by vapor-phase polymerization. *Nanoscale* 6158–6166 (2017). doi:10.1039/C7NR01158J

3. Gizzie, E. A., Leblanc, G., Jennings, G. K. & Cliffel, D. E. Electrochemical preparation of photosystem I-polyaniline composite films for biohybrid solar energy conversion. *ACS Appl. Mater. Interfaces* **7**, 9328–9335 (2015).

4. Badura, A. *et al.* Photocurrent generation by photosystem 1 integrated in crosslinked redox hydrogels. *Energy Environ. Sci.* **4**, 2435–2440 (2011).

5. Toporik, H. *et al.* Large photovoltages generated by plant photosystem I crystals. *Adv. Mater.* **24**, 2988–2991 (2012).

6. Ciesielski, P. N. *et al.* Photosystem I-Based biohybrid photoelectrochemical cells. *Bioresour. Technol.* **101**, 3047–3053 (2010).

7. Wolfe, K. D. *et al.* Improving the Stability of Photosystem I-Based Bioelectrodes for Solar Energy Conversion. *Curr. Opin. Electrochem.* **19**, 27–34 (2019).

8. Yamamoto, Y. Quality control of photosystem II. *Plant Cell Physiol.* **42**, 121–128 (2001).

9. Wright, T. A., Page, R. C. & Konkolewicz, D. Polymer conjugation of proteins as a synthetic post-translational modification to impact their stability and activity. *Polym. Chem.* **10**, 434–454 (2019).

APPENDIX A

Photoreduction of Metal Nanoparticles on Photosystem I Active Sites

In previous work from our group as well as the work of others, the high reducing potential of the F_B reaction site has been used to electrochemically deposit Pt nanoparticles on the surface of PSI, and the resulting conjugates were then used for photocatalytic H_2 evolution.[1–4] PSI has also been platinized and used to create oriented multilayers of PSI where photovoltage improved with each additional layer.[5] In addition to direct photoreduction, Au and Pt nanoparticles have been connected to the F_B site of PSI through molecular wiring of the protein to the nanoparticle.[6] PSI is able to reduce both Pt II and Pt IV salts onto the F_B site, showing that the reduction is not limited to singly charged ions.

Platinization of PSI has been thoroughly examined, but the ability to photoreduce other metals on PSI has been unexplored. Many metals have reduction potentials that are favorably aligned and can be reduced by the F_B reaction center. Metallic nanoparticle-PSI conjugates should retain photoactivity and be available to catalyze other reactions beyond H_2 evolution, such as the potential reduction of CO_2 by Cu or Sn nanoparticles. Additionally, if successful, dual modification of PSI proteins can be performed by reducing a metal on one end of the protein and growing polymer on the other end using the technique described in Chapter 4.

The overall goal of this project is to successfully photoreduce metal nanoparticles other than Pt and use the resulting metallized PSI to catalyze a new reaction. Cu and Sn are examined because they are energetically aligned with F_B and are used to catalyze many reactions. Additionally, the reduction of CO_2 can occur in both adsorbed and non-adsorbed reactions with Cu and Sn catalysts, respectively.

After confirmation of the presence of a nanoparticle on the F_B site, the nanoparticle-protein conjugates will be used to reduce aqueous CO_2. Sn and Cu both are able to selectively catalyze the reduction of CO_2 to formate and methane, respectively.[7] Sn nanoparticles have been shown to reduce CO_2 to formate at overpotentials as low as 340 mV, within the range of PSI reduction potentials.[8] To test catalytic ability, multilayers of the conjugates will be deposited on a gold electrode in an aqueous solution of $NaHCO_3$ and AscH (as an electron donor). The films will be illuminated and photocurrent response will be measured to see if the reduction reaction is being catalyzed by the nanoparticles. An unmodified PSI film will be tested in parallel as a control.

Sn II and Cu II chlorides were the first salts explored in this investigation. To reduce the metals, PSI was mixed with either $SnCl_2$ or $CuCl_2$ in an aqueous solution with an excess of sodium ascorbate to donate electrons to PSI. The solution was then stirred for 24 h, and light was pulsed on and off every 2 h to help the reduction reaction proceed. EDS was performed to try and identify if metal had been deposited on a protein film. However, the energy of the beam required destroyed the protein, and the metal nanoparticles were too small to be reliably measured.

Photochronoamperometry was also used to determine if the metals were successfully deposited. If deposition was successful, a change in photocurrent could occur by either blocking electron transfer at the F_B site to lower photocurrent, or by providing more active, conductive area to increase photocurrent. Figure A.1 shows the PCA results of a three-electrode setup where PSI films were vacuum deposited on a gold substrate with a ferri/ferrocyanide mediator, a Pt counter electrode, and Ag/AgCl reference. The samples were illuminated between 20 and 50 s. The initial results show that the metallized samples had almost no photocurrent compared to the PSI-only control. The results suggest that the metals have changed the photoactivity of the protein, suggesting some type of modification. The large photocurrent spike for the PSI-Sn sample when

the light is turned on and off is unexpected considering there is no photocurrent under illumination except for the spikes. This phenomenon needs to be explored more because it could lead to insights on how electrons are transferred to and stored by the nanoparticle-PSI conjugate.

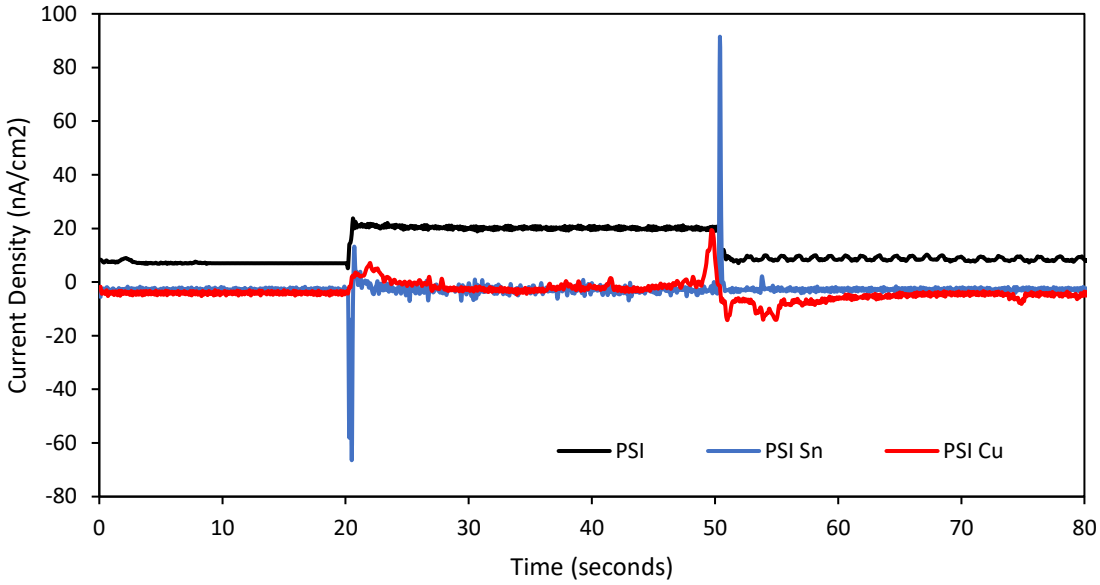

Figure A.1: Photochronoamperometry experiments of PSI films from samples that were reacted with metal salts for 24 h in 1 mM ferri/ferrocyanide solution with 0.1 M KCl as supporting electrolyte.

UV-Vis was also used to investigate if metals were connected to the proteins. After mixing with the metal salts and pulsing with light for 24 h, samples were dialyzed overnight in 4 L of water, and then the solution was measured in the tool. The results are shown in Figure A.2. In all t samples, peaks at 433 and 680 nm appear, which are indicative of the PSI chlorophylls. Sn oxide nanoparticles have been shown to have a strong absorbance at 300 nm and below, agreeing with the sharp rise in absorbance seen at 300 nm from the UV-Vis.[9] Cu oxide particles have been shown to exhibit a broad absorption peak at 285 nm that is similar to the increase in absorption seen in the spectra below.[10] The current work shows promising evidence that metals other than Pt were successfully conjugated with PSI, but more work needs to be done to prove that the metals are combined and that they can be used to photocatalyze desired reactions.

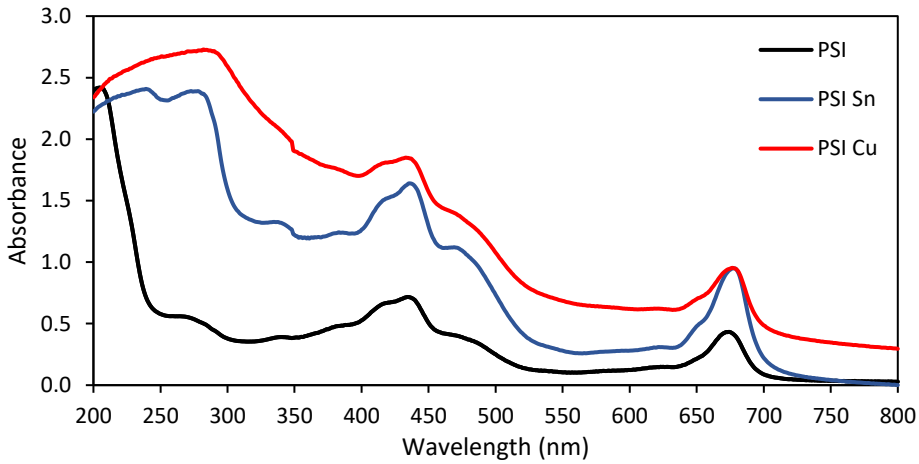

Figure A.2: UV-Vis spectra of dialyzed PSI samples that were reacted with metal salts for 24 h.

Reducing metal nanoparticles on the F_B site can allow PSI to be used to help catalyze many electrochemical reactions. Pt particles have been reduced on PSI in previous work with the goal of H_2 production. Exploring the ability to reduce other metal nanoparticles can potentially allow PSI to catalyze other desired reactions such as the reduction of CO_2 or the formation of commercially desired materials. Similar to conducting polymer polymerization, if metal nanoparticles can be reduced, and if catalyzed reactions can occur simply from shining light on the protein, this greatly reduces the cost and equipment needed to perform the desired reactions.

References

1. Platinized Chloroplasts : A Novel Photocatalytic Material. *Science (80-.).* **230**, 1373–1375 (1985).
2. Leblanc, G., Chen, G., Jennings, G. K. & Cliffel, D. E. Photoreduction of catalytic platinum particles using immobilized multilayers of Photosystem I. *Langmuir* **28**, 7952–7956 (2012).
3. Lubner, C. E., Grimme, R., Bryant, D. A. & Golbeck, J. H. Wiring photosystem I for direct solar hydrogen production. *Biochemistry* **49**, 404–414 (2010).
4. Lee, J. W., Lee, I. & Greenbaum, E. Platinization: A novel technique to anchor photosystem I reaction centres onto a metal surface at biological temperature and pH. *Biosens. Bioelectron.* **11**, 375–387 (1996).
5. Frolov, L., Wilner, O., Carmeli, C. & Carmeli, I. Fabrication of oriented multilayers of photosystem I proteins on solid surfaces by auto-metallization. *Adv. Mater.* **20**, 263–266 (2008).

6. Grimme, R., Lubner, C., Bryant, D. & Golbeck, J. Photosystem I/molecular wire/metal nanoparticle bioconjugates for the photocatalytic production of H2. *Chemtracts* **21**, 207–209 (2008).

7. Hori, Y. Electrochemical CO2 Reduction on Metal Electrodes. in *Modern Aspects of Electrochemistry* 89–189 (Springer New York, 2008). doi:10.1007/978-0-387-49489-0_3

8. Zhang, S., Kang, P. & Meyer, T. J. Nanostructured Tin Catalysts for Selective Electrochemical Reduction of Carbon Dioxide to Formate. *J. Am. Chem. Soc.* **136**, 1734–1737 (2014).

9. Mayandi, J., Marikkannan, M., Ragavendran, V. & Jayabal, P. Hydrothermally Synthesized Sb and Zn Doped Sno 2 Nanoparticles. **2**, 707–710 (2014).

10. Yugandhar, P., Vasavi, T., Uma Maheswari Devi, P. & Savithramma, N. Bioinspired green synthesis of copper oxide nanoparticles from Syzygium alternifolium (Wt.) Walp: characterization and evaluation of its synergistic antimicrobial and anticancer activity. *Appl. Nanosci.* **7**, 417–427 (2017).

APPENDIX B

Electrochemical Investigation of the AscH/DCPIP Mediator Couple

The use of the AscH/DCPIP mediator couple has become widespread both in investigating photosynthetic processes[1–4] and in the determination of the amount of vitamin C and other reductants found in commercial products.[5,6] The redox couple has the potential to be a widely used electrochemical mediator because of its low toxicity and cost, motivating its use in the previous gel-cell studies.

When ascorbate and DCPIP are dissolved in an aqueous solution, there are many different molecular transformations dependent on pH that can affect both the chemical and electrochemical reactivity.[7] Figure 7 shows the known forms, showing the expected reactants for the successful two proton and two electron reaction for DCPIP to $DCPIPH_2$.

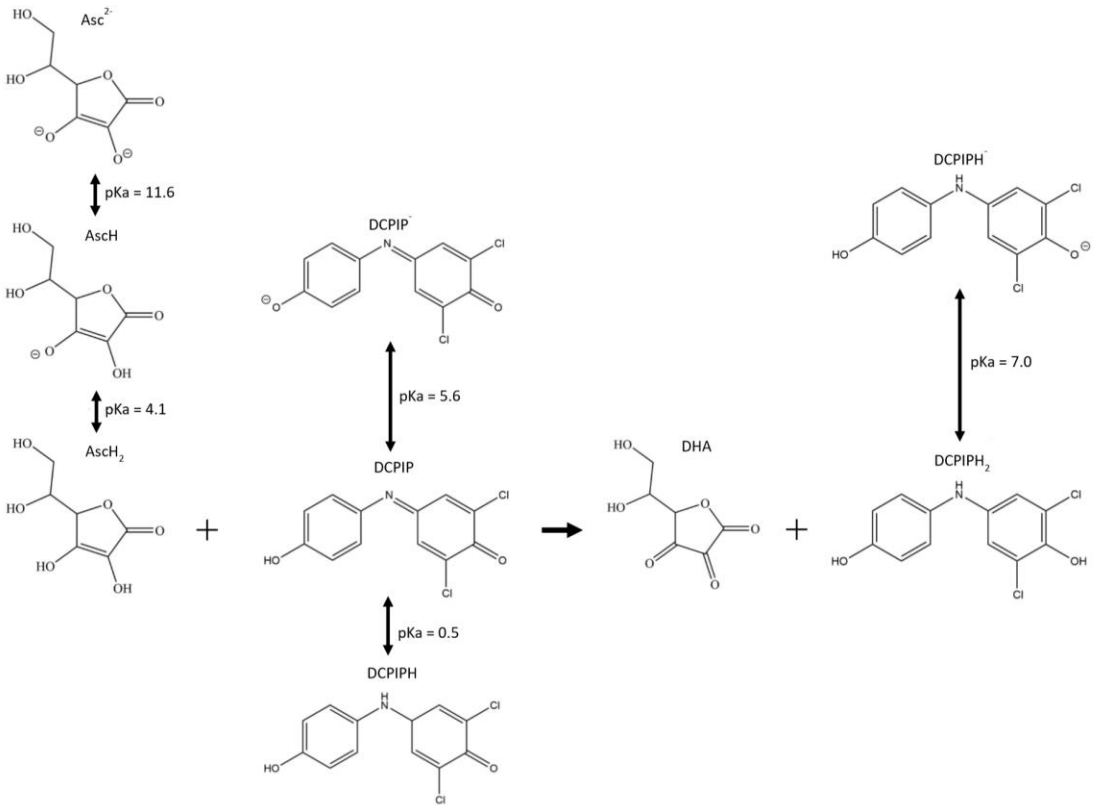

Figure B.1: Forms and reaction of ascorbate with DCPIP and corresponding pKa's.

The chemically reactive species are ascorbic acid ($AscH_2$) reacting with DCPIP to form dehydroascorbic acid (DHA) and $DCPIPH_2$. Using the Henderson-Hasselbach equation, mol fractions at any pH can be approximated for all of the forms of AscH and DCPIP shown in Figure B.2. There are claims that DCPIP can be reduced with AscH at a pH of 8.5, but based on literature values for pKa's, neither DCPIP or ascorbic acid would be present.[8] According to Karayannis, there is no reaction beyond a pH of 7 for an ascorbate/DCPIP mixture, but the rate constant of the reaction greatly increases at pH 4 and lower.[9] Others have examined the reaction at or near neutral pH's ranging from 6.5-7.0.[1,5]

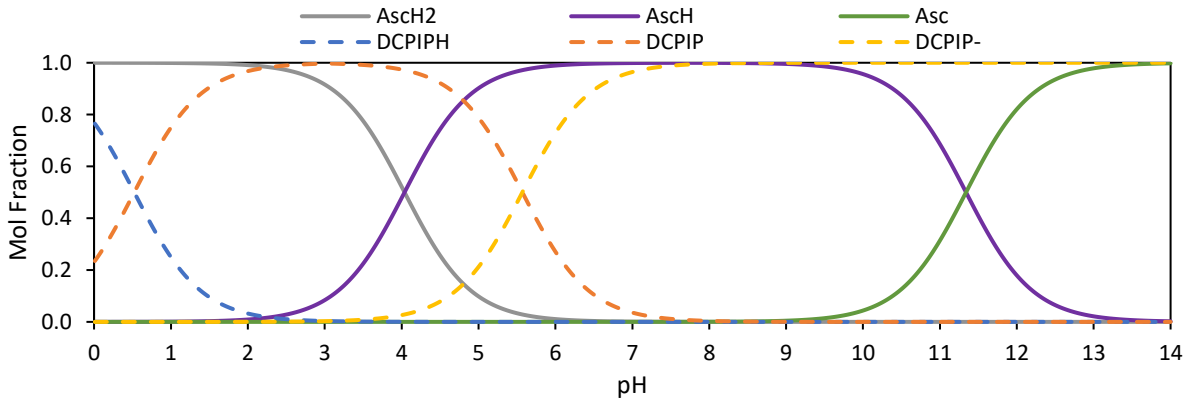

Figure B.2: Mol fraction of different forms of ascorbate and DCPIP based on pH.

In all of these cases, only the homogeneous kinetics of the AscH/DCPIP reaction are considered, neglecting the electrochemical reactions that these chemicals are mainly used for. $DCPIPH_2$ is known to be electrochemically active, but there is no clarity for what $DCPIPH_2$ can be reduced to. Currently, there is no strong understanding as to which forms of ascorbate and DCPIP are electrochemically active. Formal potentials are reported for both DCPIP (0.217 V)[10] and ascorbic acid (0.40 V),[11] but the other forms also might be electrochemically active at other potentials and need to be explored further. Ascorbic acid is considered to be a sacrificial electron donor[12], but some work suggests that there is a reversible pathway to regenerate the reduced form.[2]

Trubitsin *et al.* have proposed a complex interaction of the ascorbate and DCPIP with the PSI. However, their results are based solely on EPR measurements made in pH 8.0 buffered solutions, which raises questions as to the accuracy of the model presented because of the species that should be present. With all of the inconsistencies in the AscH/DCPIP literature and a lack of thorough electrochemical studies of the reaction, we aim to carry out a methodical investigation of the electrochemical properties of the mediator couple with a secondary goal of being able to more deeply understand the reactions relevant with PSI. Currently, $DCPIPH_2$ is accepted to be a good electron donor to P_{700}, but the dominant reactant at the F_B site is currently unknown.

The main goal of this project is to obtain better understanding of the electrochemical properties of the AscH/DCPIP mediator couple. Determining what species are electrochemically active can provide more accurate electrochemical measurement results. Additionally, we hope to be able to determine which species is the electron acceptor from the F_B site because there are currently conflicting opinions.

To reach these goals, we plan to perform multiple studies on AscH and $DCPIPH_2$ using CV. The reaction rate for the oxidized form of $DCPIPH_2$ with ascorbate can be determined using CV at high scan rates to determine reaction kinetics. AscH is typically added in excess to reduce all of the DCPIP but testing a solutions with different molar ratios of DCPIP to AscH should reveal if DCPIP and $DCPIPH_2$ can have separate redox reactions in the same solution. From the CV experiments, the formal potentials for all of the different forms can be found, and we can then determine which reactions most energetically align with PSI. NMR can also be used to determine different forms that are present at various conditions before and after chemical and electrochemical reactions. Testing if AscH is truly a sacrificial donor, long reversibility studies using CV can be performed to examine reversibility over time. A more involved study of the pH effects on the

performance of the AscH/DCPIP mediator couple and their reactivity are explored in more detail in Chapter 3.

Working in collaboration with Kody Wolfe in the Interdisciplinary Materials Science Program, CV scans of the AscH/DCPIP reaction were done at scan rates ranging from 100 mV/s to 1,300 mV/s and showed the expected EC' catalytic reaction CV shape where the oxidation peak is larger than the reduction peak (Figure B.3). As the scan rate increases, the reduction peak grows relative to the oxidation peak because the increased scan rate allows less time for the chemical reduction of DCPIP by AscH to occur, leaving more reducible species. Eventually, at a high enough scan rate the chemical reaction should not have enough time to occur and thus, the kinetic reaction rate for the AscH/DCPIP reaction can be measured.

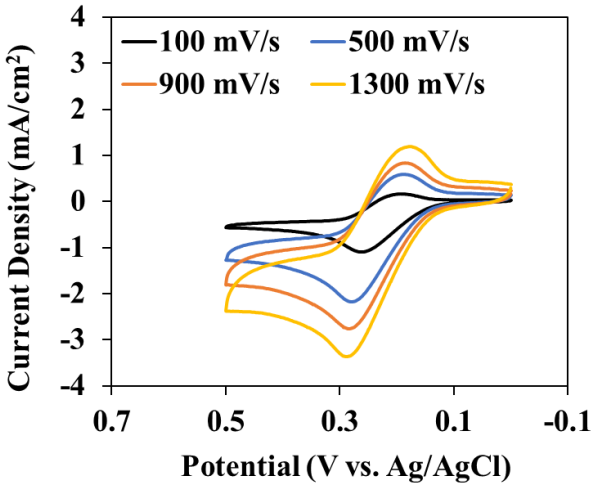

Figure B.3: CV scans of the EC' catalyzed reaction of AscH and DCPIP. Image by Kody Wolfe.

Multiple CV experiments were carried out to determine some of the reactions that occur between AscH and DCPIP under different conditions and potential windows and are shown in Figure B.4. In these 4 CV experiments, 7 unique peaks appear in the voltammograms, showing how complex the reactions between the two redox species can be.

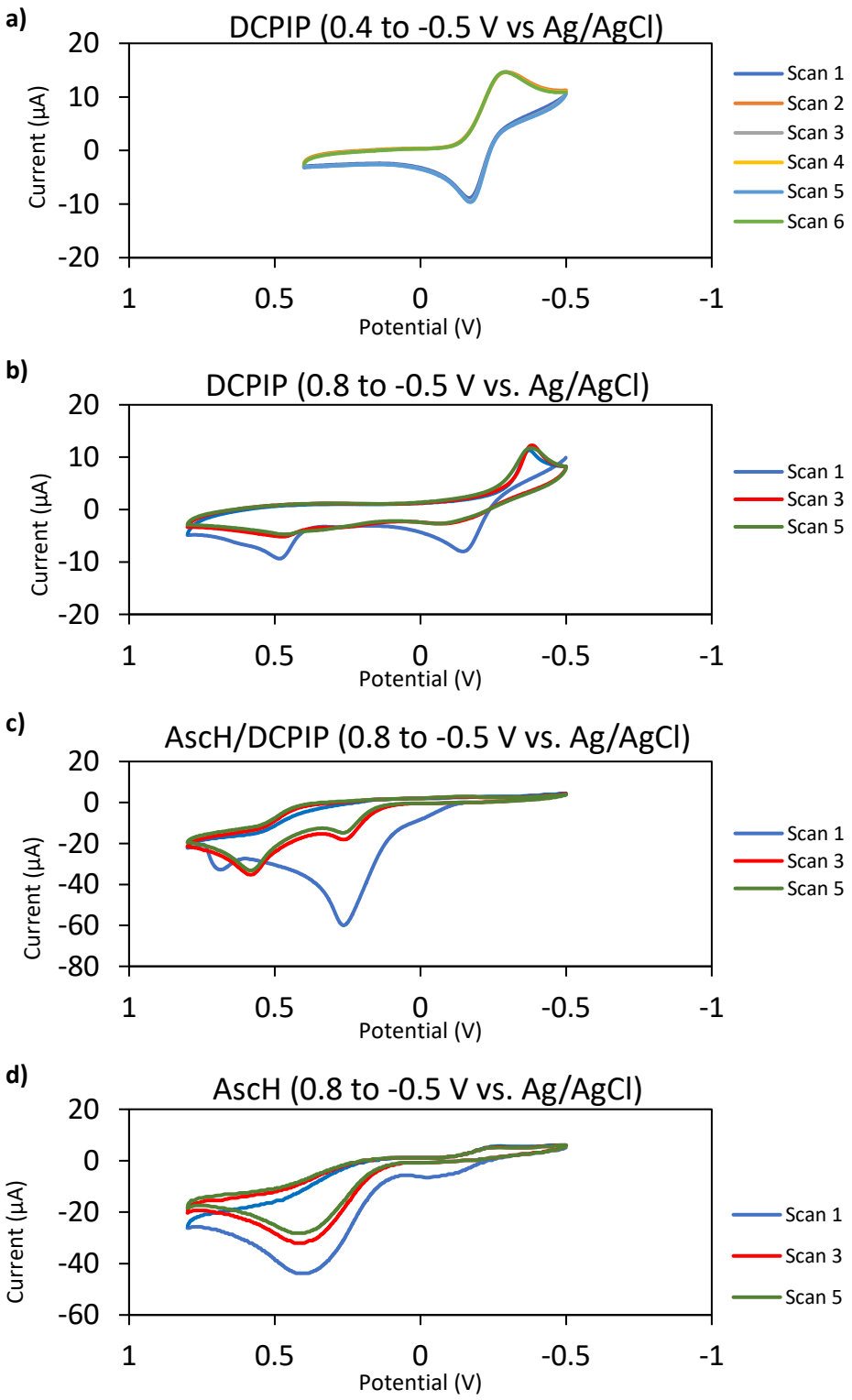

Figure B.4: CV scans of AscH/DCPIP mediators under different conditions: a) DCPIP from 0.4 to -0.5 V, b) DCPIP from 0.8 to -0.5 V, c) AscH/DCPIP from 0.8 to -0.5 V, and d) AscH from 0.8 to -0.5 V.

The use of the AscH/DCPIP couple is widely used in photosynthesis research. A large portion of this research is used to determine kinetic parameters of photosynthetic processes, but in electrochemical applications, reactive mediator concentration is needed to extract kinetic information. This work will help to provide more detailed information of what reactive species are in these systems. Additionally, many investigators report that AscH is a sacrificial electron donor, but if evidence is shown that it can be reduced in an electrochemical cell, it can promote the use of this non-toxic mediator in electrochemical cells.

References

1. Vernon, L. P. & Zaugg, W. S. Photoreductions by fresh and aged chloropasts: requirement for ascorbate and 2, 6-dichlorophenolindophenol with aged chloroplasts. *J. Biol. Chem.* **235**, 2728–2733 (1960).
2. Trubitsin, B. V., Mamedov, M. D., Semenov, A. Y. & Tikhonov, A. N. Interaction of ascorbate with photosystem i. *Photosynth. Res.* **122**, 215–231 (2014).
3. Vernon, L. P. & Shaw, E. R. Photoreduction of 2,6-Dichlorophenolindophenol by Diphenylcarbazide: A Photosystem 2 Reaction Catalyzed by Tris-Washed Chloroplasts and Subchloroplast Fragments. *Plant Physiol.* **44**, 1645–1649 (1969).
4. Yang, X. *et al.* pH dependence of photosynthetic behavior of plant photosystem I particles. *Russ. J. Plant Physiol.* **56**, 599–606 (2009).
5. Florou, A. B., Prodromidis, M. I., Karayannis, M. I. & Tzouwara-Karayanni, S. M. Flow electrochemical determination of ascorbic acid in real samples using a glassy carbon electrode modified with a cellulose acetate film bearing 2,6-dichlorophenolindophenol. *Anal. Chim. Acta* **409**, 113–121 (2000).
6. Davies, S. H. R. & Masten, S. J. Spectrophotometric method for ascorbic acid using dichlorophenolindophenol: elimination of the interference due to iron. *Anal. Chim. Acta* **248**, 225–227 (1991).
7. Tonomura, B., Nakatani, H., Ohnishi, M., Yamaguchi-Ito, J. & Hiromi, K. Test reactions for a stopped-flow apparatus. Reduction of 2,6-dichlorophenolindophenol and potassium ferricyanide by L-ascorbic acid. *Anal. Biochem.* **84**, 370–383 (1978).
8. Prigodich, R. V. A stopped-flow kinetics experiment for the physical chemistry laboratory using noncorrosive reagents. *J. Chem. Educ.* **91**, 2200–2202 (2014).
9. Karayannis, M. I. Comparative kinetic study for rate constant determination of the reaction of ascorbic acid with 2,6-dichlorophenolindophenol. *Talanta* **23**, 27–30 (1976).
10. Kumar, S. & Acharya, S. K. 2,6-Dichloro-phenol indophenol prevents switch-over of

electrons between the cyanide-sensitive and -insensitive pathway of the mitochondrial electron transport chain in the presence of inhibitors. *Anal. Biochem.* **268**, 89–93 (1999).

11. Creutz, C. The Complexities of Ascorbate as a Reducing Agent. *Inorg. Chem.* **20**, 4449–4452 (1981).

12. Pellegrin, Y. & Odobel, F. Sacrificial electron donor reagents for solar fuel production. *Comptes Rendus Chim.* **20**, 283–295 (2017).

APPENDIX C

MATLAB Code Used for Reaction-Diffusion Model in Gel Devices

The model uses three separate scripts (leastsquares.m, GelPDE_NoPSI.m and GelPDE_PSI.m) to determine the values for the initial ratio of oxidized to reduced species in solution (C_o/C_R) and the reaction rate constant for PSI (kPSI). The leastsquares script uses the *lsqcurvefit* command to provide an initial guess for C_o/C_R in the GelPDE_NoPSI function to get the ratio for a device without PSI, and then the *lsqcurvefit* command is used again to determine the kPSI, using the newly found C_o/C_R, in the GelPDE_PSI function. The normalized currents are also calculated to compare the calculated values to experimental values. The code for all three scripts is provided below.

leastsquares.m

```
global x0
%lsqcurvefit(FUN,X0,XDATA,YDATA,LB,UB)
%XDATA is concentration
%YDATA is normalized current

%solve for x0 which is O/R ratio from no PSI case
x0 = lsqcurvefit(@GelPDE_NoPSI,[0.001],[1,4,20,120,200],[.1356,.478,.8367,.9788,1],[.000001],[.1])

%solve for kPSI using new x0 data
kPSI =
lsqcurvefit(@GelPDE_PSI,[0.001],[1,4,20,120,200],[.185,.7116,.984,1.0703,1.1554],[0.000001],[1000])


x0 =

   1.0796e-04


kPSI =

   2.0276e-05
```

GelPDE_NoPSI.m

```
function [iNo] = GelPDE_NoPSI(A0,xdata)
global D Co_in Ctot n current i0 kT_q B Ecopp EDCPIP Asc Conc Dasc
x1 = linspace(0,4,1500); %PSI film thickness in um
x2 = linspace(4.1,400,250); %bulk electrolyte thickness in um
x = [x1 x2];
tmesh = 4000;
t = linspace(0,30,tmesh);
time = round(linspace(0,tmesh,10)); %create 4000 time points from 0-30s for plotting
m = 0; %pdepe parameter

D = 0.27e-9*1e12; %um2/s %DCPIP diffusion coefficient in gel
%D = 0.77e-9*1e12 diffusion in water;

Dasc = 0.31e-9*1e12; %um2/s % Asc diffusion coefficient in gel
%Dasc = 0.87e-9*1e12 diffusion in water;

%set counter
count = 1;

EX = xdata; %AscH concentrations
Exp1 = [25.71,90.62,158.63,185.57]; %pH 7

for Conc = EX./20 %dcpip concentration
    Ctot = Conc;
    n = 2;
    B = 0.5;
    kT_q = 0.025693; %V
    Co_in = A0*Ctot; %initial concentration of oxidized DCPIP %A0 is initial guess
    Asc = Conc-(Ctot-Co_in); %AscH concentration
    Ecopp = 0.14; %V vs Ag/AgCl
    EDCPIP = 0.017; %V vs Ag/AgCl

    %exchange currents from EIS
    i0 = 0.28;

    sol = pdepe(m,@pde1,@pdeic,@pdebc,x,t,[]);

    %calculate currents and potentials
    Co = sol(:,:,1);
    Cr = sol(:,:,2);

    Crate = Co(:,1)./Cr(:,1);

    eta = Ecopp-EDCPIP+(kT_q/n)*log(Crate);
    E1 = (kT_q/n)*log(Crate(1));
    E2 = (kT_q/n)*log(Crate(end));
    current = i0.*((exp((1-B)*n*eta/kT_q))-exp((-B)*n*eta/kT_q));

    i2(count) = current(end);
    Ediff1(count) = (E1-E2)*1000;
```

```
    count = count+1;
end

%calculate currents to compare to experimental data
iNo = i2./i2(end);
ENo = Exp1./Exp1(end);
%--------------------------
function [c,f,s] = pde1(x,t,Co,DuDx)
global D Dasc

%enter reaction rate constants
kOx = 0.00000;
kAsc = 0.299;

c = [1;1;1];
%set reactions for all x values
s = [kOx*Co(2)-kAsc*Co(1)*Co(3);-kOx*Co(2)+kAsc*Co(1)*Co(3);-kAsc*Co(1)*Co(3)];
f = [D*DuDx(1);D*DuDx(2);Dasc*DuDx(3)];

%---------------------------
function Co0 = pdeic(x)
global Co_in Ctot Conc
Co0 = [Co_in;Ctot-Co_in;Conc-(Ctot-Co_in)];

%---------------------------
function [pl,ql,pr,qr]=pdebc(xl,ul,xr,ur,t)
global D n kT_q B i0 Ecopp EDCPIP

%eta and current calculations
etal = Ecopp-EDCPIP+(kT_q/n)*log(ul(1)/ul(2));
cell = i0*((exp((1-B)*n*etal/kT_q))-exp((-B)*n*etal/kT_q));

%left boundary condition
pl = [-cell;cell;0];
ql = [(n*96485.33*1e6*1e8*D/(1e15*1000));(n*96485.33*1e6*1e8*D/(1e15*1000));1];

%right boundary condition
pr = [cell;-cell;0];
qr = [(n*96485*1e6*1e8*D/(1e15*1000));(n*96485*1e6*1e8*D/(1e15*1000));1];
```

GelPDE_PSI.m

```
function [iPSI] = GelPDE_PSI(B0,xdata)
global D Co_in Ctot n current i0 kT_q B kPSI Ecopp EDCPIP Asc Conc Dasc x0
x1=linspace(0,4,1500); %PSI film thickness in um
x2 = linspace(4.1,400,250); %bulk electrolyte thickness in um
x = [x1 x2];
tmesh = 4000;
t = linspace(0,30,tmesh);
time = round(linspace(0,tmesh,10)); %create 4000 time points from 0-30s for plotting
m = 0; %pdepe parameter
```

```
D = 0.27e-9*1e12; %um2/s %DCPIP diffusion coefficient in gel
%D = 0.77e-9*1e12 diffusion in water;

Dasc = 0.31e-9*1e12; %um2/s % Asc diffusion coefficient in gel
%Dasc = 0.87e-9*1e12 diffusion in water;

%set counters
count = 1;
count1 = 1;

EX = xdata; %AscH concentrations
Exp1 = [25.71,90.62,158.63,185.57]; %pH 7
Exp2 = [35.07,134.91,186.55,202.9]; %PSI pH 7

for kPSI = [0,B0] %B0 is initial guess for kPSI
    for Conc = EX./20 %dcpip concentration
        Ctot = Conc;
        n = 2;
        B = 0.5;
        kT_q = 0.025693; %V
        Co_in = x0*Ctot; %initial concentration of oxidized DCPIP
        Asc = Conc-(Ctot-Co_in); %AscH concentration
        Ecopp = 0.14; %V vs Ag/AgCl
        EDCPIP = 0.017; %V vs Ag/AgCl

        %exchange currents from EIS
        if kPSI ~= 0
            i0 = 0.19;
        else
            i0 = 0.28;
        end

        sol = pdepe(m,@pde1,@pdeic,@pdebc,x,t,[]);

        %calculate currents and potentials
        Co = sol(:,:,1);
        Cr = sol(:,:,2);

        Crate = Co(:,1)./Cr(:,1);

        eta = Ecopp-EDCPIP+(kT_q/n)*log(Crate);
        E1 = (kT_q/n)*log(Crate(1));
        E2 = (kT_q/n)*log(Crate(end));
        current = i0.*((exp((1-B)*n*eta/kT_q))-exp((-B)*n*eta/kT_q));

        if kPSI == 0
            i2(count) = current(end);
            Ediff1(count) = (E1-E2)*1000;
            count = count+1;
        else
            i3(count1) = current(end);
            Ediff2(count1) = (E1-E2)*1000;
            count1 = count1+1;
        end
```

```
    end
end

%calculate currents to compare to experimental data
iPSI = i3./i2(end);
iNo = i2./i2(end);
ENo = Exp1./Exp1(end);
EPSI = Exp2./Exp1(end);

%--------------------------
function [c,f,s] = pde1(x,t,Co,DuDx)
global D kPSI Dasc

%enter reaction rate constants
kOx = 0.00000;
kAsc = 0.299;

c = [1;1;1];
%set reactions for inside or out of the film
if x <= 4 %inside film
    s = [kPSI*Co(2)+kOx*Co(2)-kAsc*Co(1)*Co(3);-kPSI*Co(2)-kOx*Co(2)+kAsc*Co(1)*Co(3);-
kAsc*Co(1)*Co(3)];
    f = [D*DuDx(1);D*DuDx(2);Dasc*DuDx(3)];
else %outside film
    s = [kOx*Co(2)-kAsc*Co(1)*Co(3);-kOx*Co(2)+kAsc*Co(1)*Co(3);-kAsc*Co(1)*Co(3)];
    f = [D*DuDx(1);D*DuDx(2);Dasc*DuDx(3)];
end

%----------------------------
function Co0=pdeic(x)
global Co_in Ctot Conc
Co0 = [Co_in;Ctot-Co_in;Conc-(Ctot-Co_in)];

%---------------------------
function [pl,ql,pr,qr]=pdebc(xl,ul,xr,ur,t)
global D n kT_q B i0 Ecopp EDCPIP

%eta and current calculations
etal = Ecopp-EDCPIP+(kT_q/n)*log(ul(1)/ul(2));
cell = i0*((exp((1-B)*n*etal/kT_q))-exp((-B)*n*etal/kT_q));

%left boundary condition
pl = [-cell;cell;0];
ql = [(n*96485.33*1e6*1e8*D/(1e15*1000));(n*96485.33*1e6*1e8*D/(1e15*1000));1];

%right boundary condition
pr = [cell;-cell;0];
qr = [(n*96485*1e6*1e8*D/(1e15*1000));(n*96485*1e6*1e8*D/(1e15*1000));1];
```